# Transport and driven-dissipative localization in exciton-polariton lattices

Bastián Maximiliano Real Elgueda

▶ **To cite this version:**

Bastián Maximiliano Real Elgueda. Transport and driven-dissipative localization in exciton-polariton lattices. Optics [physics.optics]. Université de Lille, 2022. English. NNT : 2022ULILR025 . tel-03938615

**HAL Id: tel-03938615**
**https://theses.hal.science/tel-03938615**

Submitted on 13 Jan 2023

**HAL** is a multi-disciplinary open access archive for the deposit and dissemination of scientific research documents, whether they are published or not. The documents may come from teaching and research institutions in France or abroad, or from public or private research centers.

L'archive ouverte pluridisciplinaire **HAL**, est destinée au dépôt et à la diffusion de documents scientifiques de niveau recherche, publiés ou non, émanant des établissements d'enseignement et de recherche français ou étrangers, des laboratoires publics ou privés.

# Transport and driven-dissipative localization in exciton-polariton lattices

## Transport et localisation sous forçage et dissipation dans des réseaux d'exciton-polaritons

**Bastián Maximiliano Real Elgueda**

École Doctorale: Sciences de la Matière, du Rayonnement et l'Environnement
PhLAM, Laboratoire de Physique et des Lasers, Atomes et Molécules
Université de Lille


Thèse préparée pour obtenir le grade de:
*Docteur*
Discipline: Milieux dilués et optique fondamentale

Soutenue le 8 Juin 2022 devant le jury composé de:

| | |
|---|---|
| Yan Pennec, *IEMN Université de Lille* | Président |
| Jean-Noël Fuchs, *Sorbonne Université* | Rapporteur |
| Dmitry Krizhanovskii, *The University of Sheffield* | Rapporteur |
| Zhigang Chen, *San Francisco State University - Nankai University* | Examinateur |
| Marzena Szymanska, *University College of London* | Examinateur |
| Pierre Suret, *PhLAM Université de Lille* | Directeur de thèse |
| Alberto Amo, *PhLAM Université de Lille* | Co-Encadrant de thèse |

# Acknowledgements

I would like to acknowledge all people who have contributed to this doctoral thesis. In first place, I warmly thank my PhD supervisor Dr. Alberto Amo. I am very grateful for his trust in my competence and my work, and for giving me the needed freedom to explore what I was interested in. Moreover, he always made the time to discuss about difficulties and progresses of my doctoral thesis and, importantly also, to work with me in the laboratory when was needed. I also appreciate his critical thinking about my work and his constant positive attitude, which has enriched my scientific career and has also left a distinctive mark in it. From a personal point of view, I truly appreciate his hospitality at the beginning and thoughtful with my move to Lille. He was also very empathetic towards my felling of living away from my family, friends and my country during all my time in France.

I thank Pierre Suret for being my formal PhD supervisor, his welcoming and good disposition with every administrative procedure.

I sincerely thank Omar Jamadi who had a postdoctoral position in Alberto's group during my first two years of thesis. He was very welcoming, pleasant and working with him was extremely confortable and enjoyable.

I would also like to thank Jacqueline Bloch, Sylvain Ravets and their research group at the Centre de Nanosciences et de Nanotecnologies (C2N) for the closely collaboration and insightful discussion in every group meeting. Their expertise in polariton research has undoubtedly been very relevant for the successful ending of my thesis. I also thank Aristide Lamaître, Luc Le Gratiet, Abdelmounaim Harouri, Martina Morassi and Isabelle Sagnes from C2N for providing us with cutting-edge samples. Without their experienced work in fabrication of etched semiconductor microcavities this thesis would not had been possible.

Also, I acknowledge the members of the jury for accepting to evaluate my doctoral thesis, for the challenging questions asked during the defense and for the interesting discussions that arose from them.

Finally, I enormously thank Ignacia and my family, their emotional support and love has been essential during these years.

# Abstract

The simulation of lattice Hamiltonians in photonic platforms has been enlightening in the understanding of novel transport and localization properties in the context of solid-state physics. In particular, exciton-polaritons provide a versatile system to investigate these properties in lattices with intriguing band structures in the presence of gain and loss, and particle interactions. Polaritons are hybrid light-matter quasiparticles arising from the strong coupling between photons and excitons in semiconductor microcavities, whose properties can be directly accessed in photoluminescence experiments. In this thesis, we firstly study the features of strained honeycomb lattices made of coupled polariton resonators having high photonic content. In a critically strained lattice, we evidence both a semi-Dirac transport and an anisotropic localization of photons. Secondly, we show that a judicious driving in lattices of lossy resonators allows the appearance of novel localized modes. Using polariton lattices driven resonantly with several optical beams, we demonstrate the localization of light in at-will geometries down to a single site. Finally, we take advantage of the polarization-dependent polariton interaction to demonstrate an optical Zeeman-like effect in a single micropillar. In combination with optical spin-orbit coupling inherent to semiconductor microstructures, the interaction-induced Zeeman effect results in emission of vortex beams with a well-defined chirality. This thesis brings to light the power of polariton platforms to study lattice Hamiltonians with unprecedented properties and it also provides a first step towards the fully-optical generation of topological phases in lattices.

**Keywords:** Photonic lattices, Exciton polaritons, Semiconductor microcavities, Honeycomb lattice, Drive and dissipation, Light-induced magnetic effects

# Résumé

La simulation des Hamiltoniens de réseaux dans les plateformes photoniques a permis de mieux comprendre les nouvelles propriétés de transport et de localisation dans le contexte de la physique de l'état solide. En particulier, les exciton-polaritons constituent un système polyvalent permettant d'étudier ces propriétés dans des réseaux avec des structures de bande intrigantes en présence de pertes et de gains, et d'intéractions entre particules. Les polaritons sont des quasi-particules hybrides lumière-matière résultant du couplage fort entre les photons et les excitons dans les microcavités semi-conductrices, dont les propriétés peuvent être directement accessibles dans les expériences de photoluminescence. Dans cette thèse, nous étudions premièrement les caractéristiques des réseaux en nid d'abeille déformés, composés de résonateurs de polaritons couplés, à haut contenu photonique. Dans un réseau déformé de façon critique, nous mettons en évidence à la fois un transport semi-Dirac et une localisation anisotrope des photons. Deuxièmement, nous montrons qu'un forçage judicieux dans des réseaux de résonateurs à pertes permet l'apparition de nouveaux modes localisés. En utilisant des réseaux de polaritons sous un forçage résonant par plusieurs faisceaux optiques, nous démontrons la possibilité de localiser la lumière sur différentes géométries, voir jusqu'à un seul site. Enfin, nous profitons de l'intéraction de polaritons dépendant de la polarisation pour démontrer un effet optique de type Zeeman dans un seul micropilier. En combinant le couplage spin-orbite optique, inhérent aux microstructures semi-conductrices, avec l'effet Zeeman, induit par l'intéraction, nous montrons l'émission de faisceaux de vortex avec une chiralité bien définie. Cette thèse met en lumière la puissance des plateformes de polaritons pour étudier les Hamiltoniens de réseaux avec des propriétés sans précédent. Elle apporte également un premier pas vers la génération, entièrement optique, de phases topologiques dans les réseaux.

**Mots-clés:** Réseaux photoniques, Exciton-polaritons, Microcavités semi-conductrices, Réseau nid d'abeille, Forçage et dissipation, Effets magnétiques induits par la lumière

# Table of contents

# Chapter 1

# Introduction

During the past two decades, artificial lattices have emerged as a test-bed to probe, emulate and observe a wide variety of phenomena related to condensed-matter physics. They rely on the very fundamental idea that electrons behave collectively as waves in crystalline materials and most of their properties are determined by the respective band structures and Bloch wavefunctions. These lattices have been implemented in a diversity of wave systems, for instance: atomic, electronic, microwave, acoustic, mechanical, and photonic systems. Lattices of coupled waveguides and photonic resonators are some of the most remarkable platforms to explore condensed-matter phenomena in the optics realm [1], including topological phases of matter [2–6]. The possibility of engineering the on-site energies, the hopping strengths and the geometry with high precision are some of the assets of these systems to explore wavepacket dynamics in periodic [1] and nonperiodic structures [7]. Remarkably, richer lattice Hamiltonians can be implemented by exploiting unique properties like on-site gain and loss, and nonlinearities. Furthermore, the use of photons allows directly accessing to the amplitude and phase of the wavefunctions as well as the coherent properties of the wavepacket's evolution by using standard optical techniques.

Some celebrated examples of photonic platforms are photonic crystals [8] and lattices of microwave cavities [9], coupled ring microresonators [10], coupled waveguides [11] and coupled semiconductor micropillars [12], which all together cover a wide range of optical frequencies. In these platforms, the periodic spatial distribution of the waveguides/resonators plays the role of the atomic potential in crystalline materials. Photons are tightly confined in the waveguide/resonator and can propagate across the lattice via evanescent coupling. This coupling arises from the fact that the evanescent tail of the field in each waveguide/resonator penetrates the neighboring ones, but it can

be also tailored by link resonators [10]. Thus, the propagation of photons in lattices is accurately described by a Schrödinger-like equation within the tight-binding model.

Pioneering works have reported outstanding and very fundamental solid-state phenomena using coupled waveguide arrays, such as Bloch oscillations and Zener tunneling in both one-dimensional [13, 14] and two-dimensional [15, 16] lattices. Moreover, linear localization phenomena were achieved by either adding defects or disorder in the lattices. The inclusion of disorder in a two-dimensional lattice yielded to the direct observation of propagation transitions, from ballistic to diffusive propagation, and the subsequent collapse of the wavefunction on a few lattice sites due to incoherent scattering in the lattice, effect better known as Anderson localization [17, 18]. The creation of a defect on two-dimensional square lattices produces a localized state in the bandgap, which has been observed and has allowed the guidance of light [19]. Interestingly also, it has been shown that curved waveguides emulate lattices undergoing an external driving force that can give rise to, for example, dynamical localization [20]. Concurrently, nonlinear experiments were carried out thanks to the nonlinear response of the material in which lattices were fabricated. These experiments immediately showed the potential of photonic systems to simulate more complex conservative lattice Hamiltonians. For example, the control of the nonlinearity allowed achieving a balance between the lattice dynamics and the nonlinear Kerr-type response of the material, observing the formation of lattice or discrete solitons in both one and two dimensions [21–23].

More recently, the exquisite control in the design of lattices has enabled the implementation of a number of lattice geometries with different transport and localization properties. By judiciously choosing the periodicity of the waveguides/resonators, lattices with at least one flat band in their spectra and the consequential compact-localized eigenstates have been reported [24–31], where the localization is achieved without breaking translation symmetry. Also, the captivating Dirac physics of graphene has been implemented using honeycomb lattices [9, 12, 32–34], which has allowed the observation of its localized edge states [33–36], the so-called conical diffraction [32] and the rich dynamics provided by the Dirac pseudospin in propagating lattices [37]. Smart designs of photonic lattices has led photons to undergo artificial gauge fields [38–41] and non-trivial topological phases as well [5, 6, 42–44], giving rise to robust chiral edge states. Alternatively, topological insulators have been also realized in lattices with sensitivity to external magnetic fields [45, 46].

Despite the astonishing capabilities of these platforms, some transport and localization properties have remained elusive due to the need to access simultaneously spectral information and particle dynamics at desire frequencies or energies. In the

majority of these photonic systems, there are important limitations in the engineering of linear localization properties because they are fixed by the lattices and are hardly adjustable once fabricated. More importantly, the role of external driving forces (or forcing) to achieve localization has hardly been addressed so far. Additionally, the use of external magnetic field to trigger certain phenomena introduces more difficulties to the experiments.

A suitable platform to overcome these difficulties are lattices of exciton polaritons. Exciton polaritons (or microcavity polaritons) are hybrid light-matter quasiparticles arising from the strong coupling between the confined photons of microcavities and the quantum-well excitons (i.e. bound electron-hole pairs) of the embedded material. The main signature of this coupling is the splitting of the photon and exciton relation dispersion into two bands called upper and lower polariton bands [47]. Therefore, polaritons can be described as a linear combination of exciton and photons and their properties are directly related to those of their constituents. From the photonic component, polaritons inherit a very low effective mass (about $10^{-5}$ times the mass of free electrons), splitting between transverse-electric (TE) and transverse-magnetic (TM) polarizations and the feasibility of leaking from the cavity in form of photons, which encode all the information on amplitude, phase, energy, polarization (pseudospin) and coherence of polaritons inside the cavity. This allows one to fully characterize polariton bands and study transport properties via photoluminescence experiments. Furthermore, lithography and etching techniques acting on the photonic component makes possible to fabricate one- and two-dimensional lattices. On the other hand, the excitonic component provides polaritons with sensitivity to external magnetic fields and nonlinear interactions. Since excitons have an actual spin, they are sensitive to magnetic fields via Zeeman shift [48] and interactions between them occur mainly via parallel spin channels [49, 50].

Thanks to the state-of-the-art etching techniques, microcavity polaritons can be confined in cylindrically-symmetric microcavities of few-$\mu$m width, called micropillar, where polaritons exhibit quantized energy levels. Polaritons in a micropillar mimic electrons in an atom, therefore, the micropillar can be used as a building block of polariton lattices. Overlapping hundred of micropillars lattices are formed and they can be accurately modeled using a tight-binding approach [51]. Despite the losses and the possibility of inducing local gains by means of pump beams, polaritons can reproduce properties associated to conservative lattice Hamiltonians such as flat bands [52, 53], graphene edge states [36] and topological phases [46, 54]. However, the gain and loss can be exploited in order to simulate non-hermitian Hamiltonians [55, 56], produce

lasing [57, 58] and other interesting localization effects. Moreover, striking nonlinear effects can take place in polariton systems such as bosonic condensation [59], which has been also observed in lattices [60, 61]. Other studies of interactions have been done in a two-coupled micropillar systems [62, 63] and in more complex lattices observing, for instance, discrete solitons in a flat-band lattice [64]. Remarkably, the polarization-anisotropic interactions can be used to break time-reversal symmetry and induced an effective Zeeman splitting similar to the observed with an external magnetic field.

In this doctoral thesis we use lattices of GaAs-based micropillars arranged in a honeycomb pattern to unveil anisotropic transport and localization in unconventional Dirac cones. Taking advantage of the driven-dissipative nature of polaritons, we experimentally show a new type of localized modes in highly-photonic polariton lattices. Last but not least, we exploit the spin-dependent interactions of excitons in a single micropillar to optically break time-reversal symmetry, thus, we give a first step towards the induction of topological phases in lattice Hamiltonians by purely optical means. This thesis is organized as follows:

**Chapter 2** gives a general introduction to semiconductor microcavities used to form exciton polaritons. The main properties of these quasi-particles are presented and the fabrication methods are briefly discussed. The chapter ends with the description of lattice geometries and the experimental setup to perform spectroscopy of polaritons.

**Chapter 3** is devoted to the basics of lattice physics. It briefly presents well-known condensed-matter tools for modeling lattices such as the Bravais lattice, the Bloch's theorem and the tight-binding model. At the end, the particular case of honeycomb lattices is developed.

**Chapter 4** reports the transport and localization properties of semi-Dirac cones in honeycomb lattices. In graphene, semi-Dirac cones arise when it subject to uniaxial strains. In order to mimic this phenomenon, honeycomb lattices with anisotropic hoppings were probed using a linearly polarized laser at energies far from the polariton bands. This has allowed us to study the polariton emission from several lattices with different hopping anisotropies in both momentum and real space that, in turn, has enabled us to unequivocally determine the so-called Lifshitz transition and the semi-Dirac cone. In addition, resonant experiments and simulations were carried out to demonstrate an anisotropic localization at the semi-Dirac point energy, which takes place due to the inherent driving and losses of polariton lattices.

**Chapter 5** presents a simple but fascinating localization effect that happens thanks to the intrinsic driven-dissipative nature of polaritons. This chapter begins with analytical and numerical studies of localized modes down to a single lattice site

in one-dimensional lattices driven coherently by external pumps. The condition for obtaining these localized modes is provided. Then, a generalization in two dimensions is shown. Finally, we present the experimental demonstration of the localized modes by performing resonant experiments in honeycomb lattices.

**Chapter 6** addresses the study of time-reversal symmetry breaking in a single micropillar. Firstly, the main signatures of a micropillar are presented such as its gapped energy spectrum. Secondly, a purely optical Zeeman-like splitting is evinced in the lowest energy mode of the micropillar by performing non-resonant experiments with circularly polarized laser beams. Then, we fully characterize the polarization textures of the first-excited modes, which emerge due to the presence of TE-TM splitting in the sample. Finally, the optical Zeeman effect is used to split apart two states belonging to the first-excited multiplet and having opposite chirality between them.

In **Chapter 7** we draw some conclusions and give some perspectives of the studied phenomena.

# Chapter 2

# Semiconductor Microcavities

Semiconductor microcavity is one of the platforms to reach sizable light-matter interactions. It usually consists in a Fabry-Perot cavity with an embedded optically-active material. The confined cavity photons are tuned in the vicinity of the material transition such that a strong light-matter coupling can be achieved. In this regime, hybrid light-matter quasiparticles, called exciton polaritons, are the more accurate entity to describe the observed phenomena. In this chapter we present the fundamental criteria of semiconductor microcavities to show strong coupling regime and we discuss two excitation schemes. We also introduce the strategy to engineer semiconductor micropillars and lattices of coupled micropillars.

## 2.1 Microcavity photons

A Fabry-Perot cavity can be considered as the simplest optical resonator. It basically consists of two highly reflected mirrors, parallel to each other and enclosing a medium of refractive index $n_c$ and thickness $l_c$. When computing the electromagnetic field inside the cavity in the case of plane-wave incidence at zero angle with respect to the normal axis $\hat{z}$ of the mirrors, one has to impose the boundary conditions at the mirrors on the traveling plane waves, which gives as a result standing waves or modes that obey $\lambda_{c,\,q} = 2n_c l_c/q$ with $q \in \mathbb{Z}$, that is, $\omega_{c,\,q} = q\pi c_0/n_c l_c$ ($c_0$ is the speed of light in the vacuum) [65]. At these wavelengths or frequencies the intensity inside the cavity is maximized and the transmissivity (fraction of transmitted light through the cavity) goes to the maximum value because the accumulated phase of a round-trip is null, therefore, constructive interference results in multiple resonances. The spacing between two consecutive resonances defines a special quantity of the cavity that is the free spectral range:

$$FSR = \omega_{q+1} - \omega_q = \pi c_0 / n_c l_c \,.$$

Furthermore, the reflection coefficient $r$ of the mirrors is related to the damping of the amplitude of the field inside the cavity. Specifically, the amplitude of a wave is reduced by a factor $r$ on each round trip across the cavity, which implies that the transmissivity and reflectivity of a Fabry-Perot cavity can be respectively written as [65]:

$$T = \frac{1}{1 + \left(\frac{2\mathcal{F}}{\pi}\right)^2 \sin^2\left(\frac{\omega}{2FSR}\right)}\,; \quad R = 1 - T\,, \tag{2.1}$$

where the lossy nature of the cavity is defined by the finesse

$$\mathcal{F} := \frac{\pi r}{1 - r^2}\,. \tag{2.2}$$

This parameter has an important influence on the resolution of the transmissivity (reflectivity) resonances: They are well resolved in the limit of large finesse. In this limit, the full width at half maximum (FWHM) of the resonance frequency is proportional to the ratio between the $FSR$ to the cavity finesse [65], i.e.

$$\delta\omega_c = \frac{1}{2\pi}\frac{FSR}{\mathcal{F}}\,, \tag{2.3}$$

hence, the larger the finesse, the smaller the linewidth of the resonance. Importantly, this linewidth provides us the amount of time that a photon stays inside the cavity, called lifetime,

$$\tau_c = \frac{1}{\delta\omega_c}\,. \tag{2.4}$$

Using these quantities, we can define the quality factor (or $Q$-factor) of the cavity, which parametrizes the frequency width of the resonance, as

$$Q = \frac{\omega_{c,\,q}}{\delta\omega_c}\,, \tag{2.5}$$

and, from Eq. (2.4), we can see that it is related to the cavity lifetime as $\tau_c = Q/\omega_{c,\,q}$. Therefore, this parameter is a measure of the rate at which the optical energy decays from the cavity, which explicitly is $\gamma_c = \hbar/\tau_c$.

In the general case of plane-wave incidence at a given angle with respect to the normal axis $\hat{z}$ of the mirrors, photons get confined along this direction and, as a result, the respective wave-vector is quantized inside the cavity: $k_z = \pi q / l_c$, being $q$ a positive

integer. Nevertheless, the in-plane wave-vector $\vec{k}_{\parallel} = k_x\hat{x} + k_y\hat{y}$ is still a continuous vector. Then, the dispersion relation for a photon in the cavity can be written as

$$E_c(\vec{k}) = \hbar\omega_c(\vec{k}) = \frac{\hbar c_0}{n_c}|\vec{k}| = \frac{\hbar c_0}{n_c}\sqrt{|\vec{k}_{\parallel}|^2 + k_z^2}\,, \tag{2.6}$$

and, considering that $|\vec{k}_{\parallel}| \ll |\vec{k}|$, the cavity photon dispersion takes the form

$$E_c(\vec{k}) \simeq \frac{\hbar^2|\vec{k}_{\parallel}|^2}{2m_c} + \hbar\omega^0_{c,\,q}\,, \tag{2.7}$$

where $\omega^0_{c,q} = c_0 k_z/n_c$ and $m_c = \hbar\omega^0_{c,q} n_c^2/c_0^2$. The latter term is regarded as the effective photon mass due to the analogy with the parabolic dispersion of a massive particle in free space. $m_/m_0 \sim 10^{-5}$ ; $m_0$ is the electron rest mass.

The highly reflected mirrors needed for the implementation of Fabry-Perot cavities can be engineered by using multilayer dielectric materials. A distributed Bragg Reflector (DBR) is a particular case of these materials and it can reflect a large amount of light under certain conditions. Precisely, a DBR is composed of many pairs of layers with alternating refractive index $n_1$ and $n_2$ with the same optical thickness, which is a quarter of a given wavelength $\lambda_c$, i.e.

$$\frac{\lambda_c}{4} = d_1 n_1 = d_2 n_2\,, \tag{2.8}$$

where $d_1$ and $d_2$ are the thickness of the layer with refractive index $n_1$ and $n_2$, respectively. This reflector is also viewed as a one-dimensional photonic crystal, where the length $d_1 + d_2$ define the lattice constant along the axis of incidence and, thus, the well-known transfer matrix method is usually used to calculate the allowed and forbidden frequencies [65]. This method enable us to obtain the characteristic reflectivity spectrum of the DBR as well, which strongly depends on both the polarization and the angle of incidence of the optical field.

In order to illustrate how the DBR reflects an optical beam, we take into account a transverse-electric (TE) polarized wave at normal incidence. Figure 2.1(b) shows the reflectivity of a DBR made of pairs of $Al_{0.10}Ga_{0.90}As$ and $Al_{0.95}Ga_{0.05}As$ layers [see Fig. 2.1(a)], with refractive index $n_1 = 3.44$ and $n_2 = 2.95$ at the temperature of 4 K and with a wavelength $\lambda_c = 890$ nm. It can be seen that the reflectivity increases up to values very close to unity in a range of wavelength around $\lambda_c$ with increasing the pairs of layers. In the case of large number of pairs [blue and black lines in Fig 2.1(b)], a high-reflectivity range of wavelengths starts to be sharply delimited by reflectivity dips at which there is a very low reflection and, therefore, a very high transmission of

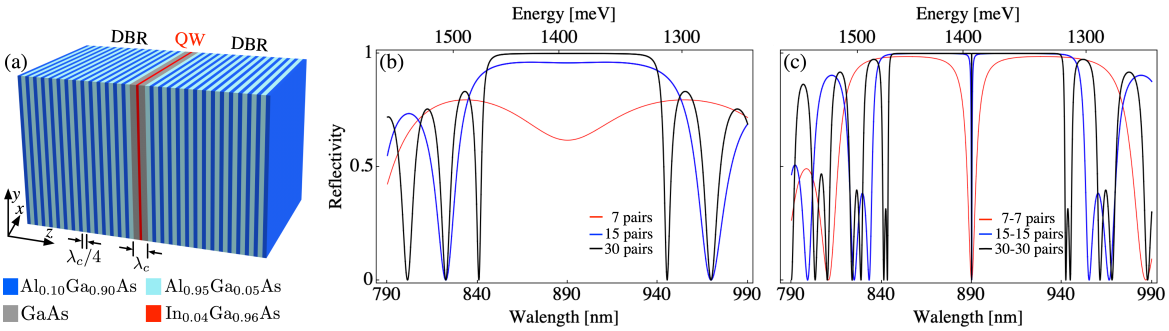


Fig. 2.1 **Semiconductor Microcavity**. (a) Scheme of a semiconductor microcavity composed of two DBRs of 30 pairs of $Al_{0.10}Ga_{0.90}As$/ $Al_{0.95}Ga_{0.05}As$ layers and a GaAs spacer. Details are given in the text. [(b)-(c)] Reflectivity spectrum of a single DBR (b) and the semiconductor microstructure (c) shown in (a). The quantum well is not considered in the computation of the spectrum shown in panel (c).

the incident wave. This high-reflectivity region is known as the stop band of the DBR that is centered at $\lambda_c$ and, indeed, corresponds to the forbidden frequency gaps of the structure. The width of the stop-band region is given by:

$$\Delta\lambda_{sb} = \frac{2\lambda_c \Delta n}{\pi n_{eff}}\,, \tag{2.9}$$

where $\Delta n = n_1 - n_2$ and $n_{eff}$ is the effective refractive index given either by a mean value of the two refractive indices ($\Delta n$ is small) or by geometric means ($\Delta n$ is large) [65]. Note that in this case (normal incidence), a transverse-magnetic (TM) polarized wave also displays the same reflectivity spectrum, however, the reflectivity spectra of both polarizations differ among each other as soon as a small angle of incidence is introduced.

We can now consider the case of a Fabry-Perot cavity made of two DBRs and a spacer of optical thickness of the order of nearly-infrared wavelengths, i.e. $l_c n_c \sim 900$ nm. The entire heterostructure can be also considered as a one-dimensional photonic crystal with a defect in the center, which breaks the discrete translation symmetry of the structure [a scheme of it is shown in Fig. 2.1(a)]. Thus, the confined cavity modes are seen as defect modes, their frequencies lie in the forbidden gaps and, consequently, they are evanescent modes decaying exponentially into the DBRs [66]. Figure 2.1(c) presents a typical reflectivity spectrum of a Fabry-Perot microcavity composed of $Al_{0.10}Ga_{0.90}As$/ $Al_{0.95}Ga_{0.05}As$ DBRs, and a GaAs spacer of refractive index $n_c = 3.55$ with a thickness $l_c = 0.251\,\mu$m. A clear dip is observed at $\lambda = 890$ nm ($E = 1393$ meV) that corresponds to the cavity resonance. As it is expected, the linewidth of the dip becomes narrower when the number of pair layers of the DBRs increases, meaning that

the $Q$-factor of the cavity gets higher. Further analyzing this reflectivity spectrum, dips appear at the eigenfrequencies of this one-dimensional photonic crystal, which means that light is able to enter in the microcavity and goes through it at these frequencies, reaching very high values of transmissivity. This is indeed an interference effect that can be also understood as a resonant tunneling of photons: photons from outside excite the cavity eigenmodes and then jump out, going through the mirrors. Importantly, absorption channels have not been taken into account in this calculation, which are certainly present in experiments.

At this point it is very important to remark that, since the confined cavity mode penetrates evanescently the DBRs, an effective cavity length $l_{eff}$ replaces the actual cavity length $l_c$ [67]. Specifically, $l_{eff}$ accounts for the electromagnetic field penetration into the DBRs ($l_{DBR}$) as $l_{eff} = l_{DBR} + l_c$. Hence, $l_{eff}$ is largely determined by $l_{DBR}$, which is inversely proportional to the refractive index contrast of adjacent layers. Comparing with a simple Fabry-Perot cavity made of metallic mirrors, the inclusion of DBRs results in the reduction of both the FSR and the linewidth of the mode. Consequently, cavities composed of DBRs have lower losses and longer lifetimes [67].

Moreover, the resonance dip at the central wavelength $\lambda_c$ can be tuned by modifying the thickness of the spacer ($l_c$). Specifically, an increase of $l_c$ by a small amount $\delta l_c$ results in the redshift of the resonance and a widening of the linewidth [68]. Interestingly also, an energy splitting between TE and TM polarized dispersions arises as soon as this mismatch is performed, having a quadratic dependency on the in-plane wave-vector. It mainly appears because the penetration depth of the confined cavity field in the DBRs depends on both the incidence angle and polarization [69]. Additionally, for a given wave-vector $\vec{k}_{\parallel}$ the TE-TM energy splitting goes up linearly with $\delta l_c$ with different slopes that are set by the DBRs parameters [68].

When a quantum well is placed at the center of the microcavity as schematized in Fig. 2.1(a), electronic excitation can be strongly coupled to the cavity photon if their resonance energy are approximately equal. Before addressing this situation, we will review the key elements of quantum well excitations.

## 2.2 Quantum well excitons

Excitons are electron-hole pairs bound together by the Coulomb attractive interaction. They arise in a very important class of inorganic and organic materials for which the Fermi energy lies within its narrow band gap, hence, some conduction at finite temperature is possible due to thermally activated carriers. These materials are called

semiconductors and they have a measurable conduction at room temperature if the band gap is less than approximatively 2 eV [70]. There exists a group classification for the semiconductors that is based on the position within the periodic table of their constituent elements. In this thesis we work with inorganic InAs and GaAs semiconductors that both belong to the group labeled III-V semiconductor. In this group, atoms arrange in a zinc-blende crystal structure (same as diamond structure), which has two atoms per unit cell in a face centered cubic (FCC) Bravais lattice. In general, the physical properties of all materials are governed by the bands closest to the Fermi energy, namely the conduction band (right above the Fermi energy) and the valence band (right below the Fermi energy). In the case of GaAs semiconductors, the are four relevant bands: three nearly degenerate valence bands made of $p$ bonding orbitals and one conducting band made of $s$ anti-bonding orbitals [70]. Both the maximum and minimum energy values of the valence and conduction bands, respectively, are reached at quasi-momentum equal to zero (center of the Brillouin zone or $\Gamma$ point), with an energy difference or band gap of $\Delta = 1.519$ eV at cryogenic temperature [66].

The origin of the splitting of the $p$ bands is the intrinsic spin-orbit coupling in zenc-blende-like semiconductors. The six degenerate $p$ orbitals with orbital angular momentum $l = 1$ are split apart into two groups with total angular momentum $j = l + s$ ($s$ is the spin quantum number) and projection $m_j = 0, \pm 1/2, \pm 1, \ldots, \pm j$. At the $\Gamma$ point, the lower-energy $p$ band is the result of eigenstates $|j = 1/2, m_j = \pm 1/2\rangle$ that is called spin-off valence band. While the higher-energy $p$ bands arise from eigenstates $|j = 3/2, m_j = \pm 3/2\rangle$ and $|j = 3/2, m_j = \pm 1/2\rangle$, which are called heavy-hole (hh) and light-hole (lh) bands, respectively. Note that these latter bands are still degenerate at the $\Gamma$ point, but they split at other quasi-momenta [70]. Since the spin-off valence band has larger energies than hh and lh bands, we will neglect it from now on.

When an electron is excited, it moves from the valence band into the conduction band leaving a hole behind that acts as a positive charge. The electron in the conduction band indeed interacts with the hole as it does with a proton in a hydrogen atom, i.e. the electron and the hole are bound together by the Coulomb attractive interaction. This electron-hole pair or exciton is able to propagate in the host semiconductor behaving as a free particle with an energy of the form

$$E_{x,n}(\vec{k}) = \Delta - E_{bind,n} + \frac{\hbar^2 |\vec{K}|^2}{2m_{x,eff}}, \tag{2.10}$$

where $m_{x,eff} = m_{e,eff} + m_{h,eff}$ is the effective total mass formed by the effective mass of the electron and hole, which are related to the electron and hole dispersion. $m^{hh}_{x,eff} =$

$0.45m_0$ and $m^{lh}_{x,\,eff} = 0.08m_0$ are the heavy-hole and light-hole mass, respectively, with $m_0$ the electron rest mass in the vacuum [71]. $\Delta$ is the band gap energy and $\vec{K}$ is the wave-vector of the center-of-mass motion. The binding energy $E_{bind,\,n}$ is obtained from the Bohr's model,

$$E_{bind,\,n} = \frac{1}{n^2}\frac{\hbar^2}{2m_r a^2_{B,\,x}}\,; \quad a_{B,\,x}|_{n=1} = \frac{4\pi\hbar^2\epsilon\epsilon_0}{m_r e^2}\,, \tag{2.11}$$

being $m_r = m_{e,\,eff}m_{h,\,eff}/m_{x,\,eff}$ and $n$ the principal quantum number. The Bohr radius $a_{B,x}$ of the fundamental state of this quasi-particle lies in the order of 150 Å for GaAs semiconductor [66], which means that such excitons can spread over many lattice sites in the semiconductor (the lattice constant of GaAs is about 5.65 Å). Considering the spin momentum of the states that are involved in the transition, excitons have integers total angular momentum $j = 0, 1, 2$, therefore, they undergo bosonic statistics. This bound and delocalized excitons are known as Wannier-Mott excitons[1] [72, 73].

Excitons can be spatially confined in lower dimensions by engineering the subjacent potential, which can lead to strong modification of the exciton's energy and wavefunctions. In two dimensions, excitons are confined by quantum wells, which consist of a thin semiconductor layer (few nanometers thick) sandwiched by another semiconductors acting as potential-barrier layers. The chemical composition of the well is chosen to have the bottom of the conduction (the top of the valence) band at the lower (higher) energy than the surrounding material and, thus, producing quantum confinement of both electrons and holes only along the normal direction (known as growth axis) of the quantum well.

A very important parameter to consider when working with a quantum well is its thickness $L_{QW}$, which is normally chosen to be less than or comparable to the exciton Bohr diameter in the bulk semiconductor ($a_{B,\,x}$). The greatest impact of $L_{QW}$ is on the exciton Bohr radius that, in the ideal 2D case (infinitely high potential), is half of the exciton Bohr radius in 3D, i.e. $a^{2D}_{B,\,x} = a_{B,\,x}/2$, leading to an increase of the exciton binding energy by a factor of four: $E^{2D}_{bind} = 4E_{bind}$ [66]. For realistic quantum-well width, the exciton binding energy ranges from $E_{bind}$ to $E^{2D}_{bind}$ and depends also on the barrier heights for electrons and holes. On one hand, the stronger the confinement, the higher the binding energy and vice versa. On the other hand, $E^{2D}_{bind}$ depends non-monotonically on $L_{QW}$: for wide wells, $E^{2D}_{bind}$ increases with decreasing $L_{QW}$; whereas for ultra-narrow wells, the tendency is inverted due to both electron and

[1] Excitons in inorganic semiconductor are called Wannier-Mott excitons, while they are called Frenkel excitons in organic semiconductor.

hole wavefunctions are wider than $L_{QW}$, and they evanescently decay into the barrier semiconductor. Then, the exciton dispersion relation can be approximatively written as [74]

$$E_x(\vec{k}) = E_x^0 + \frac{\hbar^2 \vec{K}_\parallel^2}{2m_{x,\,eff}}\,, \tag{2.12}$$

where $E_x^0 = \Delta + \Delta E_e + \Delta E_h - E_{bind}^{2D}$. $\Delta E_e$ ($\Delta E_h$) represents the energy levels of the electron (hole) along the quantized direction $\hat{z}$. Note that the quasi-momentum has been split as $\vec{K} = \vec{K}_z + \vec{K}_\parallel$ due to the confinement. Since $\Delta E_h$ is inversely proportional to the effective mass of the particle, the degeneracy of the hh and lh excitons in the valence band is lifted at the $\Gamma$ point [71], thus hh excitons belong to the fundamental excitation of the quantum well.

Excitons in quantum well can be generated by an optical field. One of the simplest mechanisms of matter-light interaction is the absorption of a photon by the semiconductor, which can provide enough energy to an electron to cross the band gap, from a valence-band state to a conduction-band state, and thus exciting an exciton. In order for this process to occur, both energy and momentum conservation need to be satisfied. Energy conservation requires the photon energy to be equal or greater than the lowest energy level of the exciton, while linear momentum conservation needs to be satisfied along in-plane directions because of in-plane translational invariance. An exciton with in-plane wave-vector $\vec{k}_x$ can couple only with a photon with the same in-plane momentum $\vec{k}_p$ that, together with energy conservation, implies that exciton with $\vec{k}_x \geq 30\,\mu\text{m}^{-1}$ are non radiative.

Furthermore, total angular momentum must also be conserved. Since photons have total angular momentum $j = 1$, the optically active excitons are those with the same angular momentum values. As we mentioned above, there are exciton states with $j = 0, 1, 2$, therefore, only excitons with $j = 1$ are optically accessible. For this reason they are called bright excitons. Conversely, the other exciton states cannot be optically excited and are named as dark excitons. However, they can be created in non-resonant experiment, that is, when the energy of the exciting photon is much higher than the exciton energy. Notice that, in principle, photons with circular polarization can efficiently couple to exciton either with pseudospin up ($m_j = +1$) or pesudospin down ($m_j = -1$), whereas photons with linear polarization produce excitons with both pseudospins.

Once excitons are created, they decay either by radiative or non-radiative processes. The radiative process consists in the emission of a photon through exciton recombination,

which is an irreversible process described by the Fermi golden rule. Its typical timescales in a 10-nm GaAs quantum well is $\sim$ 10 ps at 4 K [75]. Non-radiative decay of the excitons mainly happens due to interaction with carriers and spatial inhomogeneities in the material (disorder), being the main raison of the broadening of the exciton linewidth ($\gamma_x$) that gives rise to finite exciton lifetimes $\tau_x = \hbar/\gamma_x$.

When placing the quantum well in a microcavity two different coupling regimes can take place: weak and strong coupling regimes. In the weak-coupling regime, the photon emitted by the quantum well has very low probability of being re-absorbed (irreversible process) because the loss rates overcome the exciton-photon coupling strength and, therefore, the cavity acts as an enhancer of this spontaneous emission at frequencies of the cavity modes, which is known as Purcell effect [66, 76]. In contrast, in the strong-coupling regime, the exciton-photon coupling is stronger than the loss rates resulting in significant probability of photon re-absorption. In this case, excitons and photons cannot be modeled as two independent particles, but as a new light-matter hybrid quasiparticle instead, which is named exciton polariton.

In order to reach strong and quasiresonant coupling of the QW excitons to photons, one or more QWs have to be embedded in Fabry-Perot microcavities at the position of the antinodes of the cavity field. Moreover, $\omega_c^0$ needs to be tuned in the vicinity of the QW exciton frequency $\omega_x^0 = E_x^0/\hbar$.

## 2.3 Exciton polaritons

The energy exchange or coupled dynamics of excitons and photons in high-quality semiconductor microcavities is accurately modeled in the second-quantized formalism by the Hamiltonian [77, 78]

$$\mathcal{H}_{cx} = \int \frac{d^2k}{(2\pi)^2} \left[ E_c(\vec{k})\hat{a}_{\vec{k}}^\dagger \hat{a}_{\vec{k}} + E_x(\vec{k})\hat{b}_{\vec{k}}^\dagger \hat{b}_{\vec{k}} + \frac{\hbar\Omega_R}{2}\left(\hat{a}_{\vec{k}}^\dagger \hat{b}_{\vec{k}} + \hat{a}_{\vec{k}}\hat{b}_{\vec{k}}^\dagger\right)\right], \tag{2.13}$$

where operators $\hat{a}_{\vec{k}}^\dagger$ ($\hat{b}_{\vec{k}}^\dagger$) and $\hat{a}_{\vec{k}}$ ($\hat{b}_{\vec{k}}$) create and destroy a photon (exciton) with in-plane momentum $\vec{k} = \vec{k}_\parallel$ and with a given circular polarization[2], satisfying Bose commutation rules. The bosonic behavior of exctions is well-grounded when the interparticle distance is much larger than their Bohr radius, which implies that electronic screening and interaction between its fermionic constituents is negligible [78]. $E_c(\vec{k})$ and $E_x(\vec{k})$ correspond to the parabolic dispersion of cavity photons and QW excitons [Eq. (2.7)

[2]In order to avoid having several subindices that can make confuse the notation, we have drop the polarization subindex. However, the Hamiltonian is the same for either of both circular polarizations.

and Eq. (2.12)], respectively. The light-matter coupling is described by the last term of Eq. (2.13), which is composed of an emission term ($\hat{a}^{\dagger}_{\vec{k}}\hat{b}_{\vec{k}}$), simultaneous creation of a photon and destruction of an exciton; and absorption term ($\hat{b}^{\dagger}_{\vec{k}}\hat{a}_{\vec{k}}$), simultaneous creation of an exciton and destruction of a photon. Additionally, the coupling strength $\Omega_R/2$ reads

$$\Omega_R = 2\sqrt{\frac{2c_0\Gamma_0}{n_c l_{eff}}} \propto \sqrt{\frac{f_{osc}}{l_{eff}}}\,, \tag{2.14}$$

where $\Gamma_0$ is the is the radiative lifetime of excitons at $\vec{k}=0$ in free space, $l_{eff}$ is the effective cavity length and $f_{osc}$ is the exciton oscillator strength that can be computed from a perturbative approach [67].

The exciton-photon Hamiltonian (2.13) can take a diagonalized form by considering a linear combination of the $\hat{a}_{\vec{k}}$ and $\hat{b}_{\vec{k}}$ operators of the form [77]

$$\begin{aligned} \hat{l}_{\vec{k}} &= X_{\vec{k}}\hat{b}_{\vec{k}} + C_{\vec{k}}\hat{a}_{\vec{k}}\,, \\ \hat{u}_{\vec{k}} &= -C_{\vec{k}}\hat{b}_{\vec{k}} + X_{\vec{k}}\hat{a}_{\vec{k}}\,, \end{aligned} \tag{2.15}$$

where $C_{\vec{k}}$ and $X_{\vec{k}}$ are known as the Hopfield coefficients. These coefficients depend on the photon-exciton detuning $\delta_{\vec{k}} = E_c(\vec{k}) - E_x(\vec{k})$ and the Rabi splitting $\Omega_R$ as

$$|X_{\vec{k}}|^2 = \frac{1}{2}\left(1 + \frac{\delta_{\vec{k}}}{\sqrt{4\hbar^2\Omega_R^2 + \delta_{\vec{k}}^2}}\right) = 1 - |C_{\vec{k}}|^2\,, \tag{2.16}$$

and satisfy the condition $|C_{\vec{k}}|^2 + |X_{\vec{k}}|^2 = 1$. Therefore, the Hamiltonian (2.13) can be written as

$$\mathcal{H}_{pol} = \int \frac{d^2k}{(2\pi)^2}\left[E_{LP}(\vec{k})\hat{l}^{\dagger}_{\vec{k}}\hat{l}_{\vec{k}} + E_{UP}(\vec{k})\hat{u}^{\dagger}_{\vec{k}}\hat{u}_{\vec{k}}\right]. \tag{2.17}$$

This Hamiltonian indeed describes a free bosonic quasiparticle represented by $\hat{l}_{\vec{k}}$ and $\hat{u}_{\vec{k}}$ operators that results from the linear superposition of exciton and cavity photon modes, the so-called exciton polaritons. The dispersion of the so-called upper and lower polariton branches, $[E_{UP}(\vec{k})]$ and $[E_{LP}(\vec{k})]$, displays an anti-crossing form

$$E_{UP,\,LP}(\vec{k}) = \frac{E_c(\vec{k}) + E_x(\vec{k})}{2} \pm \frac{1}{2}\sqrt{\hbar^2\Omega^2 + \delta_{\vec{k}}^2}\,. \tag{2.18}$$

The sign + [−] refers to the upper ($UP$) [lower ($LP$)] branch. Figure 2.2 shows the polariton energy dispersion for three different values of the photon-exciton detuning at $\vec{k}=0$: $\delta_{cx} = \hbar\Omega_R, 0, -\hbar\Omega_R$, with $\hbar\Omega_R = 3.5$ meV. The exciton dispersion seems flat because the exciton mass is much larger that photon mass. At $\delta_{cx} = 0$ and

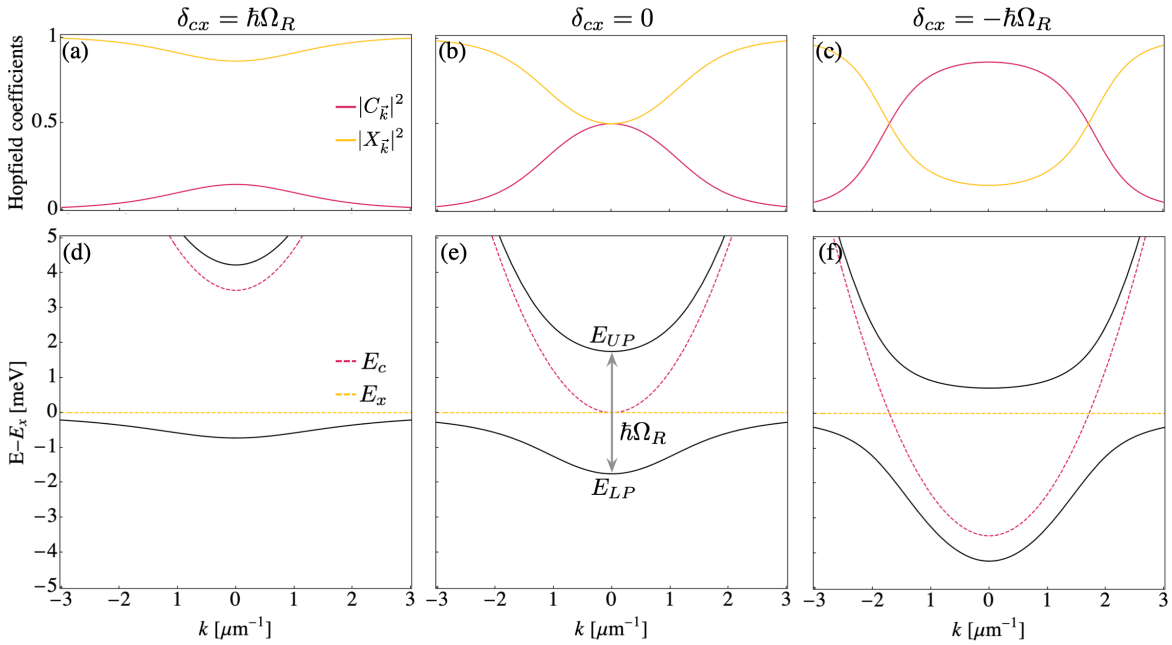


Fig. 2.2 **Exciton-polariton energy dispersion**. [(d)-(f)] Upper and lower polariton branches $E_{LP}$ and $E_{UP}$, respectively, as a function of the in-plane wave-vector $k$ for three different values of the energy detuning $\delta_{cx} = \delta_{\vec{k}=0}$; (d) $\delta_{cx} = \hbar\Omega_R$, (e) $\delta_{cx} = 0$, and (f) $\delta_{cx} = -\hbar\Omega_R$. Cavity-photon and QW-exciton energy dispersion are plotted with colored dashed lines. The corresponding Hopfield coefficients, $|X_{\vec{k}}|^2$ and $|C_{\vec{k}}|^2$, as a function of the in-plane wave-vector are shown in panel (a)-(c).

$\vec{k} = 0$, it is observed the characteristic anti-crossing of the polariton bands with a gap proportional to the Rabi splitting $\Omega_R$. This is the main signature of the strong coupling regime. Additionally, polaritons acquire a more excitonic or photonic behavior depending on both the detuning and the in-plane wave-vector. Focusing on the lower polariton branch, polaritons can have more excitonic or photonic content at $\vec{k} \approx 0$, which depends strongly on the detuning value. Conversely, polaritons always exhibit a predominant excitonic behavior for $\vec{k} \gg 0$, as shown in Fig. 2.2(a)-(c). Note that the lower polariton branch can have a very high photon content at $\vec{k} \approx 0$ in the case of negative detuning and large Rabi splitting.

Equation (2.18) describes accurately the in-plane dynamics of polariton in semiconductor microcavities. From it one can define the effective mass of the polariton by expanding the $E_{LP}$ close to zero values of the in-plane momentum [66],

$$\frac{1}{m_{LP}} = \frac{|X_0|^2}{m_{x,eff}} + \frac{|C_0|^2}{m_c} \approx \frac{|C_0|^2}{m_c}\,. \tag{2.19}$$

The last approximation is valid because $m_{x,eff} \gg m_c$. Therefore, for $\delta_{cx} \leq 0$, the effective mass of polaritons in the lower branch is extremely light, being four orders of magnitude smaller than the electron rest mass. For instance, in typical GaAs based microcavities at zero detuning $m_{LP} \approx 2m_c \approx 6.4 \times 10^{-5} m_0$.

Nevertheless, the finite lifetime of both photons and excitons can significantly determine the dynamics of polaritons. Indeed, in order to observe the strong-coupling regime, the relation $\hbar\Omega_R > |\gamma_c - \gamma_x|$ must be satisfied [74]. Since losses of the cavity-photon are usually predominant, this regime can be achieved when $\hbar\Omega_R > \gamma_c/2$. Furthermore, the linewidth of the polariton modes can be related to the photon and exciton linewidths and the Hopfield coefficients as

$$\begin{aligned} \gamma_{LP}(\vec{k}) &= |X_{\vec{k}}|^2 \gamma_x(\vec{k}) + |C_{\vec{k}}|^2 \gamma_c(\vec{k}) \,, \\ \gamma_{UP}(\vec{k}) &= |C_{\vec{k}}|^2 \gamma_x(\vec{k}) + |X_{\vec{k}}|^2 \gamma_c(\vec{k}) \,. \end{aligned} \tag{2.20}$$

Because $\gamma_x \ll \gamma_c$, the losses of the lower polariton branch at $\vec{k} = 0$ are mostly determined by the cavity-photon losses, i.e. $\gamma_{LP} \approx \gamma_c/2$, therefore, the lifetime of polaritons in the lower branch is $\tau_{LP} \approx \tau_c/|C_0|^2$.

Interactions are other important effects that can drastically change the dynamics of polaritons when the particle density increases. There are different interactions, either between polaritons, excitons or excitons and polaritons. They are generally repulsive and happen through Coulomb exchange interaction of the excitons [78, 49, 50]. This interaction mechanism depends strongly on the pseudospin of the excitons in the considered polaritons: two polaritons with same pseudospin interact directly because it is a resonant process; while interaction of polaritons with antiparallel pseudospin needs dark excitons as intermediate states, which live at a different energy than the lower polariton branch, resulting in a much less probable transition [50]. Also, the presence of each interaction in the polariton dynamics is determined by the driven optical field, which can be tuned either in resonant or out of resonant with respect to the polariton modes. These two excitation schemes are known as resonant and non-resonant excitation (or pumping), respectively, and will be described in detail in the following sections.

### 2.3.1 Non-resonant excitation

In this scheme, the pumping laser is far-blue detuned from the polariton modes creating hot free carriers that relax via phonon emission and, then, form both radiative and non-radiative QW excitons. The former can enter into the strong-coupling regime with

cavity photons, while the latter build up a long-lived exciton reservoir that are able to interact with polaritons via their excitonic component [79]. When the number of particles becomes relevant, the coupling between the polariton field and the excitonic reservoir density becomes important producing a nonlinear shift of the polariton energy, which can be modeled by adding nonlinear terms to the Hamiltonian (2.17) that describes the polariton dynamics. This Hamiltonian with exciton-polariton interaction can be accurately described within a mean-field approximation [80]. Focusing on the lower polariton branch, in the basis of left- or right-circularly polarized ($m_j = \pm 1$) polaritons, a generalized Gross-Pitaevskii (GP) equation models the dynamics of the macroscopic wave function of the lower polariton field $\psi_\pm(\vec{r},t)$, which is coupled through an amplification term $R$ to the local density of the reservoir $n_{R,\pm}(\vec{r},t)$ [80]:

$$\begin{aligned} i\hbar\frac{\partial\psi_\pm(\vec{r},t)}{\partial t} = \Bigg[-\frac{\hbar^2\nabla^2}{2m_\pm} + V_{ext}(\vec{r}) + g_R n_{R,\pm}(\vec{r},t) + g|\psi_\pm(\vec{r},t)|^2 \\ +iRn_{R,\pm}(\vec{r},t) - i\frac{\gamma_c}{2}\Bigg]\psi_\pm(\vec{r},t)\,, \end{aligned} \tag{2.21}$$

where the cavity losses are represented by the term $\gamma_c$ (we assume that they are the same for both polarizations). The parallel interaction between polaritons and the exciton reservoir is captured by the term $g_R$. We have also included an external potential term $V_{ext}$ and taken into account the polariton-polariton interaction captured by the term $g$, which can be also present in this excitation scheme. Additionally, the non-resonant laser feeds the reservoir at a rate $P(\vec{r})$ and, thus, the exciton reservoir density is modeled by a rate equation of the form [80]:

$$i\hbar\frac{\partial n_{R,\pm}(\vec{r},t)}{\partial t} = -\left[\gamma_R + R|\psi_\pm(\vec{r},t)|^2\right] n_{R,\pm}(\vec{r},t) + P(\vec{r})\,, \tag{2.22}$$

where $\gamma_R$ is the relaxation rate. Note that the amplification term $R$ describes the scattering into the polariton modes.

In a low density regime, interactions are negligible and the exciton reservoir populates all the available polariton modes at a rate given by $R$. After tens of picosenconds, polaritons decay and photons leak out the cavity encoding the energy and the in-plane momentum of polaritons. Indeed, photons escape at a given angle $\theta$ with respect to the normal which is determined by the in-plane momentum as $|\vec{k}| = (E/\hbar c_0)\sin\theta$, forming the well-known microcavity photoluminescence. In experiments, this emission is acquired in both momentum and real space by standard optical setups, which allows us to fully characterized the polariton emission. As we will see below, the main inter-

ests of this thesis are situations in which polaritons are subjected to certain external potential $V_{ext}$.

### 2.3.2 Resonant excitation

A different scenario takes place when the pumping laser is tuned at energies (or frequencies) of polariton modes: a coherent driven of the polariton field is triggered. A monochromatic pump laser can only couple to polariton modes matching the energy, intensity and phase profile, and polarization of the pump. In this situation, the creation of an exciton reservoir can be neglected and a coherent incident optical field of the form $F(\vec{r})e^{i\omega_p t}$ is considered[3] [78]. Thus, a driven-dissipative GP equation describes the dynamics of polaritons in the lower branch:

$$i\hbar\frac{\partial\psi_{\pm}(\vec{r},t)}{\partial t} = \left[-\frac{\hbar^2\nabla^2}{2m_{\pm}} + V_{ext}(\vec{r}) + g|\psi_{\pm}(\vec{r},t)|^2 - i\frac{\gamma_c}{2}\right]\psi_{\pm}(\vec{r},t) + F(\vec{r})e^{i\omega_p t}\,. \quad (2.23)$$

In the situation of excitation with a low-intensity optical field, the nonlinear term can be neglected and the dynamics of polariton is fully linear. On the other hand, in the case of high-intensity pumping, the density of particles increase and, consequently, the interactions takes a predominant role in the polariton dynamics. Since the interactions are spin dependent, the term $g$ is composed of parallel $\alpha_1$ (triplet) and antiparallel $\alpha_2$ (singlet) interaction terms and they obey $\alpha_1 \gg \alpha_2$ for the Rabi splitting that we used ($\hbar\Omega_R \geq 3.5$ meV). Therefore, $g \approx \alpha_1$ in our case. In this thesis we only probe resonant pumping in the linear regime and we do not enter in the nonlinear one. We address interested readers to the Refs. [78, 83], which give a comprehensive overview of the reported phenomena in the nonlinear regime.

## 2.4 Polaritons in lattices

The engineering of potential landscapes for exciton polaritons enables changing radically their dynamics. For instance, polaritons can be confined in small spatial regions such that their continuous spectrum turns into a discrete one displaying quantized energy levels. They can be subjected to periodic potentials leading to the emergence of energy bands in the spectrum with negative and positive effective mass. A given potential can be modeled by the term $V_{ext}$ added in the dynamical equations for polariton described

[3] A reservoir of long-lived excitons could coexist with polaritons in this regime. See Ref. [81, 82] for more details.

above and, experimentally, they can be fabricated in semiconductor microcavities by acting on the excitonic or photonic component of polaritons. Different techniques have been developed to spatially control and modulate the polariton constituents, achieving the trapping of polaritons in a diversity of lattice geometries, as reviewed in Refs. [51, 84]. In the following we will highlight some of these experimental techniques.

In the case of potentials acting on the excitonic component, we would like to mention briefly two techniques:

- Surfaces acoustic waves (SAWs): Electrically-stimulated acoustic fields propagate across the semiconductor microcavity changing the local strain environment, which has stronger impact on the excitonic component of polaritons. Depending on the applied acoustic waves 1D and 2D lattices can be implemented [85–87].

- Optical manipulation of the excitonic reservoir: The excitonic reservoir induced by a non-resonant pumping laser provides a purely optical and reconfigurable manner to confine polariton in desire potential landscapes. This approach exploits the repulsive Coulomb interaction between the excitons and polaritons [see Eq. (2.21)] creating a local blueshift in the pumping region. It has allowed to confine polariton in 1D configurations [88] and generate at-will confined geometries by designing the pumping laser beam [89–91].

In the case of acting on the photonic component, we would like to mention three techniques:

- Metallic deposition: This technique relies on the changing of the dielectric constant when depositing a thin metallic layer with a given pattern on the sample surface. It is a simple technique and several pioneering experiments in 1D and 2D periodic potential were implemented in such samples [92, 93].

- Etching before top-mirror growth: This technique consists in growing the bottom DBR together with the cavity spacer and the QW(s). Then, an etching process reduces locally the thickness of the cavity spacer on top of the QW(s) in desire zones and, finally, a growing of the top DBR is carried out. It was firstly implemented in order to reach a 3D spatial confinement of polariton [94] and, afterwards, to place polaritons in a 2D potential landscape [95].

- Post-growth etching: In contrast with the preceding technique, here the whole semiconductor microcavity is grown, which can be then etched down to either the substrate or the cavity spacer (the top DBR is etched only). Both techniques

have been intensively used to produce different lattice geometry in 1D and 2D such as the honeycomb lattice [12, 46, 41] and Lieb lattice [52, 53], to name few.

In this thesis we use samples of GaAs-based semiconductor microcavities, which are fabricated with the post-growth etching technique down to the substrate. The samples were grown and etched in the facilities of Centre de Nanosciences et de Nanotechnologies (C2N) in Palaiseau. The growth process is in charge of the group of Aristide Lemaître, while the etching process is in charge of Luc le Gratiet, Abdelmounaim Harouri and Isabel Sagnes. The heterostructures are grown layer by layer using the Molecular beam epitaxy (MBE) method on an epitaxial quality GaAs substrate with a nominal thickness of 350 $\mu$m. Importantly, in the MBE reactor, the molecular beams are not collimated causing a spatial gradient in the molecular deposition, which can be minimized by rotating the substrate. This effect can be used to generate a gradient of the central wavelength of the cavity over the samples (known as wedge), enabling different photon-exciton detuning. In absence of rotation the detuning gradient is $\Delta_{cx} \sim 6.5$ meV mm$^{-1}$ and can be reduced up to $\Delta_{cx} \sim 0.1$ meV mm$^{-1}$ by rotating the GaAs substrate [68]. Once the samples are fabricated, a reflectivity spectrum analysis at room temperature is performed by the group of J. Bloch and S. Ravets. From this, a spatial map of the cavity resonance is obtained. After this stage, a Silicon Oxynitride quater-wavelength anti-reflective coating (ARC) can be deposited on the substrate facet in order to avoid spurious Fabry-Perot effects. The as-grown planar structures are then processed with electron-beam lithography imprinting the spatial patterns that will be removed by the Inductively Coupled Plasma (ICP) etching. By properly designing the electron beam mask, thin micropillars can be made as well as few coupled micropillars and lattices of coupled micropillars. Specifically, in this thesis we use two samples, one is studied in reflection geometry in chapter 4 and 6. Its composition is summarized in Table A.1 in appendix A. The second one is study in transmission geometry in chapter 5 whose components are tabulated in Table A.2 in appendix A. Notice that the former is composed of twelve GaAs QWs arranged in three groups of four QWs each, while the latter has only one InGaAs QW at the center of the cavity.

### 2.4.1 Single micropillar

Thanks to the etching capabilities developed in C2N, microcavities can be etched in the form of cylindrically-symmetric thin microcavities with a diameter of a few micrometers [96]. Figure 2.3(a) shows a scanning electron microscopy (SEM) image of many cylindrical microcavities of different sizes and a zoomed image of a single one

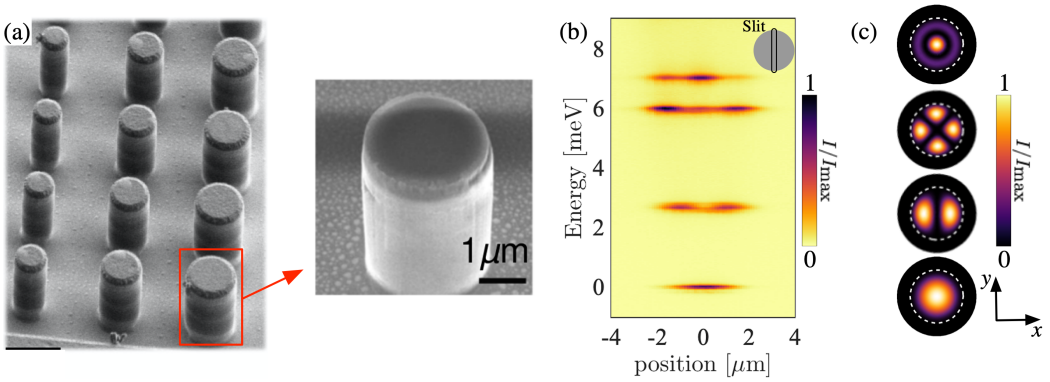


Fig. 2.3 **Micropillar**. (a) SEM image of cylindrical microcavities (micropillar) obtained by deep etching of a planar heterostructure. Right panel shows a zoomed image of the micropillar. (b) Spatially resolved photoluminescence spectrum of a micropillar with diameter $D = 3.6\,\mu$m. Inset: scheme of the position of the spectrometer slit. (c) Calculated intensity profile of the micropillar eigenmodes. Lowest and first-excited modes are respectively called $s$ and $p$ modes. $E_s = 1419.2$ meV.

is displayed in the right panel. These microcavities, named micropillars, provide a tight 3D confinement of the optical modes: The DBRs confine along the longitudinal direction, while the difference of refractive index between the heterostructure and the air produces a transversal confinement, which results in the discretization of the polaritonic energy spectrum because both $k_x$ and $k_y$ wave-number are now quantized. Indeed, the micropillar can be seen as the well-known box problem in fundamental quantum mechanics. Let us remember that the time-independent Schrödinger equation of a particle with a given mass trapped in a potential can be written down in spherical coordinates and split into two parts, one related to the radial degree of freedom and another related to the angular degrees of freedom. Considering an infinite circular barrier at a given radial distance, the problem reduces to solving the so-called radial equation having two quantum numbers, the radial and the angular ones. Solutions of this problem result in eigenmodes whose energy is proportional to the number of zeros of the spherical Bessel functions. The wavefunction of the ground state is radially symmetric while the first-excited states have a wavefunction showing two main lobes with a node in the center. These features are indeed found for a micropillar when solving the scalar Helmholtz equation in an equivalent waveguide problem [97].

Performing non-resonant excitation experiments on a single pillar of a diameter $D = 3.6\,\mu$m, its typical spatially-resolved photoluminescence (PL) spectrum is obtained and displayed in Fig. 2.3(b)[4]. A quantized spectrum with several energy levels is

[4]Experimental details are given in the last section of this chapter.

clearly observed. Their eigenstates can be calculated from the paraxial Helmholtz equation considering a circular-step potential with an effective refractive index of the heterostructure $n = 3.42$, which are shown in Fig. 2.3(c). Notice that the lowest energy states have the spatial profile expected from the circular box problem. The two lowest energy modes are of special interest for this thesis and we called them $s$ orbital mode (ground state) and $p$ orbital mode (first-excited state) owing to their symmetry and similarities with the modes of an atom. Importantly, the energy of the pillar's modes can be varied by modifying the pillar diameter: the thinner the pillar the higher the eigenvalue energies. Interestingly, inherent polarization effects in microcavities can yield a richer spectrum of the single pillar, as we will see in chapter 6.

For the purpose of this thesis, the micropillar is regarded as the building block of more complex systems. Indeed, overlapping micropillars allow polaritons to hop from one pillar to others, which allows the study of lattice Hamiltonians with all the polariton features included. The simplest case corresponds to two overlapping micropillars with equal radius $R$ at a center-to-center distance $a$ (this system is also known as dimer), as shown in Fig. 2.4(a). Providing that the overlapping of the micropillars is small, this system (dimer) can be described by a basis composed of the $s$ mode of each pillar connected by a hopping energy term [98]. This model gives as a result the hybridization of the $s$ modes and the formation of two new states. They are the linear superposition of the $s$ modes of each pillar and, moreover, they split apart by an energy equal to twice the hopping energy. Specifically, if $|\psi_R\rangle$ and $|\psi_L\rangle$ denote the $s$ modes of the right and left pillar, respectively, the eigenstates of the dimer read $|\psi_\pm\rangle = (|\psi_R\rangle \pm |\psi_L\rangle)/\sqrt{2}$ and their energy are $E = E_0 \pm t$, with $E_0$ the nominal energy of the pillars and $t$ the hopping energy. In analogy with a dimer molecule, we call $|\psi_+\rangle$ the bonding states and $|\psi_-\rangle$ the anti-bonding state. Notice that, this approximation is only valid when $t/E_0 \ll 1$, otherwise the hopping term is not perturbative and cannot be decoupled of effects on the pillar energy $E_0$. This presented model is known as the tight-binding model or LCAO theory that we will describe in the next chapter.

Figure 2.4(b) shows the spatially-resolved PL of a dimer composed of two micropillar with $R = 2.0\,\mu$m and $a = 3.6\,\mu$m reported in Ref. [98]. This emission also exhibits a discretized spectrum where the two lowest energy levels belong to the superposition of $s$ modes, which are schematized in Fig. 2.4(c). The most important feature of the dimer is that the hopping energy can be modified by tuning the center-to-center distance $a$. Figure 2.4(d) shows the lowest energy emission from a single pillar together with the two lowest energy levels of various dimers with different center-to-center distances. It

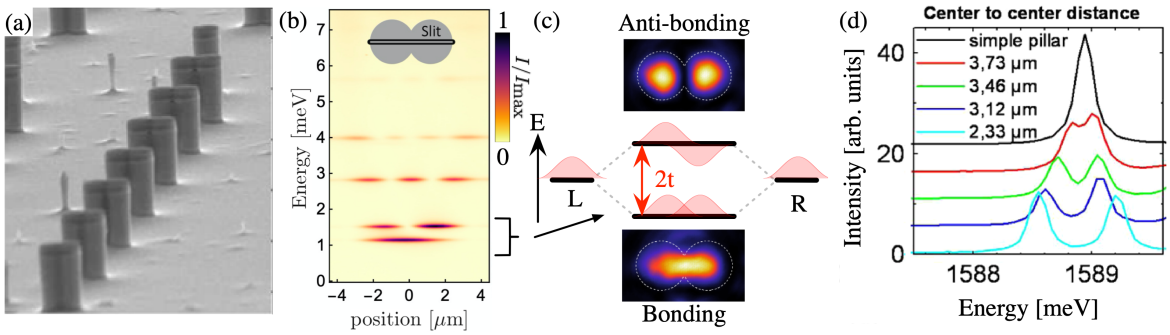


Fig. 2.4 **Two overlapping micropillars**. (a) SEM image of several overlapping micropillars forming a dimer with different center-to-center distances. (b) Spatially resolved photoluminescence spectrum of a dimer with $D = 4\,\mu$m and center-to-center distance $3.6\,\mu$m. Inset: position of the spectrometer slit. Adapted from Ref. [68]. (c) Energy level scheme of the hybridization of the two $s$ modes of a single micropillar into bonding and anti-bounding orbitals in a dimer. (d) Emission spectrum of a single micropillar with $D = 4\,\mu$m and two overlapping micropillars with $D = 4\,\mu$m and various center-to-center distances. Panel (a) and (d) are taken from Ref. [98].

can be clearly observed that the splitting of the energy levels of the dimer increases with decreasing $a$.

### 2.4.2 Lattice Hamiltonian simulation

We have seen that the precise control of the etching technique allows us to carefully tune both the eigenenergies of a pillar and the hopping energy between two pillars, which can be exploited when overlapping hundred of micropillars with a given spatial geometry. Thus, the judicious control of these parameters enables us to study phenomena related to lattice Hamiltonians and to engineer polariton bands with desire features. For instance, the physics of graphene has been intensively explored in our group by the overlapping of hundred micropillars in a honeycomb pattern, which is shown in Fig. 2.5(a). The remarkable band structure of graphene with the well-known Dirac cones has been directly observed [12]. Also, other outstanding phenomena have been reported such as edge states [36, 99], exotic Dirac cones [100] and anisotropic transport of polaritons in a semi-Dirac cone [101] (chapter 4 is devoted to this phenomenon). In order to give a glance of the main features of this lattice, we present in Fig. 2.5(b) the measured PL intensity in momentum space at the energy of the Dirac points of a honeycomb lattice with pillars of $D = 2.6\,\mu$m and a lattice constant $a = 2.4\,\mu$m. The photon-exciton detuning is $\sim -15$ meV (highly photonic). It can be clearly seen the corresponding hexagonal shape of the Brillouin zone [16]. Figure 2.5(c) shows the emission spectrum

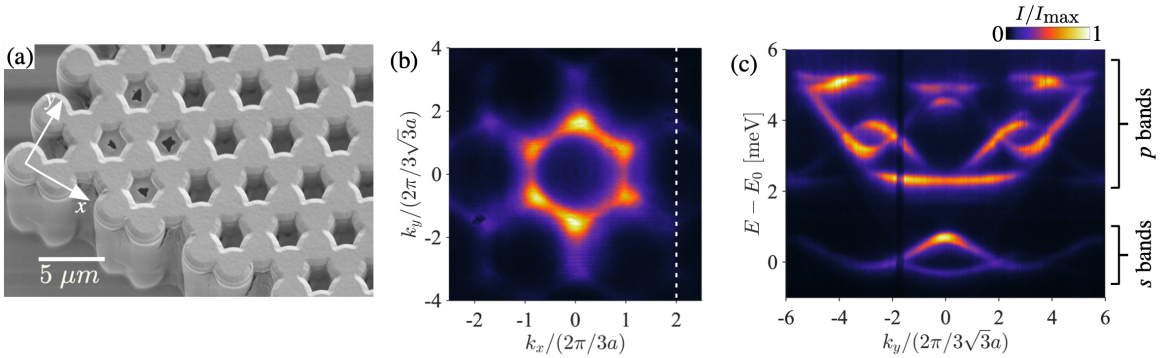


Fig. 2.5 **Polariton Honeycomb lattice**. (a) SEM image of multiple overlapping micropillars arranged in a honeycomb geometry. (b) Measured photoluminescence intensity in momentum space at the energy of the Dirac points. (c) Emission spectrum in momentum space at $k_x = 4\pi/3a$ ($a = 2.4\,\mu$m) pointed out by the dashed white line in panel (b). $s$ and $p$ bands are indicated.

at $k_x = 4\pi/3a$, position depicted in panel (b) by a white dashed line. We can observe two group of bands separated by an energy gap. The two lowest bands arise from the coupling between the $s$ mode of the micropillars, whereas the higher bands emerge from the coupling of the $p$ modes. Focusing on the lowest energy bands, a linear crossing between the two bands can be observed, which corresponds to the Dirac cones of Graphene.

Other groups have reported the observation of incredible effects in lattices of overlapping micropillars, corroborating the capability of this platform to simulate lattice Hamiltonians and observe intriguing phenomena. For example, the observation of flat-band states [52, 53], gauge field for photons [41] and an exciton-polariton topological insulator [46].

## 2.5 Experimental setup

Figure 2.6(a) displays a scheme of the experimental setup used to pump the semiconductor microcavities and to detect the polariton photoluminescence in real space. Along this thesis, we use two excitation or pumping schemes called reflection and transmission geometry. The former is usually used in non-resonant excitation studies, while the latter allows carrying out both non-resonant and resonant excitation experiments. In order to perform experiments, the samples are held inside a close-cycle He cryostat at a temperature of 6 K measured on the sampler holder. The excitation beam comes from a Ti:Sapph mode laser ($<$ 10 MHz linewidth), which passes through a single-mode polarization-maintaining fiber to obtain a clean Gaussian mode. Then, the beam can

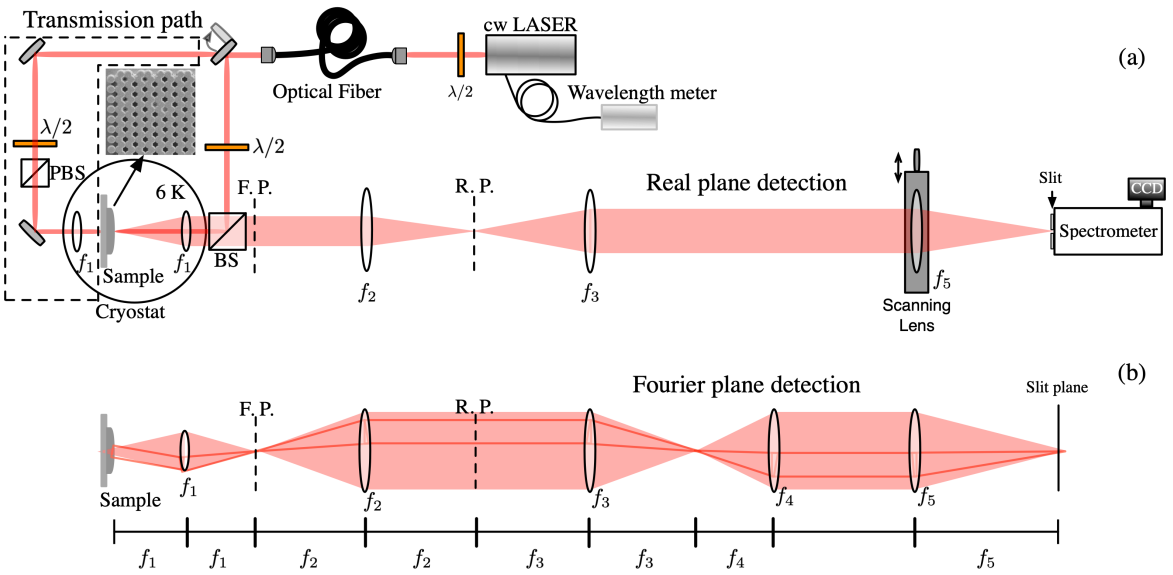


Fig. 2.6 **Experimental setup**. (a) Scheme of the experimental setup to pump the semiconductor microcavities and measure the polariton photoluminescence (PL) in real space. The enclosed region shows the pumping beam path for transmission-geometry experiments. Abbreviations: $\lambda/2$ half-wave retarder, PBS polarized beam splitter, BS beam splitter, F. P. Fourier plane, and R. P. real plane. (b) Detection path to measure the polariton PL in momentum (Fourier) space. Lenses: $f_1 = 8$ mm, $f_2 = 300$ mm, $f_3 = 150$ mm, $f_4 = 200$ mm, $f_5 = 500$ mm.

follow either the reflection or transmission path [see enclosed region in Fig. 2.6(a)] by taking off the mirror that divides the two paths. In both paths the laser beam is tightly focused on the sample by an aspherical lens of 8-mm focal length and numerical aperture of 0.45 [$f_1$ in Fig. 2.6(a)]. In reflection geometry, excitation and detection of the polariton PL are done by the same side of the sample and using the same lens $f_1$ [see right side of the sample in Fig. 2.6(a)], whereas in transmission geometry the PL detection is done by the opposite side to the excitation. Notice that the GaAs substrate is transparent at the working wavelengths. After being collected, the PL is magnified over 100 times by an image system composed of telescopes. Then, it arrives at the entrance port of a spectrometer. The spectrometer slit and a scanning lens placed on a motorized translation stage ($f_5$) allow selecting real-space images of a vertical slice of the emission. The slit has a width of $\sim 32.5\,\mu$m that, taking into account the magnification, corresponds to $0.3\,\mu$m on the sample. Finally, the 1D slice of the image is dispersed by the spectrometer and imaged on a CCD.

Additionally, we also perform angle-resolved scans of the momentum space by adding an extra lens [$f_4$ in Fig.2.6(b)]. By doing so, the imaging system formed by

the $f_2$-$f_3$ and $f_4$-$f_5$ lenses image the Fourier plane of $f_1$ on the spectrometer slit. Each point in this plane corresponds to an angle of emission $\theta$ of the sample, which is directly related to the in-plane momentum of polaritons: $k_{\parallel} = k_0 \cos\theta$, where $k_0$ is the total momentum of the out-coming photons. This configuration enables the observation of the band structure for given cuts of the Fourier plane, as shown in Fig. 2.5(c) in the case of a honeycomb lattice. Acquiring a number of cuts in momentum or real space at different positions of the translation lens, both momentum- and real-space intensity profile of polaritons at desire energies can be reconstructed.

Modifications of this experimental setup have been implemented for the experiments described in chapter 5 and 6.

# Chapter 3

# Introduction to lattice physics

One of the goals of this thesis is to simulate and study physical phenomena related to lattice Hamiltonians using exciton polaritons. Our approach relies on the fruitful understanding of crystals achieved in condensed-matter physics. In the fabrication of a desire lattice Hamiltonian, we use as a building block a micropillar: thin cylindrically-symmetric semiconductor microcavity. The micropillar plays the role of an atom in natural crystals because it confines photons (and, therefore, exciton polaritons) in a small spatial region about $2 - 4\,\mu$m. The confined particles thus exhibit a discrete spectrum of energy levels. This spectrum resembles the atomic orbitals and, hence, exciton polaritons mimic electrons bound to a simplified crystal atom. Since many phenomena in crystal have been understood from the wavy behavior of electrons such as the allowed and forbidden energy bands, artificial lattices offer a playground for studying phenomena that are rather challenging in crystals and, also, for exploring novel phenomenology related to nonlinear physics, for instance. In particular, lattices of coupled micropillars (polariton lattices) allow to directly observe both the eigenstates and the energy bands by performing simple optical experiments. In this chapter, we recall some basic concepts of relevance for the study of lattice Hamiltonians.

## 3.1 Bravais and Reciprocal lattice

Crystals are the thermodynamic equilibrium states of many elements and compounds found in nature. This crystallization occurs because the atoms arrange themselves into special positions to minimize their potential energy, which spontaneously breaks continuous symmetries and gives way to discrete symmetries. One of the consequences of this natural process is that by knowing the position of a few atoms, the position of all others can be predicted. The formalism used in condensed matter to describe a

crystal is to consider a Bravais lattice, which is a set of points (or sites) in the real space of the form [102]:

$$\vec{R}_{\vec{n}} = n_1\vec{a}_1 + n_2\vec{a}_2\,, \tag{3.1}$$

where $\vec{n} \equiv (n_1, n_2)$ is a vector of two integers and $\vec{a}_1$, $\vec{a}_2$ are the primitive lattice vectors. We have restricted ourselves to the two-dimensional (2D) case, but this expression is easily extended to the three-dimensional (3D) case by adding an orthogonal $\vec{a}_3$ vector. This mathematical object is the simplest with the desired discrete translation symmetries. Since atoms are not point-like objects, an alternative way to view a Bravais lattice is to specify its primitive unit cell, which is a fixed area that precisely fills space without overlaps when translated by the lattice vectors. There is not a unique way to define the unit cell, however, any definition must have an area equal to $|\vec{a}_1 \cdot (\vec{a}_2 \times \hat{z})\,|$.

Every crystal has a corresponding Bravais lattice and, in the simplest case, the atoms of the crystal are located at the sites of a Bravais lattice. In most cases, nonetheless, there may be more than one atom per unit cell. In those cases, the lattices are constructed by attaching a set of $m$ points to sites of the Bravais lattice:

$$\vec{R}_{\vec{n},s} \equiv \vec{R}_{\vec{n}} + \vec{\delta}_s;\quad s = 1, 2, \ldots, m\,. \tag{3.2}$$

These lattices are called non-Bravais lattices. If we consider any function that has the periodicity of the lattice, it can be written in Fourier representation as

$$f(\vec{r}) = \sum_{\vec{G}} \tilde{f}(\vec{G}) e^{i\vec{G}\cdot\vec{r}}\,, \tag{3.3}$$

where $\vec{G}$ is determined from the periodicity condition $f(\vec{r} + \vec{R}_{\vec{n}}) = f(\vec{r})$ and by the requirement

$$e^{i\vec{G}\cdot(\vec{r}+\vec{R}_{\vec{n}})} \equiv e^{i\vec{G}\cdot(\vec{r}+n_1\vec{a}_1+n_2\vec{a}_2)} = e^{i\vec{G}\cdot\vec{r}}\,, \tag{3.4}$$

for every $n_1$ and $n_2$. This means that

$$\vec{G}\cdot\vec{a}_j = 2\pi m_j\,;\quad j = 1, 2\,, \tag{3.5}$$

where $m_j$ is an integer. The vector $\vec{G}$ forms a lattice in wave-vector space known as reciprocal lattice:

$$\vec{G} = m_1\vec{b}_1 + m_2\vec{b}_2\,, \tag{3.6}$$

being $\vec{b}_1$, $\vec{b}_2$ the primitive reciprocal lattice vectors. In the 2D case, they are defined by

$$\vec{b}_j = \varepsilon_{ji}(\hat{z} \times \vec{a}_i), \tag{3.7}$$

with $\varepsilon_{ji}$ the anti-symmetric Levi-Civita tensor. As a result

$$\vec{a}_i \cdot \vec{b}_j = 2\pi\delta_{ij}\,, \tag{3.8}$$

and

$$\vec{G} \cdot \vec{R} = 2\pi l\,; \;\; l = n_1 m_1 + n_2 m_2\,. \tag{3.9}$$

In the same way as the Bravais lattice, the reciprocal lattice has its own unit cell that is called first Brillouin zone (or Wigner-Seitz cell), and its boundaries are defined from the Bragg planes that are closest to the origin.

## 3.2 Bloch's theorem

In order to describe the motion of electrons in a crystal, an inherently quantum mechanical approach should be considered, which is based on solving many-body Schrödinger equations. This can be simplified by assuming the ions of a crystal move slowly in space and the electrons response instantaneously with the ionic motion. Thus, the many-body wavefunction depends only on the electronic degree of freedom. This is known as Born-Oppenheimer approximation. Further approximations can be done by neglecting the exchange and correlation effects among electrons and taking them into account in an average way as electron-electron interactions. Thus, these approximations result in a single-particle picture, which describes the behavior of electrons as independent particles in an external potential defined by the ions, together with an external field produced by other electrons. Actually, the single-particle states are not necessarily related to electrons, but to quasiparticles that represent collective excitation of electrons [103].

Since the motion of electrons (particles) in a crystal (lattice) is completely determined by the underlaying crystalline potential $V(\vec{r})$, a single-particle Hamiltonian can be considered,

$$H(\vec{r}) = \frac{\vec{p}^2}{2m} + V(\vec{r})\,, \tag{3.10}$$

where $\vec{p}$ is the momentum vector and the potential captures the lattice translation symmetry, i.e., $V(\vec{r}+\vec{R}_{\vec{n}}) = V(\vec{r})$ with $\vec{R}_{\vec{n}}$ satisfying Eq. (3.1). Thus, the Hamiltonian is also periodic, $H(\vec{r}+\vec{R}_{\vec{n}}) = H(\vec{r})$, and conmutes with the primitive translation

operator $T_{\vec{R}_{\vec{n}}}$, that is

$$[H, T_{\vec{R}_{\vec{n}}}] = 0\,. \tag{3.11}$$

Hence $H$ and $T_{\vec{R}_{\vec{n}}}$ have a common eigenbasis. The Bloch's theorem states the wavefunctions that diagonalize both operators must have the same lattice symmetry, up to a phase factor:

$$\psi^{(n)}_{\vec{k}}(\vec{r}) = e^{i\vec{k}\cdot\vec{r}} u^{(n)}_{\vec{k}}(\vec{r})\,, \tag{3.12}$$

where $u^{(n)}_{\vec{k}}(\vec{r}+\vec{R}_{\vec{n}}) = u^{(n)}_{\vec{k}}(\vec{r})$. The wavevector $k$ lies in the 1st BZ and $n$ is an integer that labels the bands. Then, the single-particle Schrödinger equation takes the form

$$\left[\frac{1}{2m}\left(-i\vec{\nabla} + \hbar\vec{k}\right)^2 + V(\vec{r})\right] u^{(n)}_{\vec{k}}(\vec{r}) = E^{(n)}_{\vec{k}} u^{(n)}_{\vec{k}}(\vec{r})\,, \tag{3.13}$$

which only needs to be solved for $\vec{r}$ within the primitive unit cell of the crystal. The corresponding energy eigenvalues satisfy $E^{(n)}_{\vec{k}} = E^{(n)}_{\vec{k}+\vec{G}}$, having the periodicity of the reciprocal lattice. For a given $n$ the wavevector $\vec{k}$ varies continuously and the eigenvalues form an energy band. This equation is also known as Bloch's equation and the wavefunctions $u^{(n)}_{\vec{k}}$ are called Bloch states.

## 3.3 Tight-binding model

One of the strategies to tackle the Bloch's equation is to use the so-called tight-binding approximation, which considers the limit where electrons are bound to a lattice of ionic potentials and the quantum mechanical tunneling process of an electron between two atoms is seen as a perturbation [70]. Let us consider firstly an isolated atom at the position $\vec{R}_j$, its Hamiltonian is

$$H_j = \frac{\vec{p}^2}{2m} + V(\vec{r} - \vec{R}_j)\,,$$

which can be formally diagonalized

$$H_j \varphi_\sigma(\vec{r} - \vec{R}_j) = E_{j\sigma}\varphi_\sigma(\vec{r} - \vec{R}_j),$$

where $\varphi_\sigma(\vec{r} - \vec{R}_j)$ is the atomic orbital in the atomic state $\sigma$ (*s, p, d,* etc) with atomic energy eigenvalue $E_{j\sigma}$. Recall that for a single atom each atomic orbital is orthogonal to the other, i.e., $\langle\varphi_{\sigma'}|\varphi_\sigma\rangle = \delta_{\sigma'\sigma}$. Now, the crystal potential can be considered as the

superposition of atomic potentials

$$V(\vec{r}) = \sum_j V(\vec{r} - \vec{R}_j)\,,$$

and the single-particle Hamiltonian of the whole lattice is given by

$$H = \frac{\vec{p}^2}{2m} + \sum_j V(\vec{r} - \vec{R}_j) = H_j + \Delta V_j(\vec{r})\,, \tag{3.14}$$

where

$$\Delta V_j(\vec{r}) \equiv \sum_{\vec{R}_i \neq \vec{R}_j} V(\vec{r} - \vec{R}_i)$$

is the potential energy associated to the perturbation of the atom placed at $\vec{R}_j$ due to the presence of all other atoms. Then, the Schrödinger equation takes the form

$$\left[H_j + \Delta V_j(\vec{r})\right] \psi_{\vec{k}}(\vec{r}) = E_{\vec{k}} \psi_{\vec{k}}(\vec{r})\,, \tag{3.15}$$

where $\psi_{\vec{k}}(\vec{r})$ is the single-particle wavefunction. The basic assumption of this approximation is that we can use the atomic orbitals as a basis for expanding the single-particle wavefunctions. Therefore, $\psi_{\vec{k}}(\vec{r})$ can be written as a linear superposition of atomic orbitals:

$$\psi_{\vec{k}}(\vec{r}) = \frac{1}{\sqrt{N}} \sum_j e^{i\vec{k}\cdot\vec{R}_j} \varphi_\sigma(\vec{r} - \vec{R}_j)\,. \tag{3.16}$$

Notice that it can be easily proved that this function satisfies the Bloch's theorem. Using now the Dirac notation, we define

$$\langle \vec{r} | j, \sigma \rangle \equiv \varphi_\sigma(\vec{r} - \vec{R}_j) \;\Rightarrow \left|\psi_{\vec{k}}\right\rangle = \frac{1}{\sqrt{N}} \sum_{j=1}^{N} e^{i\vec{k}\cdot\vec{R}_j} \left| j, \sigma \right\rangle\,,$$

where $N$ is the total number of atoms in the lattice. Assuming the orthogonality between orbitals of different isolated atoms, $\langle j' | j \rangle = \delta_{j'j}$, we obtain the matrix elements of the Hamiltonian from eq. (3.15),

$$\begin{aligned} \langle j', \sigma' | \, H \, | j, \sigma \rangle &= \langle j', \sigma' | \, H_j \, | j, \sigma \rangle + \langle j', \sigma' | \, \Delta V_j \, | j, \sigma \rangle \\ &= E_{j\sigma} \delta_{j'j} \delta_{\sigma'\sigma} + \langle j', \sigma' | \, \Delta V_j \, | j, \sigma \rangle\,. \end{aligned} \tag{3.17}$$

$E_j$ is known as the on-site energy and the second term describes the tunneling of an electron in the orbital $\sigma$ of the atom $j$ to the orbital $\sigma'$ of the atom $j'$ when they

are close enough to each other. This term is also known as hopping matrix element:

$$\langle j', \sigma' | \, \Delta V_j \, | j, \sigma \rangle = \begin{cases} -t & \text{if atoms } j \text{ and } j' \text{ are nearest neighbors with } \sigma' = \sigma \\ 0 & \text{otherwise} \end{cases}$$

We only consider the hopping between nearest neighbors with the same orbitals, however, longer range hoppings could be also considered. A more accurate model that considers the hopping between different orbital can be found in Ref. [104]. Then, the single-particle Hamiltonian of eq. (3.15) can be written as

$$H_{tb} = \sum_j E_j \, |j\rangle \, \langle j| - t \sum_{\langle j'j \rangle} \left( |j'\rangle \, \langle j| + |j\rangle \, \langle j'| \right) , \tag{3.18}$$

where the summation subscripts $\langle j'j \rangle$ indicates the sum over nearest neighbors. Furthermore, we can recast the tight-binding Hamiltonian in the second-quantized formalism. Since the states $|j\rangle$ form a basis of the single-particle wavefunction, a creation operator $c_j^\dagger$ can be defined such that $|j\rangle = c_j^\dagger \, |0\rangle$, being $|0\rangle$ the vacuum states. Therefore, the Hamiltonian now reads

$$\hat{H}_{tb} = \sum_j E_j \hat{c}_j^\dagger \hat{c}_j - t \sum_{\langle j'j \rangle} \left( \hat{c}_{j'}^\dagger \hat{c}_j + \hat{c}_j^\dagger \hat{c}_{j'} \right) . \tag{3.19}$$

The operators obey anti-conmutation relation, $\{\hat{c}_{j'}^\dagger, \hat{c}_j\} = \delta_{j'j}$, for fermions and conmutation relation, $[\hat{c}_{j'}^\dagger, \hat{c}_{j'}] = \delta_{j'j}$, for bosons. Also, it is required that $\hat{c}_j \, |0\rangle = 0$. Notice that we have considered the crystalline potential having the same periodicity of the Bravais lattice that is not always the case and, for non-Bravais lattices like the honeycomb lattice, a slight modification is needed as we will see below.

## 3.4 Introduction to Graphene

One of the most studied models in condensed matter physics is the 2D honeycomb lattice, which describes the natural arrangement of carbon atoms in graphene. Graphene is the constituent material of graphite and, since P. R. Wallace first derived its extraordinary band structure in 1947 [105], it has caught a lot of interest because not only allows to describe properties of many carbon-based materials but also is an excellent platform for studying the Dirac equation [106]. Thanks to this latter feature, massless behavior of quasiparticles in graphene was predicted and experimentally proved [107] together with some other captivating transport phenomena such as antilocalization, Klein tunneling

and the quantum Hall effect [106, 108]. In this section we introduce the honeycomb lattice and its electronic properties by using the concepts illustrated above.

The spatial distribution of the carbon atoms in graphene is displayed in Fig.3.1(a) and its primitive lattice vectors are:

$$\vec{a}_1 = \frac{a}{2}\left(3, \sqrt{3}\right), \ \vec{a}_2 = \frac{a}{2}\left(3, -\sqrt{3}\right), \tag{3.20}$$

where $a \approx 1.42$ Å is the lattice constant. They form the primitive unit cell shown in gray area in Fig. 3.1(a) that is composed of two carbon atoms connected by the vector $\vec{\delta}_1 = (a, 0)$. Thus, the honeycomb lattice is classified as a non-Bravais lattice and can be also seen as the composition of two A and B triangular sublattices. Moreover, each atom has three nearest neighbor with the corresponding vectors $\delta_1$ and $\delta_{2,3} = a(-1/2, \pm\sqrt{3}/2)$. Then, the reciprocal-lattice vectors are:

$$\vec{b}_1 = \frac{2\pi}{3a}\left(1, \sqrt{3}\right), \ \vec{b}_2 = \frac{2\pi}{3a}\left(1, -\sqrt{3}\right), \tag{3.21}$$

and they build up the first Brillouin zone (1st BZ) of the honeycomb lattice that is shown in Fig. 3.1(b). It has an hexagonal shape with four highly symmetric points at

$$\vec{\Gamma} = (0, 0), \ \vec{K} = \left(\frac{2\pi}{3a}, \frac{2\pi}{3\sqrt{3}a}\right), \ \vec{K'} = \left(\frac{2\pi}{3a}, -\frac{2\pi}{3\sqrt{3}a}\right), \ \vec{M} = \left(\frac{2\pi}{3a}, 0\right). \tag{3.22}$$

The tight-binding model captures accurately the transport of particles in graphene [105]. To further understand this fact, let us go a step back to a single carbon atom, whose electronic configuration is $1s^2 2s^2 2p^2$. In this atom, the $1s$ orbital has very low energy forming completely filled bands and, therefore, being irrelevant for the low-energy physics. On the contrary, the four electrons in the $2s$ and $2p$ orbitals determine the low-energy properties of the system. These orbitals are very close in energy and they become mixed orbitals in the presence of a lattice potential because of the breaking of rotation symmetry. In graphene, the $s$, $p_x$ and $p_y$ orbitals hybridize along the direction of the nearest-neighbor bonds and create the so-called $\sigma$ (or $sp^2$) orbitals that, in turn, form bonding and anti-bonding bands with energy far below and far above the Fermi energy. As a result, one electron in the $p_z$ orbital (also called $\pi$ orbital) per carbon atom does not pair up with any neighbor and it completely dominates the low-energy physics.

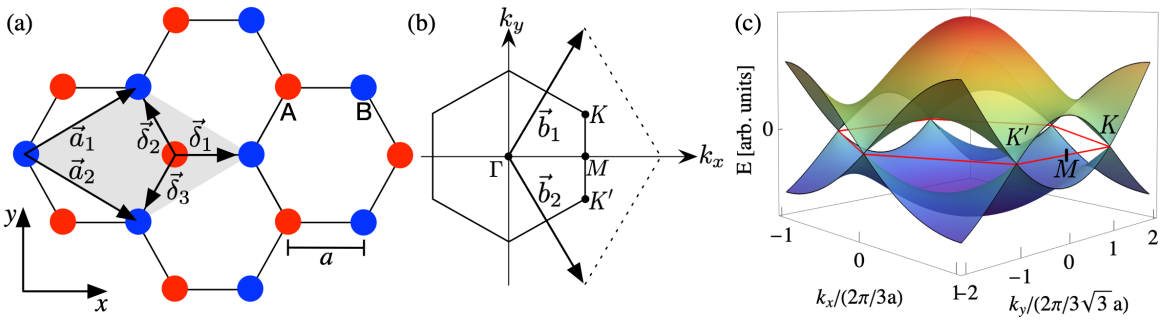


Fig. 3.1 **Honeycomb lattice**. (a) Crystalline structure of the carbon atoms in graphene: Honeycomb lattice. It is composed by two triangular sublattices A and B (red and blue circles, respectively). The enclosed gray area demarcates its primitive unit cell. $\vec{a}_1$ and $\vec{a}_2$ are the primitive lattice vectors, and $\vec{\delta}_1$, $\vec{\delta}_2$ and $\vec{\delta}_3$ are the nearest-neighbor vectors. (b) First Brillouin zone of the honeycomb lattice. $\vec{b}_1$ and $\vec{b}_2$ are the reciprocal-lattice vectors and $\vec{K}$, $\vec{M}$, $\vec{K}'$ and $\vec{\Gamma}$ are the high-symmetry points. (c) Tight-binding band structure (or dispersion) of the honeycomb lattice when considering nearest- and next-nearest-neighbor hoppings. Red lines demarcate the first Brillouin zone and Dirac cones are placed at $K$ and $K'$ symmetry points.

Using the second-quantized formalism, the tight-binding Hamiltonian for the $\pi$ orbitals in graphene reads:

$$\hat{H} = -t \sum_{\langle i,j \rangle} \left( \hat{a}_i^\dagger \hat{b}_j + \text{c.c} \right) - \bar{t} \sum_{\langle\langle i,j \rangle\rangle} \left( \hat{a}_i^\dagger \hat{a}_j + \hat{b}_i^\dagger \hat{b}_j + \text{c.c} \right) , \tag{3.23}$$

where $\hat{a}_i^\dagger$ ($\hat{b}_i^\dagger$) creates an electron on the i-*th* atom of the sublattice A (B), $t$ and $\bar{t}$ are respectively the nearest-neighbor and next-nearest-neighbor hoppings[1], and the on-site energy is set to zero. Considering the discrete Fourier transform of each sublattice operator,

$$\hat{a}_i^\dagger = \frac{1}{\sqrt{N}} \sum_{\vec{k}} e^{i\vec{k}\cdot\vec{r}_i} \hat{a}_{\vec{k}}^\dagger , \quad \hat{b}_i^\dagger = \frac{1}{\sqrt{N}} \sum_{\vec{k}} e^{i\vec{k}\cdot(\vec{r}_i + a\hat{x})} \hat{b}_{\vec{k}}^\dagger , \tag{3.24}$$

where $N$ is the number of A and B sites, the Hamiltonian can be written as

$$\hat{H} = \sum_{\vec{k}} \hat{\Psi}_{\vec{k}}^\dagger h_{\vec{k}} \hat{\Psi}_{\vec{k}} , \tag{3.25}$$

with $\hat{\Psi}_{\vec{k}} = (\hat{a}_{\vec{k}}\ \hat{b}_{\vec{k}})^T$, $\hat{\Psi}_{\vec{k}}^\dagger = (\hat{a}_{\vec{k}}^\dagger\ \hat{b}_{\vec{k}}^\dagger)$ and

[1]Here, we have also included the hopping between next-nearest neighbors because it allows us to better describe the observed asymmetry in the band structure of the exciton-polariton honeycomb lattice, which is studied in the next section.

$$h_{\vec{k}} = \begin{pmatrix} h_{11} & h_{12} \\ h_{21} & h_{22} \end{pmatrix} , \tag{3.26}$$

where

$$\begin{aligned} h_{11}(\vec{k}) = h_{22}(\vec{k}) &= -2\bar{t}\left[\cos\left(\sqrt{3}k_y a\right) + 2\cos(3k_x a/2)\cos\left(\sqrt{3}k_y a/2\right)\right] , \\ h_{12}(\vec{k}) = h_{21}^*(\vec{k}) &= -t\left[1 + 2\cos\left(\sqrt{3}k_y a/2\right)e^{-i3k_x a/2}\right] . \end{aligned}$$

Then, the energy eigenvalues read as

$$E_\pm(\vec{k}) = h_{11}(\vec{k}) \pm |h_{12}(\vec{k})| = -\bar{t}f(\vec{k}) \pm t\sqrt{3 + f(\vec{k})}, \tag{3.27}$$

where $f(\vec{k}) = 2\cos\left(\sqrt{3}k_y a\right) + 4\cos(3k_x a/2)\cos\left(\sqrt{3}k_y a/2\right)$, $\vec{k}$ is defined within the first BZ and the band with sign $+$ $(-)$ is called $\pi$ $(\pi^*)$ band. In the case of $\bar{t} = 0$, this spectrum is symmetric with respect to the Fermi energy ($E_F = 0$), but the bands become asymmetric for finite values of $\bar{t}$. Figure 3.1(c) presents the well-known band structure of graphene in the presence of next-nearest-neighbor hoppings. The two dispersive bands intersect each other at the highly symmetric points $\vec{K}$ and $\vec{K}'$, which means that there is no band gap. When $\bar{t} = 0$, $E_\pm(\vec{K}) = E_\pm(\vec{K}') = E_F$ and graphene is a semimetal. Furthermore, expanding $E_\pm$ near $\vec{K}$ one finds

$$E_\pm(\vec{K} + \vec{k}) \approx \pm v_F|\vec{k}| , \tag{3.28}$$

with $v_F = 3ta/2 \approx 10^7$m/s ($t \approx 2.8$ eV) the graphene Fermi velocity [108]. Therefore, the energy bands depend linearly on $\vec{k}$ around this symmetric point (same for $\vec{K}'$). In this approximation, the Hamiltonian (3.23) can be written as

$$H_{\vec{K}} = v_F \vec{\sigma} \cdot \vec{k} , \tag{3.29}$$

where $\vec{\sigma} = (\sigma_x, \sigma_y)$ and

$$\sigma_x = \begin{pmatrix} 0 & 1 \\ 1 & 0 \end{pmatrix} , \ \sigma_y = \begin{pmatrix} 0 & -i \\ i & 0 \end{pmatrix} , \ \sigma_z = \begin{pmatrix} 1 & 0 \\ 0 & -1 \end{pmatrix} , \tag{3.30}$$

are the Pauli matrices. Likewise, expanding around $\vec{K}'$ we have $H_{\vec{K}'} = v_F \vec{\sigma}^* \cdot \vec{k}$. Therefore, low-energy quasiparticles near the symmetric points $\vec{K}$ and $\vec{K}'$ (Dirac points) obey an effective Dirac Hamiltonian, resembling massless relativistic particles

in 2D with the velocity $v_F$ given by the bands. This is the reason why the conical sections of the honeycomb's band structure are called Dirac cones.

### 3.4.1 Symmetries

Besides the discrete translation symmetry, which is determined by the primitive lattice vectors, the honeycomb lattice possesses two other spatial symmetries that give insight into the properties of the band structure and the eigenstates. They are the three-fold rotation symmetry ($C_3$) and the reflection (or inversion) symmetry ($R$). $C_3$ symmetry is a manifestation of the fact that when rotating the lattice by an angle equal to $2\pi/3$ with respect to a lattice site (fixed point), it remains invariants. $R$ symmetry keeps invariant the lattice when it is applied with respect to a vertical (or horizontal) axis that goes through the center of the lattice. This is because A and B sublattices are indistinguishable. While the former symmetry is responsible for the appearance of the Dirac cones, the latter plays and important role in the protection of them. By implementing a staggered potential, such that A and B sublattices have opposite on-site energy, inversion symmetry can be broken and, as a result, a gap is opened among the bands that destroys the Dirac cones. Such a case is found in a single layer of Boron Nitride (h-BN), in which carbon and nitrogen atoms arrange in a honeycomb pattern [109].

Beyond spatial symmetries and without considering the spin degree of freedom, the real values of the Hamiltonian's eigenenergies ensure the presence of time-reversal symmetry. Taking the complex conjugate of the Schrödinger equation in Fourier space, we have

$$\left(h_{\vec{k}}\Psi_{\vec{k}}\right)^* = E_{\pm}(\vec{k})\Psi^*_{\vec{k}}\,, \Longleftrightarrow h_{-\vec{k}}\Psi^*_{\vec{k}} = E_{\pm}(\vec{k})\Psi^*_{\vec{k}}\,, \tag{3.31}$$

because $h^*_{\vec{k}} = h_{-\vec{k}}$. Therefore, we obtain that

$$E_{\pm}(\vec{k}) = E_{\pm}(-\vec{k})\,. \tag{3.32}$$

Additionally, the honeycomb Hamiltonian with only nearest-neighbor hoppings ($\bar{t} = 0$) anti-commutes with the $\sigma_z$ Pauli matrix,

$$\sigma_z h_{\vec{k}} \sigma_z^\dagger = -h_{\vec{k}}\,, \tag{3.33}$$

which is a hermitian and unitary operator. The main consequence of this special symmetry is that eigenstate $|\psi\rangle$ with energy $\epsilon \neq 0$ has its chiral partner $|\psi'\rangle$ with

energy $\epsilon' = -\epsilon$, thus, giving rise to a symmetric band structure with respect to the Fermi energy. Moreover, zero-energy eigenstates can be chosen to have non-zero amplitude on one sublattice only and they are chiral partners of themselves. Indeed, this fact helps to understand the wavefunction and energy of edge sates in finite graphene as we will see in Chapter 4.

# Chapter 4

# Semi-Dirac Honeycomb Lattices

In the previous chapter we mentioned some extraordinary transport properties of graphene, which arise from the Dirac cones present in its band structure. These conical dispersions are modified when graphene undergoes an uniaxial strain, situation that has driven much attention due to the possibility of modifying the Fermi surface and, consequently, implementing directional transport properties [110–121]. In particular, for a critical compression, a semi-Dirac cone is formed with massless and massive dispersions along perpendicular directions. In this chapter, we show direct evidence of the highly anisotropic transport of polaritons in a honeycomb lattice of coupled micropillars implementing a semi-Dirac cone, which is framed in a semimetal-to-insulator transition (also known as Lifshitz transition). Furthermore, if we optically induce a vacancy-like defect in the lattice, we observe an anisotropically localized polariton distribution in a single sublattice, a consequence of both the semi-Dirac dispersion and chiral symmetry.

## 4.1 Transport in semi-Dirac honeycomb lattices

Strained graphene with modified Dirac cones has been studied from a theoretical point of view by tuning the nearest-neighbor and next-nearest-neighbor hoppings among atoms along a given direction in tight-binding models. Figure 4.1(a) sketches the honeycomb lattice model, where parameters $t'$ and $t$ ($\bar{t}'$ and $\bar{t}$) account for nearest-neighbor (next-nearest-neighbor) hoppings. Using this model, it has been shown that tilted Dirac cones with asymmetric Dirac velocities in the $x$ and $y$ directions can be engineered [110–119], predicting exotic tunneling properties [120, 121] and high-temperature superconducting gaps [122]. A peculiar case of Dirac cone manipulation takes place when the two Dirac cones merge, forming a so-called semi-Dirac cone [112, 115, 123, 124]. The

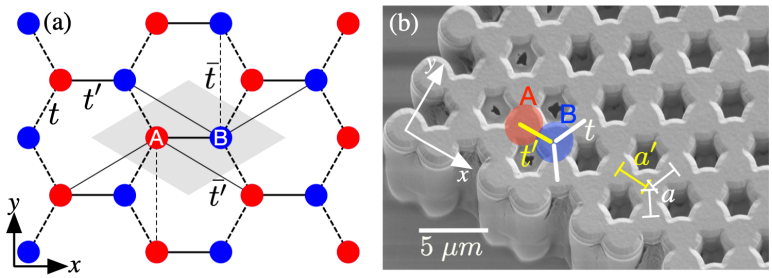


Fig. 4.1 **Strained honeycomb Lattice**. (a) Sketch of a honeycomb lattice, $t'$ (thick-continuous line) and $t$ (thick-dashed line) symbolize the nearest-neighbor hoppings, while $\bar{t}'$ (thin-continuous line) and $\bar{t}$ (thin-dashed line) typify the next-nearest-neighbor hoppings. (b) Electron microscopy image of a polariton honeycomb lattice. Red and blue circles demarcate A and B sublattices. Yellow and white lines denote hopping among horizontal an diagonal nearest neighbors. $a = a' = 2.4\,\mu$m.

semi-Dirac cone is a transition that separates a semimetallic phase with two Dirac cones from an insulating phase with a gap, which corresponds to a topological Lifshitz transition [115, 116]. This transition is achieved in graphene when the Dirac cones move along the edge of the first BZ (line that joins $\vec{K}$ and $\vec{K}'$ points), due to the modification of the hoppings parameters along one direction only, and it takes place when the horizontal hopping is twice stronger than the diagonal one. Figure 4.2(a)-(c) show this situation, the bottom panels schematize the compression of a honeycomb lattice and top panels display the corresponding tight-binding band structure around the Dirac point at the edge of the first BZ. It can be seen that the two Dirac cones merge/annihilate forming the semi-Dirac dispersion at a critical compression [see Fig.4.2(b) top panel]. Interestingly, quasiparticles at the Dirac point behave as massless particles in one spatial direction and as massive ones in the perpendicular direction. The topological feature of the transition is determined by the Berry phase. Before the transition and at low energies, the Berry phase around the Dirac cone at $\vec{K}$ ($\vec{K}'$) takes the value $\pi$ ($-\pi$) and it becomes zero once the two Dirac cones merge [115]. Furthermore, for a finite honeycomb lattice, the bearded edge state disappears when the merging of the two Dirac cones occurs and, conversely, the zigzag edge state extends over the entire BZ [35]. This is shown in Fig. 4.2(d) where an existence plot of the edge states is presented as a function of the compression parameter $\beta \equiv t'/t$ and the wavevector $k$ that is perpendicular to the lattice edge (adapted from Ref. [35]).

The asymmetry of such exotic Dirac cones anticipates highly anisotropic transport and localization properties as studied in a number of theoretical works [112, 115, 123–127]. However, these properties have been hardly explored experimentally due to the difficulty in synthesizing two-dimensional materials with the required asymmetric

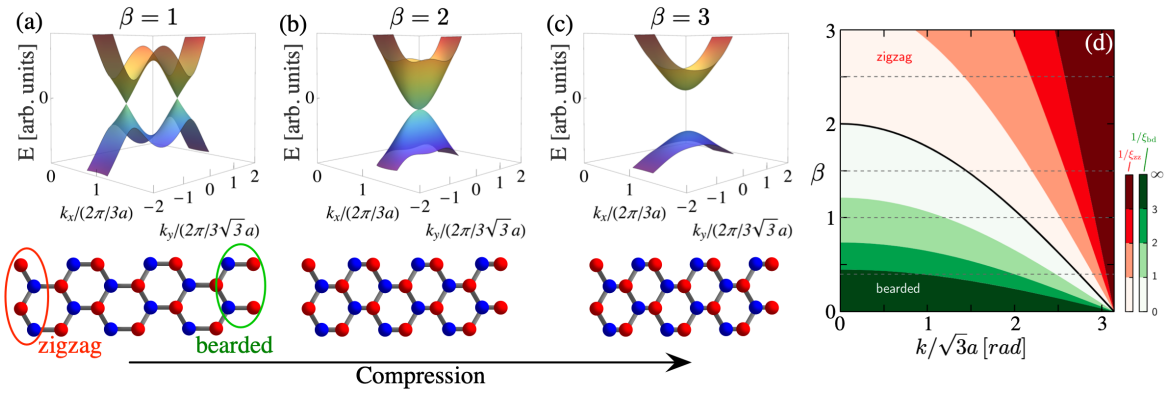


Fig. 4.2 **Lifshitz Transition**. (a)-(c) Band structure around the Dirac points for the indicated $\beta$ values. Bottom panel of each column show schematically the compression of the honeycomb lattice. (d) Parametric diagram, $\beta$ versus momentum $k$, of the existence of the bearded and zigzag edge states. Color maps represent the inverse localization length for the zigzag (red colors) and bearded (green colors) edge states. Panel (d) is taken from Ref. [35].

hoppings and low disorder. For instance, semi-Dirac cones have been observed in black phosphorous [128], but no transport studies are available.

Artificial systems, such as ultra-cold atoms [129], lattices of photonic resonators [9, 35] and waveguide arrays [33, 130] have shown the possibility of engineering semi-Dirac cones with an exquisite control, and demonstrated the effect of the merging of the Dirac cones on the presence of edge states [35, 33, 130]. Despite these progresses, the exotic dispersion of the merging has not been reported in these artificial systems. Moreover, transport and localization properties have not been studied in these platforms because of the need to access simultaneously spectral information and particle dynamics. Lattices of semiconductor micropillars allows to overcome these challenges [12, 46, 100, 41] and provides a controllable platform where the lattice dispersion can be directly observed and the anisotropic transport that happens in a semi-Dirac scenario can be probed.

### 4.1.1 Lifshitz transition in a polariton honeycomb lattice

In order to observe the Lifshitz transition in the polaritonic graphene, we fabricate lattices from a planar semiconductor microcavity made of 28 (top) and 40 (bottom) pairs of $\lambda/4$ alternating layers of $Ga_{0.05}Al_{0.95}As$ and $Ga_{0.80}Al_{0.20}As$ ($\lambda = 783$ nm), a $\lambda/2$ cavity spacer of $Ga_{0.05}Al_{0.95}As$, and twelve GaAs quantum wells embedded at the three central maxima of the electromagnetic field. This microcavity is grown on top of a GaAs substrate. At 6 K, the temperature of our experiments, the microcavity is in the strong

coupling regime between quantum-well excitons and confined photons, giving rise to polaritons characterized by a Rabi splitting of 15 meV. The microcavity is then etched down to the GaAs substrate into honeycomb lattices of coupled micropillars of 2.6 $\mu$m diameter. By varying the center-to-center distance between micropillars, the amplitude of the polariton hopping between neighboring micropillars can be engineered [100] to simulate the homogeneous strain that has been predicted to result in semi-Dirac dispersions [112, 115, 123, 124]. All experiments are done at a photon-exciton detuning of $-15.2$ meV, thus leading to polaritons states with a dominant photonic fraction, which present the longest polariton lifetimes in our samples.

Figure 4.1(b) shows a scanning electron microscope image of a lattice with isotropic hoppings, corresponding to a center-to-center distance of $a = a' = 2.4$ $\mu$m for the three nearest-neighbors links of each micropillar. To measure the polariton dispersion and study the transport properties, photoluminescence experiments are done under excitation at the center of the lattice with a linearly polarized beam in a spot of 8 $\mu$m coming from a continuous-wave Ti:Sapphire laser at 745 nm (1660 meV), much higher energy than the polariton bands. Since the substrate absorbs photons at the working wavelengths, only experiments in reflection geometry can be implemented. The absorption of the photon laser by the semiconductors creates a hot cloud of carriers (electron-hole pairs) that relax incoherently and populate all the polaritonic bands of the structure. Then, polaritons leak out the microcavity in form of photons that encode the energy and momentum of the polaritons inside the structure. An image system generate a 120-times magnified image of the lattice at the entrance port of a spectrometer. This slit allow selecting a vertical slice of the emission either in real or momentum space, which is dispersed by the spectrometer an image on a CCD. Thus, energy-resolved emission from the polariton bands can be recorded along $k_x$ ($k_y$) direction for a specific $k_y$ ($k_x$) position. Figure 4.3(b1)-(b2) shows the emission from the lowest energy bands ($s$-bands) in momentum space. Along the $k_y$ direction [line 1 in Fig. 4.3(a1)] two Dirac crossings are observed in Fig. 4.3(b1), corresponding to the $K$ and $K'$ points characteristic of the unperturbed honeycomb lattice. The Dirac velocities (slopes of the Dirac dispersion) are in this case isotropic around each Dirac cone, as evidenced when comparing the dispersions close to $E_0$ in Fig. 4.3(b1) for $K$ along $k_y$ [line 1 in Fig. 4.3(a1)] and in Fig. 4.3(b2) along $k_x$ [line 2 in Fig. 4.3(a1)].

The polariton dispersion is well reproduced by a tight-binding model, whose eigenvalues as a function of the strain parameter $\beta = t'/t$ are:

$$E_{\pm}(\vec{k}) = E_0 - \bar{t} f(\vec{k}) \pm t\sqrt{(\beta^2 + 2) + f(\vec{k})}\,, \tag{4.1}$$

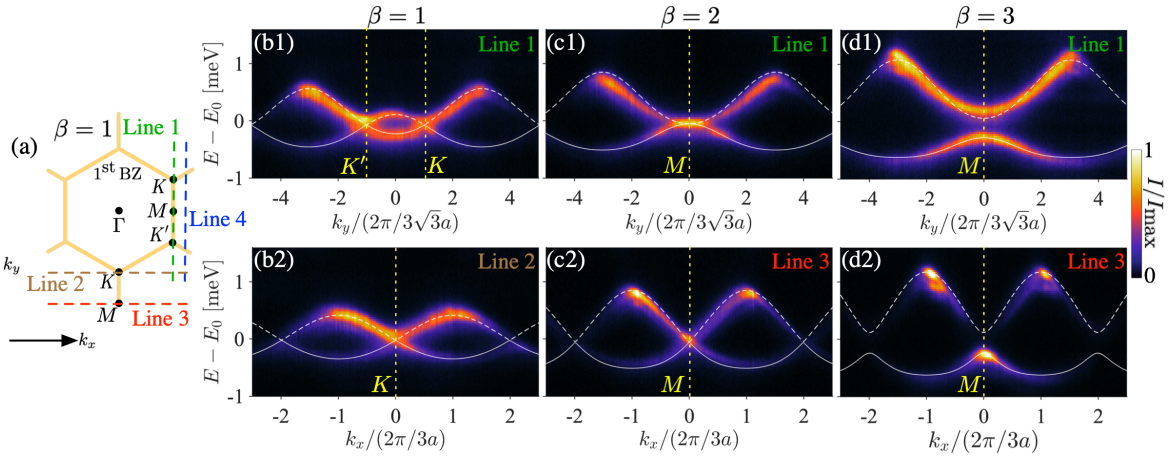


Fig. 4.3 **Dirac cones merging and semi-Dirac dispersion**. (a) Sketch of the Brillouin zones. Middle and bottom rows of columns (b)-(d) are measured polariton photoluminescence intensity in momentum space for different values of $\beta$. Each image is normalized to its maximum. (b1), (c1) and (d1) show the emission along $k_y$ at $k_x = 2\pi/3a$ [line 1 in (a)], while (b2), (c2) and (d2) show the emission along $k_x$ at both $k_y = -4\pi/3\sqrt{3}a$ (line 2) and $k_y = -6\pi/3\sqrt{3}a$ (line 3). White continuous and dashed lines are fits to the lower and upper bands [Eq. 4.1]. $E_0 = 1589.2$ meV and $a = 2.4\,\mu$m.

with, $f(\vec{k}) = 2\cos\left(\sqrt{3}k_y a\right) + 4\cos(3k_x a/2)\cos\left(\sqrt{3}k_y a/2\right)$ and $E_0$ the Dirac-point energy. $\beta$ quantifies the engineered compression strength, which is equal to one in the present case (isotropic hopping). A fit of Eq. (4.1) to the collected photoluminescence [white lines in Fig. 4.3(b1)-(b2)] results in the hopping parameters $t = 0.18$ meV (nearest-neighbor) and $\bar{t} = -0.014$ meV (next-nearest-neighbor). Note that in the micropillar system, the next-nearest-neighbor hopping in Eq. (4.1) is a phenomenological term that reproduces the observed asymmetry of $s$-bands. Its origin is the coupling of $s$ and $p$-modes, as described in Ref. [104].

We experimentally probe the Dirac cones merging in Fig. 4.3(c1)-(c2) for a lattice with $a' = 2.2\ \mu$m and $a = 2.4\ \mu$m. Using the tight-binding model with the previously obtained values of $t$ and $\bar{t}$, a value of $\beta = 2$ reproduces the experimental features. The recorded spectrum along $k_y$ [line 1 in Fig. 4.3(a)] shows not only that the two Dirac cones have merged but, more importantly, the dispersions of both the upper and lower bands are now parabolic in this direction, while they remain linear along the $k_x$ direction. This situation is the expected semi-Dirac cone, which combines massless and massive dispersions along perpendicular directions. If $\beta$ is further increased, the Dirac cone merging evolves into a band gap. We implement experimentally this last situation by reducing further the center-to-center distance $a'$ to 1.7 $\mu$m as shown in Fig. 4.3(d1)-(d2), corresponding to $\beta = 3$.

Besides the bulk consequences of the Lifshitz transition in graphene, it has also a strong effect in the existence of graphene's edge states. The most studied terminations of graphene are zigzag, bearded and armchair edges. While both zigzag and bearded edges present localized states, armchair edge state appears when considering anisotropic graphene, that is, a honeycomb lattice with anisotropic nearest-neighbor hoppings [131–133]. The zigzag and bearded edge states lie at specific values of $\vec{k}$ within the first BZ, in complementary regions that connect the highly symmetric points $\vec{K}$ and $\vec{K}'$, and at zero energy due to the presence of chiral symmetry. Specifically, the zigzag edge state has wavevector $k_y^{zz} \in [-4\pi/3\sqrt{3}a, -2\pi/3\sqrt{3}a] \cup [4\pi/3\sqrt{3}a, 2\pi/3\sqrt{3}a]$ and the bearded edge state possesses wavevector $k_y^{bd} \in [-2\pi/3\sqrt{3}a,\ 2\pi/3\sqrt{3}a]$. Since both edge states live at zero energy for every wavevector $k_y^{zz}$ or $k_y^{bd}$, their dispersion relation is regarded as flat band, which becomes slightly dispersive when next-nearest-neigbor hoppings cannot be neglected. Furthermore, these two edge states are intimately related to the no-zero Berry phase along a straight trayectory in momentum space defined by the geometry of the considered edge [134–136], which is understood as a bulk-edge correspondence. When considering the uniaxial strain in finite graphene, the existence and localization length of the edge states depend on the strain's strength $\beta$ [35]. A comprehensive evolution of the wavevector of the edge states when graphene undergoes strain is presented in Fig. 4.2(d), in which black line depicts the wavevector of the Dirac point. Qualitatively speaking, zigzag edge states exists for any value of strain and its localization length is directly proportional to $\beta$ for a given $k$ (perpendicular to the edge) and, conversely, bearded edge state lives when $\beta \in [0, 2]$ and its localization length is inversely proportional to $\beta$ for a given $k$ [see Fig.4.2(d)]. The disappearance of the bearded edge state is understood as a consequence of the Dirac cones' merging and the null value of the Berry phase along any trajectory in momentum space defined for this edge when $\beta \geq 2$ [35].

The observation of the electronic zigzag and armchair edge states has been achieved using scanning-tunneling microscopic [137]. However, the electronic bearded edge states has remained elusive due to the mechanical instability of the dangling bond associated to this edge. The overcoming of this challenge had to wait for the flourishing of artificial graphene in photonic realm, where all these edge states have been observed [9, 34, 36].

In order to experimentally probe the existence of both bearded and zigzag edge states when going through the transition[1], we carry out experiments on the edges of a regular and compressed polariton lattice as shown in Fig. 4.3(a1)-(a2). Red

[1]Even though this study has been done both theoretically and experimentally in previous works [35, 33] through momentum and real-space measurements, polaritons enable us to directly probe the energy of the edge states.

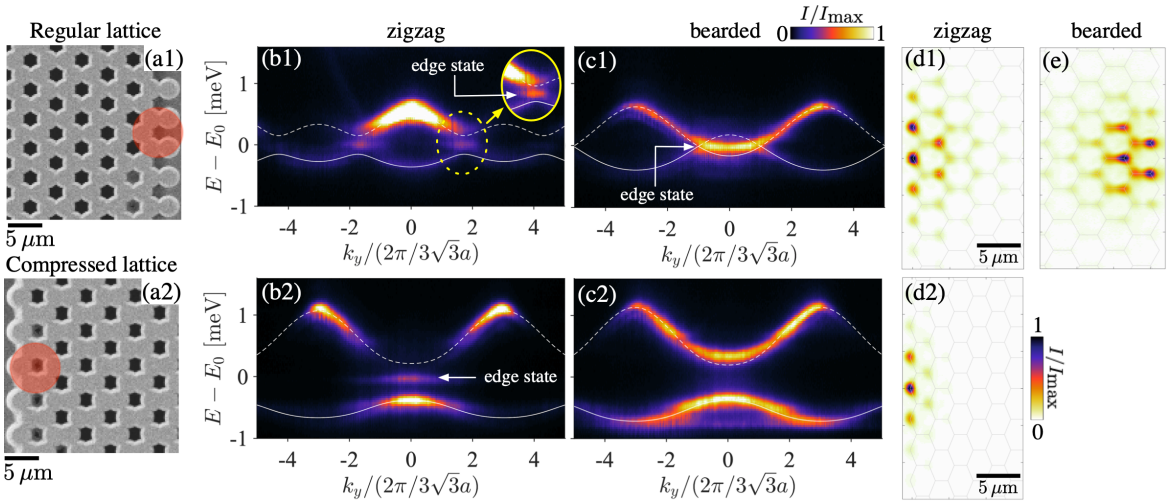


Fig. 4.4 **Zigzag and bearded edge states of Honeycomb lattices**. Electron microscopy image of a regular (a1) and compressed (a2) polariton honeycomb lattice. Red circle schematizes the pump beam on the bearded (a1) and the zigzag (a2) edge. (b)-column Measured polariton photoluminescence in momentum space along the line 4 ($k_x \gtrsim 2\pi/3a$) shown in Fig. 4.3(a1) when pumping on the zigzag edge, for $\beta = 1$ (b1) and $\beta = 3$ (b2). (c)-column Measured polariton photoluminescence in momentum space along the line 1 ($k_x = 2\pi/3a$) shown in Fig. 4.3(a1) when pumping on the bearded edge $\beta = 1$ (c1) and $\beta = 3$ (c2). (d1) and (d2) Emission intensity of the zigzag edge in real space at $E_0 = 1582.2$ meV (energy of the Dirac point) for $\beta = 1$ and $\beta = 3$, respectively. (e) Emission intensity of the bearded edge in real space at the energy of the Dirac point for $\beta = 1$. Hexagons depict the underlying lattice. Each image is normalized to its maximum intensity.

circles depict the pumping beam that has $\sim 8\,\mu$m width and covers 6 pillars (an hexagon). When pumping on the zigzag edge of a regular honeycomb lattice and collecting the photoluminescence in momentum space along $k_y$ direction at a given $k_x \in [2\pi/3a, 4\pi/3a]$ [line 4 in Fig. 4.3(a1)], the two dispersive bands plus emission at $E_0$ energy around $k_y \approx |4\pi/3\sqrt{3}a|$ are detected, which confirms the presence of an edge state. Figure 4.4(b1) shows this case and the inset displays a saturated image that highlights the emission belonging to the edge states. Likewise, Figure 4.4(c1) shows the emission along $k_y$ direction at $k_x = 2\pi/3\sqrt{3}a$ [line 1 in Fig. 4.3(a1)] when a bearded edge is pumped. A flat band between the two Dirac points is observed, corroborating the existence of a localized state on this edge. In the case of a compressed honeycomb lattice ($\beta = 3$), the zero-energy emission from the zigzag edge is still present [see Fig. 4.4(b2)], whereas there is no emission at zero energy from a bearded edge as shown in Fig. 4.4(c2). Only a gapped spectrum is observed, same than the bulk dispersion shown in Fig. 4.3(d1).

Real-space measurement of the photoluminescence allows for the reconstruction of their associated wavefunction and, owing to chiral symmetry, they are expected to be localized on one sublattice. Figure 4.4(d1)-(e) shows the zigzag and bearded edge states, respectively, for a honeycomb lattice without strain. Both edge states are mostly localized on one sublattice, zigzag (bearded) edge state on B (A) sublattice. A little emitted intensity is detected from micropillars of the opposite sublattice, which is caused by the presence of next-nearest-neighbor hoppings in our lattice, which breaks chiral symmetry and destroys slightly the sublattice polarization. Real-space emission at $E_0$ energy for a compressed honeycomb lattice is only detected when pumping the zigzag edge. The reconstruction of the intensity profile exhibits a highly-localized edge state and it has mostly non-zero intensity on the B sublattice [see Fig. 4.4(d2)]. During my thesis I participated in experiments in this lattices which measured the topological invariant associated to the existence of edge states, for different values of $\beta$, by means of the use of a technique known as measurement of the mean chiral displacement. The results were published in Ref. [138].

### 4.1.2 Real-space features of the semi-Dirac dispersion

The semi-Dirac scenario predicts strong consequences on the transport properties of polaritons in the bulk. To verify this, we now pump the lattice in the central region using the same beam as before and we measure the polariton emission in real space at several $x$ position. Then, the real-space polariton distribution can be reconstructed at a number of emission energies by collecting the recorded data. Figure 4.5(a1)-(b1) shows the real-space emission at the energy of the Dirac point $E_0$ for $\beta = 1$ and $\beta = 2$, respectively. For $\beta = 1$, polaritons propagate isotropically across the lattice, whereas, for $\beta = 2$, they travel further away along the $x$ direction than the $y$ direction, exhibiting a significantly anisotropic propagation. By measuring the propagation length along both $x$ and $y$ directions in both lattices, the anisotropy is quantified. To extract the propagation length, we firstly select a rectangular region along each direction [enclosed region in Fig 4.4(a1)-(b1)] and we then integrate along the shorter directions. By doing so, an integrated intensity profile of the real-space emission on each direction is obtained. Finally, by fitting an exponential decay to the tails of the $x$ and $y$ profiles, i.e. $|\psi(r)|^2 \propto e^{-r/L_r}$, the propagation length $L_r$ ($r = x$ or $r = y$) is determined. Notice that we only take into account points far from the pumping region in order to avoid excitonic construbution to the decay. Figure 4.5(a2)-(b2) show the measured intensity from each micropillar in the rectangles depicted in Fig. 4.5(a1)-(b1) - each point corresponds to the emission from a micropillar. For $\beta = 1$, the propagation

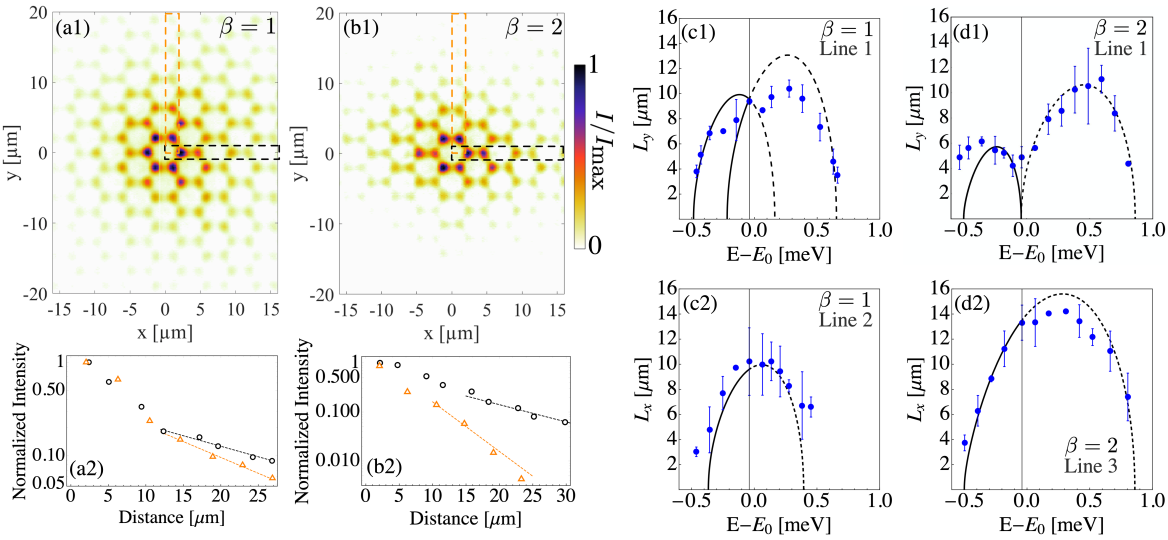


Fig. 4.5 **Transport at the semi-Dirac point**. (a1) and (b1) emission intensity in real space at the energy of the Dirac point ($E_0 = 1582.2$ meV) for $\beta = 1$ and $\beta = 2$, respectively. Each image is normalized to its maximum intensity. (a2) and (b2) the measured intensity along $x$ (circles) and $y$ (triangles) directions for $\beta = 1$ and $\beta = 2$, respectively, extracted from the dashed boxes in (a1) and (b1). Lines are exponential decay fits. (c1) and (c2) The measured propagation lengths (dots) at several energies along the $y$ and $x$ directions for $\beta = 1$. (d1) and (d2) Same for $\beta = 2$. Solid and dashed lines display the theoretical propagation lengths corresponding to the upper and lower bands in Fig. 4.3. The vertical line depicts the Dirac-point energy $E_0$.

lengths are $L_x = 10.21 \pm 2.69$ $\mu$m and $L_y = 9.38 \pm 0.23$ $\mu$m. These values confirm the isotropic transport of polaritons near the Dirac-point energy, which was previously measured in the form of conical diffraction [32]. For $\beta = 2$, at the same energy, we obtain $L_x = 13.31 \pm 1.40$ $\mu$m and $L_y = 4.89 \pm 0.84$ $\mu$m, evidencing the high group velocity in the direction of the massless dispersion, and the reduced group velocity along the $y$ direction associated to the parabolic shape of the bands [see Fig. 4.3(c1)]. From this analysis, the polariton population is expected to decay $1/e^3$ at a distance of $3L_y$ (about 15 $\mu$m away), which means that 95% of the population has decayed at such a distance.

We also perform the same analysis for a number of energies within the $s$ bands. Figure 4.5(c1)-(d2) shows in filled dots the measured propagation lengths $L_x$ and $L_y$ as a function of the energy across the Dirac point. This measurement can be directly compared to the propagation length expected from the tight-binding group velocities, $v_{g,x(y)} = \partial E/\partial k_{x(y)}$, in the following way:

$$L_{x(y)} \approx v_{g,x(y)}\tau\,. \tag{4.2}$$

$v_{g,x(y)}$ is calculated from the dispersion curves in Fig. 4.3 along the vertical ($k_x = 2\pi/3a$) and horizontal ($k_y = -4\pi/3\sqrt{3}a$ for $\beta = 1$; $k_y = -6\pi/3\sqrt{3}a$ for $\beta = 2$) directions, and $\tau$ is the polariton lifetime. The lines in Fig. 4.5(c1)-(d2) show the propagation lengths calculated from the group velocities predicted by the tight-binding model in each spatial direction below (continuous line) and above (dashed line) $E_0$. Here we assume a polariton lifetime of $\tau = 14$ ps and $\tau = 12$ ps, for $\beta = 1$ and $\beta = 2$ lattices, respectively, which is used as a fitting parameter to the experimental points.

The calculated propagation distances match well the experimental data and reproduce the increase of the propagation length along the $x$ direction when going from $\beta = 1$ to $\beta = 2$, due to the higher hopping in that direction [see Fig. 4.5(c2)-(d2)]. Along the $y$ direction, the expected propagation length for $\beta = 2$ goes down to zero at the Dirac-point energy $E_0$, a consequence of the massive dispersion along that direction [see Fig. 4.5(d1)]. Similarly, the calculated propagation length is also zero at the top and bottom of the bands. Experimentally, the measured propagation length at those points is about 4 $\mu$m. This value is, in part, determined by the linewidth of 60 $\mu$eV associated to the finite polariton lifetime: when selecting a given energy, we are in fact detecting the emission from a small range of energies around the desired one, corresponding to states with a nonzero group velocity. Moreover, diffusion of photoexcited excitons away from the excitation spot might also contribute to the residual measured propagation distance. The hypothetical case of samples with smaller linewidth (longer lifetime) would result in a sharper decrease of the measured propagation along the $y$ direction at $E_0$.

## 4.2 Vacancy-like behavior of polaritons

Further insight of the polaritons' transport properties at the semi-Dirac point energy $E_0$ can be accessed when implementing a resonant-laser excitation scheme. This means that we tune the energy of the laser to be exactly the energy of the semi-Dirac point $E_0$ and, consequently, the laser injects polaritons at this energy only as relaxation to lower states is negligible. Figure 4.6(a) shows the measured intensity when a resonant laser at $E_0$ is focused on a single micropillar of the A sublattice (marked with a circle) in a lattice with $\beta = 2$. To measure the propagation away from the excitation spot, a mask was placed at the center of the image (white area) with the aim of blocking the excitation beam reflecting onto the CCD (the inset shows an image of the reflected pump beam in the absence of the mask). Note that the laser and the emission are at the same wavelength and we can only remove the laser reflection from the sample by

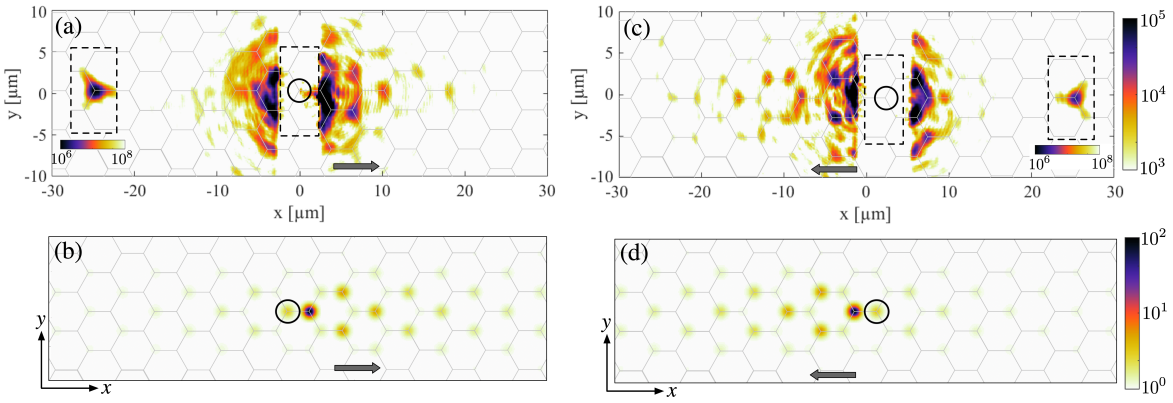


Fig. 4.6 **All-optical analog of a vacancy localization in semi-Dirac graphene**. (a) and (c) The measured photoluminescence intensity in real space at the energy of the Dirac point when a single pillar is pumped (demarcated by a circle) in an A pillar (a) and in a B pillar (c). Insets show the reflected pump spot when the beam block is removed from the central region. (b) and (d) The polariton distribution calculated from Eq. (4.3) when a single A and B pillar, respectively, is pumped at $E_0$ energy. Hexagons depict the underlying lattice.

using the mask. The image shows some stray laser light close to the excitation spot and a decay of the luminescence on the B sublattice towards the right of the excitation spot. If the excitation is centered on a pillar of the B sublattice, the decay direction and the sublattice asymmetry are reversed, as shown in Fig. 4.6(c). Since the reflected laser beam is not completely removed, the acquired intensity data in Fig. 4.6(a)-(c) are plotted in logarithmic scale in order to emphasize the photoluminescence away from the central region.

This behavior is well reproduced using a driven-dissipative model of the polariton dynamics in resonant excitation [78]:

$$i\hbar\frac{\partial\psi_n}{\partial t} = \sum_{m\neq n} t_{n,m}\psi_m - i\frac{\hbar}{\tau}\psi_n + F\delta_{n,n_p}e^{-i\omega_p t}. \tag{4.3}$$

$\psi_n$ represents the polariton amplitude at site $n$, $t_{n,m}$ is the next- and nearest-neighbor hopping, and $F$ is the strength of the pump at frequency $\omega_p$. In the rotating frame of the pump frequency, a steady-state solution of Eq. (4.3) has the form $\psi_n^{ss}(t) = \psi_n^{ss}e^{-i\omega_p t}$. Then, the steady-state equation of the $n$-th micropillar reads

$$\hbar\omega_p\psi_n^{ss} = \sum_{m\neq n} t_{n,m}\psi_m^{ss} - i\frac{\hbar}{\tau}\psi_n^{ss} + F\delta_{n,n_p}\,, \tag{4.4}$$

which can be written in matricial form by considering the vector of the steady-state amplitudes $\vec{\Psi}^{ss} = (\psi_1^{ss}, \ldots, \psi_N^{ss})$, the hopping matrix $H$ ($H_n = \sum_{m \neq n} t_{n,m}$), the dissipative matrix $\Gamma = i\frac{\hbar}{\tau}\mathbb{I}$, the pumping energy matrix $\mathbb{E}_p = \hbar\omega_p\mathbb{I}$ ($\mathbb{I}$ is the identity matrix) and the pump vector $\vec{F} = (0, \ldots, F, \ldots, 0)$. Thus, we have

$$[H - \mathbb{E}_p - \Gamma]\,\vec{\Psi}^{ss} = -\vec{F}\,. \tag{4.5}$$

We define $\mathbb{G} = [H - \mathbb{E}_p - \Gamma]$ and, therefore, the steady-state amplitude vector can be found by:

$$\vec{\Psi}^{ss} = -\vec{F} \cdot \mathbb{G}^{-1}\,. \tag{4.6}$$

Figure 4.6(b) depicts the steady-state solution in the conditions of Fig. 4.6(a): $\tau = 12$ ps, $t = 0.18$ meV and $\bar{t} = -0.014$ meV, $\beta = 2$. It shows that the population in the pumped micropillar, marked by a circle, is almost zero, and the distribution extends mainly to the right of the excited micropillar, on the B sublattice. When moving the excitation spot to a B site [Fig. 4.6(d)], the calculated distribution reverses its decay direction, as observed in the experiment [panel (c)]. Note that along the $y$ direction, corresponding to the massive dispersion of the semi-Dirac point, the polariton distribution is localized within a single hexagon.

To provide further support to these observations, we focus on the single excitation of a B micropillar. Figure 4.7 displays Fig. 4.6(c) in linear color scale with integrated $x$ (upper panel) and $y$ (right panel) profiles. They show the emitted intensity integrated along the vertical (upper panel) and horizontal (right panel) direction within the dashed rectangles depicted in the central panel. Along the $x$ direction, the integrated profile clearly presents a much longer decay towards negative values away from the central region. Conversely, the right panel exhibits a symmetric and fast decay in the $y$ direction. Along this latter direction we expect the polariton distribution to cover mainly one hexagon [see Fig. 4.6(d)]. However, scattered light of the reflected pumping beam is also present at longer distances.

Interestingly, the observed polariton distributions resemble the predicted wavefunctions of electrons bound to a single bulk vacancy in compressed graphene [125]. The wavefunction of the vacancy state acquires an anisotropic distribution: if the vacancy is in the A sublattice, the state is localized to the right of the vacancy; if the vacancy is in the B sublattice, it is localized to the left [125]. In both cases the decay of the amplitude follows a sub-exponential decay, i.e. $1/\sqrt{|x|}$. In the case of a single bulk vacancy in unstrained graphene a defect state at the Dirac-point energy

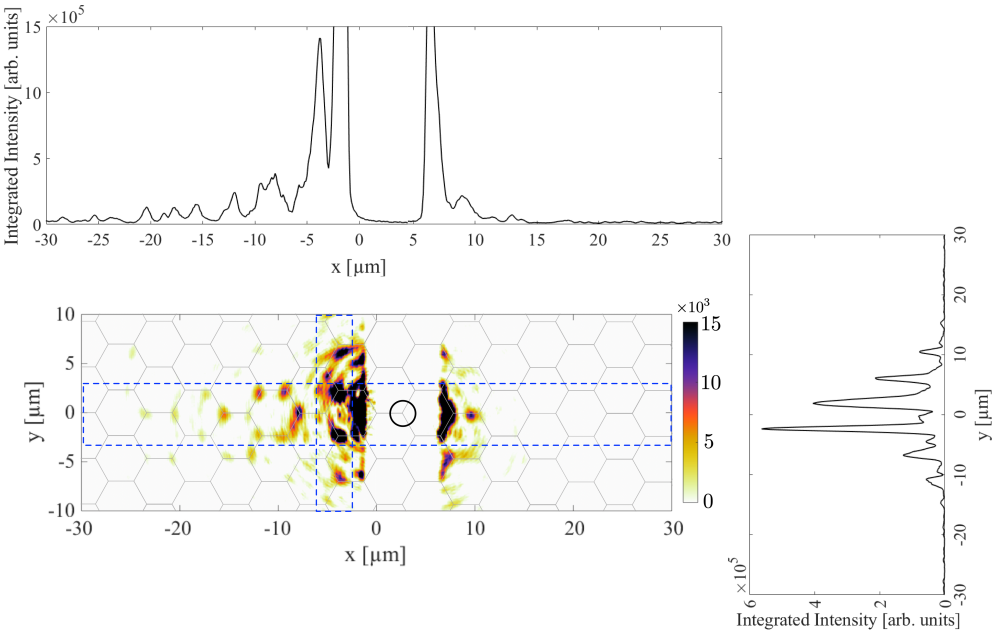


Fig. 4.7 Central panel shows Fig. 4.6(c) in linear color scale. The circle points out the pumped pillar. Top panel shows a vertical integrated plot along the $x$ direction, while the right panel shows a horizontal integrated plot along the $y$ direction. Enclosed regions depict the integrated areas.

$E_0$ also appears, with a decay in amplitude following a $1/r$ law [139, 140] isotropically in the 2D plane. The chiral symmetry of the lattice imposes that the wavefunction of the vacancy resides in one sublattice only: the sublattice opposite to that of the vacancy. These vacancy states are expected to play an important role in the transport properties of graphenelike materials in which localization by weak disorder is strongly decreased due to the Klein tunneling effect.

To experimentally evidence the vacancy-like behavior in an unstrained lattice, we perform experiments in a different sample because the shorter decay for $\beta = 1$ does not allow observing the polariton distribution with a mask in reflection (as we did for the situation of $\beta = 2$). Hence, we use a honeycomb lattice of coupled micropillars of 2.75 $\mu$m, with a center-to-center distance of 2.4 $\mu$m, which has been fabricated by etching down a planar semiconductor microcavity made of 28 (top) and 32 (bottom) pairs of $\lambda/4$ alternating layers of $Ga_{0.90}Al_{0.10}As$ and $Ga_{0.05}Al_{0.95}As$ ($\lambda = 880$ nm), a $\lambda$ spacer of GaAs, and a single 20-nm-width $In_{0.09}Ga_{0.91}As$ QW at the center of the cavity. At cryogenic temperature the lattices has a Rabi splitting of 3.5 meV. The $In_{0.09}Ga_{0.91}As$ QW allows for experiments in transmission geometry: a resonant laser beam impinges on one side of the sample and the photoluminescence is collect from the

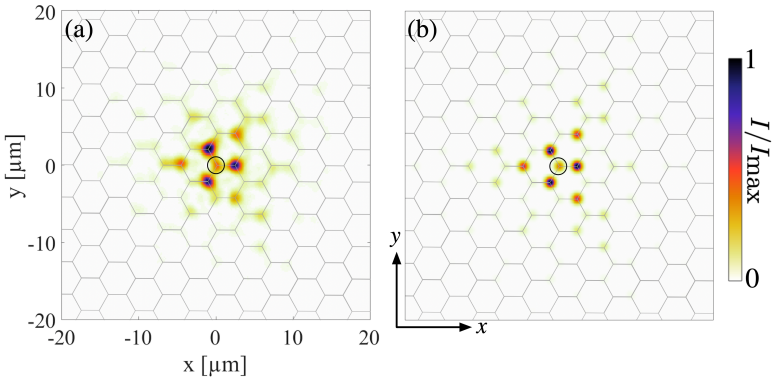


Fig. 4.8 **All-optical analog of a vacancy state in a regular honeycomb lattice** $\beta = 1$. (a) Measured photoluminescence intensity in the real space at the energy of the Dirac point $E_0$ when a single A-pillar is pumped (marked by a circle). (b) Steady-state solution of Eq. (4.3) when a single A-pillar is pumped at $E = E_0$ and considering $t = 0.23$ meV, $\beta = 1$, and $\tau = 10$ ps.

opposite side. Notice that, in this experimental situation, the pumping laser beam does not arrive at the CCD camera because it is reflected back by the sample. Figure 4.8(a) presents the emitted intensity in linear scale when a laser at the Dirac-point energy ($E_0 = 1402.54$ meV) is focused on a single micropillar of the A sublattice (marked with a black circle). The intensity distribution decays exhibiting a triangular shape with a clear predominance of the population on the B sublattice, opposite to that of the excitation beam. Some little emission is detected from A sublattice because of both the finite lifetime of polaritons and non-zero next-nearest-neighbor hoppings. In contrast to the situation for a critically compressed lattice ($\beta = 2$), the polariton steady state is here spread over $x$ and $y$ directions. Figure 4.8(b) shows the steady-state solution of Eq. (4.3) with the conditions: $E = E_0$, $t = 0.23$ meV, $\beta = 1$ and $\tau = 10$ ps.

The similarity between the measured polaritonic distribution and bound electron wavefunctions can be interpreted phenomenologically as follows. Under resonant excitation ($\hbar\omega_p = E_0$), the population of the driven micropillar interferes destructively with the laser, resulting in an almost zero population in the pumped micropillar, analogous to the effect of a vacancy. This phenomenon was recently reported in the case of two coupled micropillars [62], and it is expected to happen in any lattice of micropillars with chiral symmetry.

## 4.3 Conclusions

In summary, we have fabricated uniaxial-strain honeycomb lattices and directly observed the consequences of the Lifshitz transition in both momentum and real space. While in real space this transition is related to the disappearance of the bearded edge state, in momentum space it is related to the gap opening in between the bands. The uniaxial strain has been simulated by varying the distances among micropillars along one direction. At a critical compression, we have evidenced the simultaneous massive and massless behavior of polaritons in a semi-Dirac honeycomb lattice. Additionally, the intrinsic driven-dissipative nature of polaritons have allowed us to open up new possibilities such as the simulation of an all-optical vacancy in Dirac and semi-Dirac honeycomb lattices when a single micropillar is pumped resonantly. We have demonstrated this by reporting the polariton steady state that resembles a single-vacancy bound state in graphene.

# Chapter 5

# Drive-induced localization in dissipative lattices

Drive and dissipation are intrinsic ingredients in polariton systems. In chapter 4 we have seen that they allow revealing unexpected phenomena in periodic potential landscapes such as vacancy-like defects. When multiple drives are considered, the response of a given dissipative photonic lattice is neither trivial nor intuitive due to the existence of interference effects between the photonic bands and the driving beams. Interference effects are at the core of wave phenomena and they have been used to engineer localized modes in photonic structures. In this chapter we treat polariton lattices as a particular case of lattices of lossy resonators, and we show that the addition of external optical drives with controlled phase enlarges the possibilities of manipulating interference effects and allows designing novel types of localized modes. Using polariton honeycomb lattices resonantly driven by several laser spots at energy within the photonic bands, we experimentally demonstrate the localization of light in at-will geometries down to a single site.

One of the strategies to engineer localization of light in optics has been the use of photonic lattices. The precise control of their fabrication has enabled the engineering of localized modes by tuning different degree of freedom. Examples are the mode localized by implementing disorder lattices (phenomenon known as Anderson localization) [17, 141], the compact localized states of flat-band lattices [25, 26, 29, 142, 30, 31], the bound states in the continuum [143, 144], and localized modes in $\mathcal{PT}$-symmetric lattices [145]. Futhermore, localized modes in the gap of a photonic band structure can be done when a local potential is added to the subjacent periodic structure, being the principle of photonic crystal cavities and Tamm modes at the surface of a photonic system [146–148]. Recently, the use of lattices with non-trivial topological bands has offered new

possibilities to implement localized modes. They are exponentially localized on the edges and/or the corners of the lattices with the great asset that both their existence and optical frequency are protected from certain types of disorder [2, 149–152, 4–6, 54].

One of the characteristics of the localized modes that are mentioned above is that their localization length is usually larger than a single site. The localization length of the bound states in the continuum covers several lattice sites [153], and disordered lattices also create the conditions for having trapped light on few sites. In the case of the compact states in flat-band lattices, they arise from the interference between at least two lattice sites with non-zero amplitude and opposite phases [154, 27], which can be added to form arbitrary light patterns with arbitrary sizes [30]. In all these cases, the localized modes are eigenmodes of the system, whose amplitude distribution is independent of the external excitation conditions. This mean that the design of the lattice, that is, the geometry of the dielectric structure, set the location, shape and extension of the localized modes. Therefore, once the lattice is fabricated the localization properties are hardly adjustable.

It would be convenient to engineer reconfigurable localized modes with no dependency on the lattice geometry because it would allow designing on-demand localization in any lattice with a fully external control. In this chapter, we show a very efficient method based on drive and dissipation that enables localization in arbitrary lattices.

## 5.1 Localization by drive and dissipation in 1D

In order to demonstrate the principle of localization by drive and dissipation, we consider a lattice of coupled photonic resonators. Each of them is subject to radiative losses to the environment and can be driven by an external laser (coherent field). An archetypical system implementing this situation is a lattice of coupled semiconductor micropillars. The dynamics of the photon field in this lattice in the tight-binding limit can be described by the following set of equations [78]:

$$i\hbar\frac{\partial\psi_n}{\partial t} = E_n\psi_n + \sum_{n\neq m} t_{n,m}\psi_m - i\frac{\hbar}{\tau}\psi_n + F_n e^{-i\omega_p t}\,. \tag{5.1}$$

$\psi_n$ is the field amplitude at the center of $n$-th micropillar, $E_n = E_0$ is the energy of considered mode in each micropillar (assumed to be identical for all sites), $t_{n,m}$ is the coupling matrix and encode the lattice geometry, $\tau$ is the radiative photon lifetime in each micropillar, and $F_n$ is the complex amplitude of the resonant excitation laser at the $n$-th site with photon energy $\hbar\omega_p$.

Let us firstly consider the simplest case, a one-dimensional (1D) lattice of coupled micropillars that is shown in Fig. 5.1(a). Considering an infinite lattice with only nearest-neighbor hoppings $t_{m+1} = t_{m-1} = t$, the photonic band of this lattice can be obtained by using a stationary *ansatz* of the form: $\psi_n(t) = \psi_n e^{iEt/\hbar}$. Thus, the photonic band has the form

$$E(k) = E_0 - 2t\cos(ka)\,, \tag{5.2}$$

where $a$ is the lattice constant and $k$ is the wavevector along the lattice direction. Notice that in order to obtain the band we have neglected the dissipation. Figure 5.1(a) depicts this photonic band structure, which is centered at energy $E_0$. For a finite lattice case there are as many equations as lattice sites, therefore, a large eigensystem problem needs to be solved numerically. Figure 5.1(b) shows the eigenvalues and their respective energies when a finite lattice composed of 200 sites is considered. It can be seen that the numerical band reproduces the sinusoidal shape of the photonic band in the infinite case.

When drive and dissipation are considered, Eq. (5.1) has a family of localized solutions for specific spatial configurations of the driving field $F_n$ in the stationary state. To show this we compute the stationary state of Eq. (5.1) when implementing different configuration of the drives, considering $\tau = 10\hbar/t$. We compute the stationary state by multiplying the pump vector with the inverted matrix of $\mathbb{G}$, which is the matrix composed of the hoppings, the dissipation and the pumping energy [see Eq. (4.6)]. Figure 5.1(c) displays the case when a single micropillar in the center of the finite lattices is pumped by a laser at the frequency $\omega_p = E_0/\hbar$, at the middle energy of the photonic band. As it can be observed, the stationary state extends over many lattice sites on the order of $t\tau/\hbar$. This delocalized behavior is found for any frequency of the pumping beam within the band but with different extensions. This can be quantified using the inverse participation ratio, which is defined as

$$\mathrm{IPR} \equiv \frac{\sum_n |\psi_n|^4}{\left(\sum_n |\psi_n|^2\right)^2}\,. \tag{5.3}$$

It has a value equal to 1 for a stationary state fully localized on one site and it tends to $1/L$ for extended modes in a finite lattice of $L$ sites. Figure 5.1(d) presents the IPR of the stationary-state solution of Eq. (5.1) when the frequency of driving laser scans the entire photonic band, showing that the stationary states are delocalized at any energy.

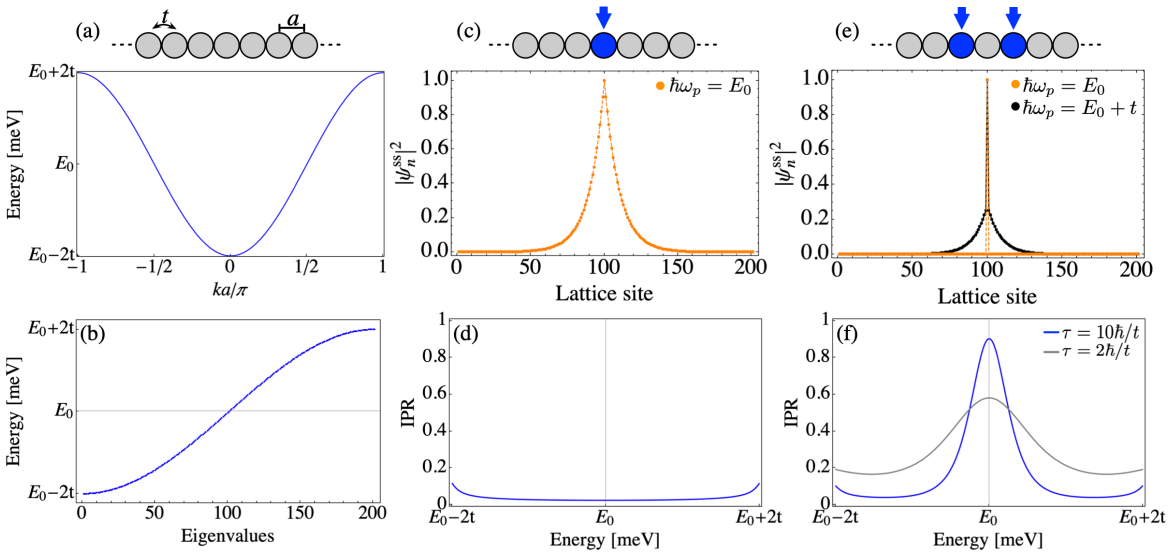


Fig. 5.1 **Localized modes in a one-dimensional driven-dissipative lattice**. (a) Tight-binding band structure of an infinite one-dimensional lattice of coupled resonators with center-to-center distance $a$ and nearest-neighbor hopping $t$. (b) Energy eigenvalues of a tight-binding 1D lattice of 200 sites. $E_0$ is the mid-band energy. (c)-(e) Normalized intensity profile of a stationary-state solution of Eq. (5.1) when the lattice is resonantly driven by a laser beam located at a single site (c) and two laser beams enclosing a single site (e) at a mid-band energy $E_0$. In panel (e) the stationary-state solution is also shown in the case when the driving laser beams have an energy away from the resonance, i.e. $\hbar\omega_p = E_0 + t$.(d)-(f) Inverse participation ratio (IPR) of the stationary-state solutions when the lattice is resonantly driven by a laser beam (d) and two laser beams (f) at every energy within the band. In panel (f), the IPR is computed considering two values of the lifetime $\tau$.

The response of the lattice changes drastically when two pumps with equal phase and amplitude at $\hbar\omega_p = E_0$ drive two sites surrounding a single one [see sketch of Fig. 5.1(e)], the stationary state is almost fully localized at the surrounded site as shown in Fig. 5.1(e). The field intensity in the pumped sites is almost zero, as well as in all sites located out of the region defined by the two pumps (it tends strictly to zero for long lifetimes, i.e., $\hbar/\tau \ll t$). Conversely, the localized response of the lattice is lost when the frequency of the drives is shifted from $E_0$ to any energy. This case can be seen in Fig. 5.1(e), in which the amplitude profile of the stationary states exhibits a slow decay out of the central peak depicted by black dots. As a result, a resonance takes place only when the frequency of the driving laser is the same than the one of the resonators. This is confirmed by the peak of the stationary-state IPR at the energy $E_0$,

however, the strong localization can be damaged by shorter lifetimes (higher losses) [see Fig. 5.1(f)].

In order to obtain further insight into the nature of this localization, let us consider Eq. (5.1) in the rotating frame of the pump frequency $\omega_p$ and in the limit of losses much weaker than the hopping $t$, i.e., $\hbar/\tau \ll t$. By doing so, the term related to the losses in the equation can be neglected and Eq. (5.1) takes the form:

$$\Delta\psi_n + \sum_m t_{n,m}\psi_m = -F_n\,, \tag{5.4}$$

where $\Delta = E_0 - \hbar\omega_p$ is the detuning between the onsite energy of the resonators and the driving energy. Considering two pumping beams placed at sites $N-1$ and $N+1$ (being the site $N$ the center of the lattice) with amplitudes are $F_{N-1}$ and $F_{N+1}$, we can write Eq. (5.4) for a few lattice sites around the drives:

$$\begin{aligned}
\Delta\psi_N + t(\psi_{N-1} + \psi_{N+1}) &= 0 && (5.5)\\
\Delta\psi_{N-1} + t(\psi_{N-2} + \psi_N) &= -F_{N-1} && (5.6)\\
\Delta\psi_{N+1} + t(\psi_N + \psi_{N+2}) &= -F_{N+1} && (5.7)\\
\Delta\psi_{N+2} + t(\psi_{N+1} + \psi_{N+3}) &= 0 && (5.8)\\
\Delta\psi_{N+3} + t(\psi_{N+2} + \psi_{N+4}) &= 0 && (5.9)\\
\Delta\psi_{N+4} + t(\psi_{N+3} + \psi_{N+5}) &= 0 && (5.10)\\
\Delta\psi_{N+5} + t(\psi_{N+4} + \psi_{N+6}) &= 0 && (5.11)
\end{aligned}$$

Looking for solutions for which the driven sites $N \pm 1$ have zero amplitude, $\psi_{N\pm1} = 0$, Eq. (5.5) implies that $\Delta = 0$. If this is so, from Eq. (5.8) we obtain that $\psi_{N+3}$ must be zero. Subsequently, Eq. (5.10) results in $\psi_{N+5} = 0$ and this happens for all the sites $n = N \pm 2m + 1$, with $m \in \mathbb{N}$. Therefore, every site separated by an odd number of pillars from the central site $N$ must have zero amplitude. Additionally, from Eq. (5.9) and (5.11) with $\Delta = 0$, we get $\psi_{N\pm2m} = -\psi_{N\pm2m+2}$. Consequently, all these sites have the same amplitude. On the other hand, inspecting the last site of the lattice, we have

$$\Delta\psi_L + t\psi_{L-1} = 0\,. \tag{5.12}$$

Then, assuming that this site is an odd one, the site placed at $L-1$ is hence even. Because of $\Delta = 0$, Eq. (5.12) gives that $\psi_{L-1} = 0$ and, thus, the amplitudes of all even sites also vanish. Finally, taking all this into account, from Eqs. (5.6) and (5.7) we

obtain

$$\psi_N = -F_{N-1}/t \; ; \; \psi_N = -F_{N+1}/t \implies F_{N-1} = F_{N+1} \, . \tag{5.13}$$

This means that the pumping beams on the two sites surrounding the $N$ site must have both equal amplitude and phase in order for the destructive interference effect away from the $N$ site to take place.

From this analysis we can draw two main conclusions. First, searching for stationary-state solutions that have zero amplitude on the driven sites leads to the fact that the frequency of the drives must coincide with the onsite energy of the surrounded site as if it were detached from the lattice, which is indeed a resonance effect. Second, assuming the null amplitude on the driven sites results in the vanishing of the amplitude for all other sites of the lattice except from the surrounded one, meaning that the presence of the localized mode is independent of the lattice size out of the enclosed region. As a final remark, we can interpreted this phenomenon as if the effect of the drives at the localization resonant energy was to detach or isolate the surrounded site from the rest of the lattice.

### 5.1.1 Multiple energy localization or resonances

These arguments also apply when the drives reside in sites further than two sites away. Figure 5.2 shows several cases along with the respective IPR of the stationary state as a function of the pumping energy within the photonic band. When the pumping beams enclose a region of two sites [see Fig. 5.2(a)], the localized modes appear at energies $\Delta$ corresponding to the eigenenergies of two isolated coupled sites (a dimer): $\Delta = -t$ and $\Delta = t$. Both amplitude and phase of the drives must respect the phase distribution of the dimer modes: for $\Delta = -t$ (bonding mode) $F_2 = F_1$; for $\Delta = t$ (antibonding mode) $F_2 = -F_1$. Figures 5.2(b) presents the case when considering three-sites distance among the pumping beams and, as a result, three resonances appear: at $\Delta = \pm\sqrt{2}t$ when the two pumps are in phase, and at $\Delta = 0$ when the two pumps are out of phase. Likewise, four resonances emerge when a four-sites configuration is implemented as shown in Fig. 5.2(c); for in-phase pumps the resonances occur at $\Delta = -t(\sqrt{5}+1)/2$ and $\Delta = t(\sqrt{5}-1)/2$, for out-of-phase pumps they happen at $\Delta = -t(\sqrt{5}-1)/2$ and $\Delta = t(\sqrt{5}+1)/2$. Remarkably, the localized resonances take place with energies given by the eigenstates of the chain in-between the pumps, as if it were completely detached from the lattice. This is a consequence of the fact that at the resonances, the amplitude at the pumped resonators is approximatively zero.

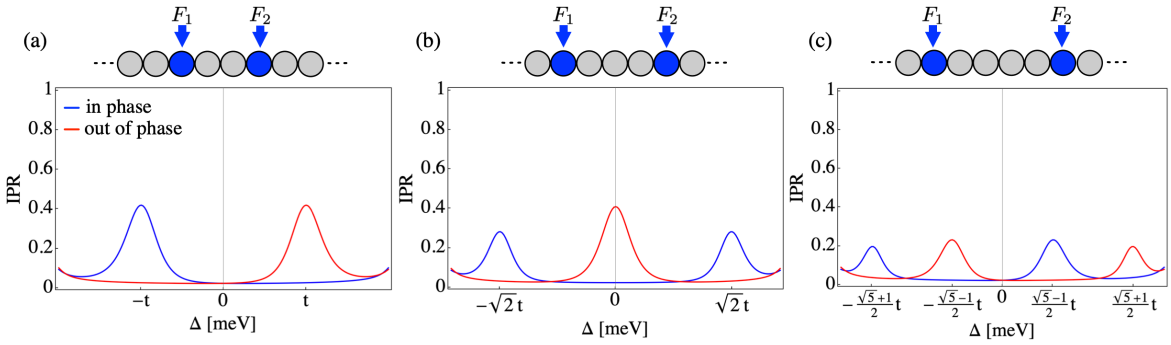


Fig. 5.2 **Generation of multiple localized modes in a one-dimensional driven-dissipative lattice**. Scheme of the driving pump separated by (a) 2, (b) 3 and (c) 4 sites. Lower panels exhibit the IPR as a function of the detuning between the onsite energy and the energy of the pumping laser, $\Delta$ parameter. Blue (red) curve corresponds to the case when the two pumping beams have the same (opposite) phase.

### 5.1.2 Shifting the energy of localization or resonance

Intriguing behavior of the resonances happens when considering an extra pumping beam in the driving configuration of two pumps separated by a single site. We address the situation by considering $F_{N-1} = F_{N+1} = F$ and the additional pump on site $N$ (surrounded site) having the same photon frequency $\omega_p$ with amplitude $G_N$ [see top panel of Fig. 5.3]. Equations (5.6) to (5.11) remain intact, while Eq. (5.5) now reads

$$\Delta\psi_N + t(\psi_{N-1} + \psi_{N+1}) = -G_N\,. \tag{5.14}$$

Imposing the condition of zero amplitude on the driven sites, $\psi_{N-1} = \psi_{N+1} = 0$, we obtain $\psi_N = -G_N/\Delta$. Inserting this into Eq. (5.7) gives

$$G_N = \frac{\Delta F_{N+1}}{t} + \psi_{N+2}\,. \tag{5.15}$$

$\psi_{N+2}$ is the amplitude of a site out of the region in-between the drives and its value is equal to zero due to similar arguments mentioned above. Thus, the value of the detuning $\Delta$ for localization is directly proportional to the amplitude of the pumping beam at the $N$ site:

$$\Delta = \frac{G_N}{F}t\,. \tag{5.16}$$

Consequently, the photon energy $\hbar\omega_p = \Delta + E_0$ of the driving field at which localization happens in a single site can be shifted by adding an extra beam of amplitude $G_N$ at the site surrounded by the main driving beams. If this extra beam is in phase with the pumps $F$, the resonance energy moves to higher $\Delta$, i.e. higher

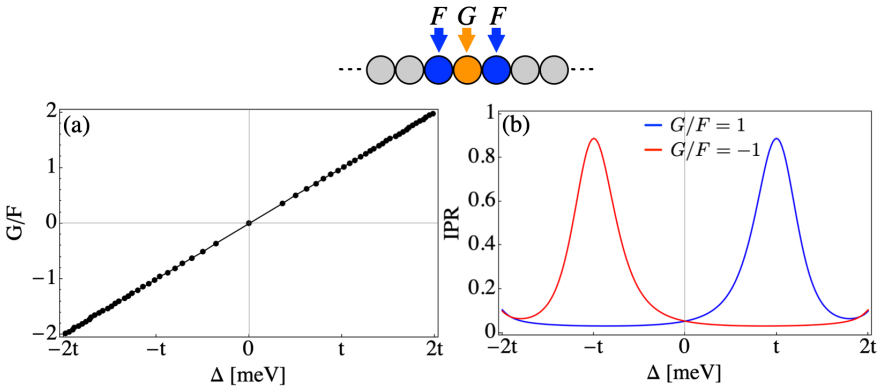


Fig. 5.3 **Shifting the energy of the localized mode in a one-dimensional driven-dissipative lattice**. Top panel shows a scheme of the driving pump configuration in the lattice. (a) Photon energy of the IPR peak for the pumping configuration shown in top panel. Vertical axis corresponds to the amplitude ration between the surrounding pumps $F$ and the surrounded one $G$, while horizontal axis is the detuning energy $\Delta$. Positive (negative) values in vertical axis indicate a zero ($\pi$) phase between the inner and outer drives. (b) Two representative values of the ratio between the pumping amplitudes, red line for $G/F = -1$ and blue line for $G/F = 1$.

energies, whereas an out of phase configuration shifts the resonance condition to lower energies. The additional drive $G_N$ acts as a renormalized onsite energy for the isolated site. This is evidenced in Fig. 5.3 where the pumping configuration is composed by three drives; two of them with amplitude $F$, which define the surrounded region (cavity); and the other with amplitude $G$ on top of the site where the localization takes place. The scanning of the photon energy within the band considering several ratios of the amplitudes ($G/F$) produces the energy shift of the highest localized mode as shown in Fig. 5.3(a). As analytically proved, the energy shift depends linearly on the ratio of the amplitudes $G/F$. Two IPR curves for $G/F = \pm 1$ are presented in Fig. 5.3(b), where the IPR peak moves to $\Delta = \pm t$, respectively.

## 5.2 Localization by drive and dissipation in 2D

The response of a 1D lattice we have just analyzed can be generalized to driven-dissipative lattices of higher dimensions. To explicitly show this, we consider a two-dimensional (2D) toy model known as square lattice, which is shown in Fig. 5.4(a). This lattice has a unit cell composed by one single site that has four nearest neighbors at a distance $a$. In the tight-binding picture, the photonic band of an infinite square

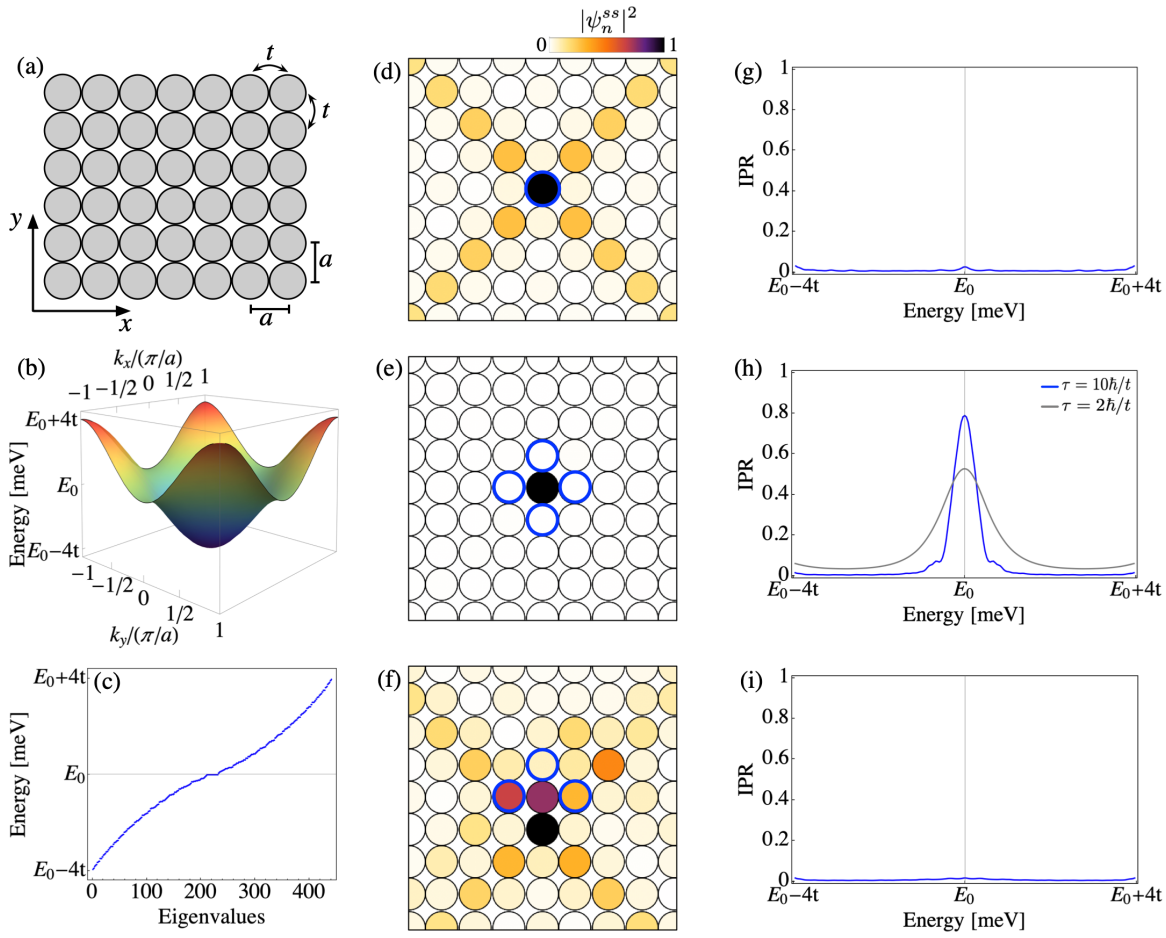


Fig. 5.4 **Localized modes in a two-dimensional square driven-dissipative lattice**. (a) Scheme of a two-dimensional lattice of coupled resonators with center-to-center distance $a$ and nearest-neighbor hopping $t$. (b) Tight-binding band structure of an infinite two-dimensional square lattice. (c) Energy eigenvalues of a tight-binding 2D square lattice of $21 \times 21$ sites. $E_0$ is the mid-band energy. (d)-(f) Normalized intensity of a stationary-state solution of Eq. (5.1) driven by one (d), four (e), and three (f) laser beams (blue circles) with energy $\hbar\omega_p = E_0$ and with identical phases. (g)-(i) IPR of the stationary-state solutions when the square lattice is resonantly driven by one (g), four (h), and three (i) laser beams at every energy within the band. In panel (h), the IPR is computed considering two values of the lifetime $\tau$.

lattice is:

$$E(\vec{k}) = E_0 - 2t\left[\cos(k_x a) + \cos(k_y a)\right] , \tag{5.17}$$

where $t$ is the hopping energy among nearest-neighbor sites and $\vec{k}$ is the wavevector. The band structure is presented in Fig. 5.4(b), it is centered around $E_0$, which is the onsite energy of a given mode in the resonator (we again assume every mode in all sites has the same energy). For a finite square lattice, eigenvalues are found numerically

by solving the set of Eqs. (5.1) without considering the losses, and they are shown in Fig. 5.4(c) when a lattice of $21 \times 21$ sites is considered.

In order to probe the response of the square lattice under the driving of a single resonator, we look for the stationary-state solution of Eq. (5.1) when an optical field of frequency $\omega_p = E_0/\hbar$ pumps the center of the lattice. Figure 5.4(d) presents the expected emission from the lattice (blue circle depicts the driven site), which extends over many sites and, therefore, is completely delocalized as in the 1D-lattice case. By scanning the entire photonic band with the driving field no localized modes are found. The computation of the stationary-state IPR shown in Fig. 5.4(g) is almost flat near zero values and it has a very small increase at $E_0$ energy, which is related to the presence of a saddle point at the mid-band energy. Then, we search for localized solution of Eq. (5.1) using a multiple pumps configuration. As we mentioned in the 1D case, the key ingredients of the drive-induced localization is that the pumping field must enclose a single site (o a region of the lattice) and they must have the same amplitude. Figure 5.4(e) displays the stationary-state solution when performing an in-phase four-pumping configuration (blue circles) such that they surround a single resonator in the center of a square lattice. A localized response at $\hbar\omega_p = E_0$, down to a single site, is obtained with almost zero amplitude in the pumped sites and in the sites away from the pumped region. This resonant behavior occurs around the onsite energy of the resonator, as it can be observed in the IPR curve shown in Fig. 5.4(h). For smaller lifetimes the highest value of the IPR decreases (similar to the 1D-lattice case), but it is still very strong, even for losses on the order of the hopping. As a counterexample, Figure 5.4(f) show the expected emission when the pump spots at $\hbar\omega_p = E_0$ do not fully surround a single resonator. In this situation, the real-space distribution of the field does not show any confined response at $E_0$ or at any other laser energy as shown by the respective IPR curve in Fig. 5.4(i).

## 5.3 Experimental realization

Lattices of semiconductor micropillars are intrinsically dissipative and can be easily driven by external lasers using a standard optical setup. Therefore, they are an ideal platform to probe the concept of localization we just introduced. In order to carry out the experiments, we use coupled micropillars of $2.75\,\mu$m in diameter arranged in a honeycomb geometry with a lattice constant of $a = 2.3\,\mu$m. As we previously mentioned, this lattice is etched from a planar semiconductor microcavity that, in this case, is made of two AlGaAs Bragg mirrors embedding a GaAs cavity spacer

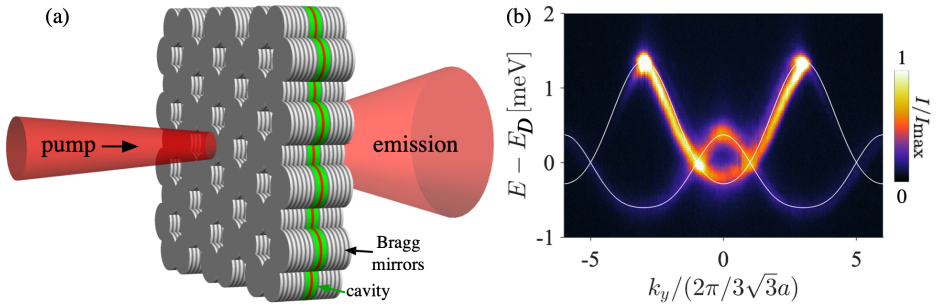


Fig. 5.5 **Transmission experiments in a photonic honeycomb lattice**. (a) Scheme of the honeycomb lattice of micropillar and of the excitation (left) and emission (right) beams, which is known as transmission geometry setup. (b) Measured angle-resolved photoluminescence of the lattice showing the lowest energy bands as a function of the in-plane momentum $k_y$ for $k_x = 2\pi/3a$, with $a = 2.3\,\mu$m the center-to-center separation among adjacent micropillars and $E_D = 1391.7$ meV. White line represent the tight-binding fit.

and a single 20-mm-width InGaAs quantum well (QW) at the center of the cavity. The whole heterostructure is grown on an epitaxial quality GaAs substrate. Since the drive-induced localization is a purely photonic phenomena, we use a region of the wafer in which the lowest photonic modes are red-detuned by 18 meV from the QW exciton resonance at 1409.9 meV at 6 K. This detuning is much larger than the Rabi splitting 3.5 meV and implies a predominant photonic component of 99%. Hence, all the effects reported here can in principle be observed in structures without excitonic resonances. Because the substrate is transparent with negligible absorption at the working wavelengths, experiments in transmission geometry are possible: the vertically polarized laser impinges the sample on the epitaxial side and collection of the emitted co-polarized photons is done from the opposite side as shown schematically in Fig. 5.5(a). Angle-resolved photoluminescence experiments with an out-of-resonant laser excitation at 1535 meV in a 2.3 $\mu$m spot (FWHM) centered on top of a micropillar reveal the two lowest energy bands of the structure [see Fig. 5.5(b)]. As it is mentioned in chapter 4, this dispersion exhibits two Dirac crossings that are the signature of honeycomb lattices [12], and no significant polarization splitting is observed in these photonic bands. Furthermore, the fitting of the measured bands to the tight-binding model gives us a the values of the nearest-neighbor and next-nearest-neighbor hoppings, $t = 328\,\mu$eV and $\bar{t} = -42\,\mu$eV, respectively, with $E_D = 1391.7$ meV the emission energy at the Dirac crossings.

We firstly explore the response of the lattice when a single micropillar is resonantly driven at energy $E_D$. The wavelength of the laser is set by a wavemeter with a precision

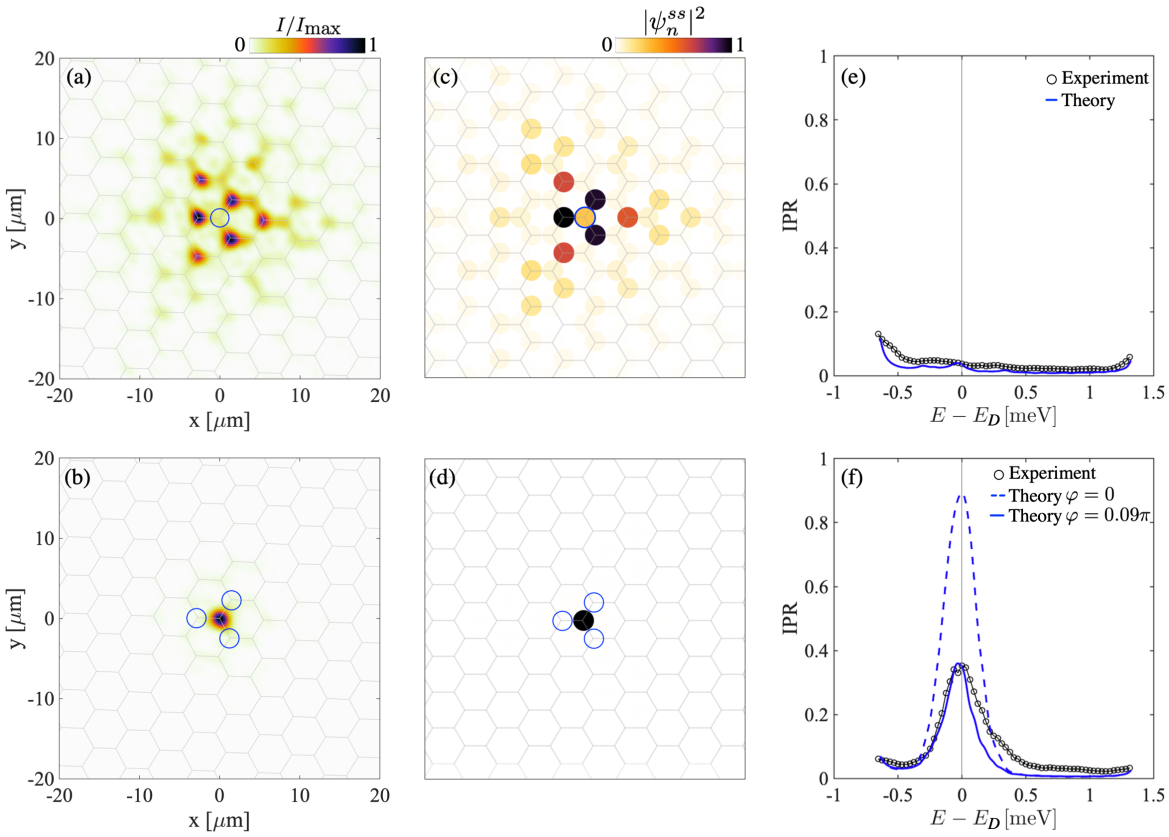


Fig. 5.6 **Resonant drive of a honeycomb lattice**. (a) Measured real-space emission when driving the micropillar marked with a blue circle with a laser beam at $\hbar\omega_p = E_D$. $E_D = 1391.7$ meV. The center of each micropillar is located at the corner of the gray hexagon pattern. (b) Same than (a) when driving three micropillars with equal amplitude and phase enclosing a central one. (c) and (d) Simulated real-space emission using the experimental conditions shown in panel (a) and (b), respectively. (e) and (f) Experimental (black circle) and simulated (blue line) IPR curve when driving a single micropillar at a number of energy in the bands. In panel (f) the dashed blue line considers a computation with three laser beams having a phase difference of $\varphi = 0.09\pi$ between each other.

of 0.1nm. Figure 5.6(a) presents the collected emission in this situation (blue circle depicts the pumped micropillar) that extends away from the pump spot resembling the wavefunction of a bound state of a single vacancy in actual graphene[1]. Remarkably, the pumped site shows almost null intensity. As mentioned in chapter 4, this peculiar response is a consequence of the interference effect at the pumped site between the laser and polariton population of the pumped site, which was already noticed in a

[1]Note that this phenomenon is also shown in chapter 4 and, in those experiments, the selected region of the wafer had a less negative exciton-photon detuning (polaritons with more excitonic content).

simpler case of two coupled micropillars pumped at the energy right in between the bonding and antibonding modes [62].

The photon field distribution is very different when three laser beams of same amplitude and phase drive the lattice at $E_D$. The three laser configuration are placed in a triangular geometry surrounding a single micropillar and it is generated thanks to a spatial light modulator SLM (see appendix B for details). Figure 5.6(b) reports the emission in this scenario. Similar to the stationary-state emission from a square lattice shown in Fig. 5.4(e), the field distribution is strongly localized in the micropillar surrounded by the three drives and no significant emission from other micropillars of the lattice is observed (including the pumped sites). These spatial distributions of the photon field are accurately described by Eq. (5.1) and considering the experimental hopping parameters, the pumping energy $E_D$ and a lifetime $\tau = 9$ ps. Thus, their respective stationary-state solution are presented in Fig. 5.6(c)-(d).

To quantitatively characterize this localized response, we compute the IPR [Eq. (5.3)] for the emission in the three-pumps configuration when the laser photon energy sweeps the whole Dirac bands. Fig. 5.6(f) present the measured IPR at the different energies with dots. This quantity is computed from the emission measured at the center of each micropillar. The highest localized emission is detected at the energy of the Dirac point $E_D$, having a value of IPR$= 0.35$. This photon energy is very close to the estimated eigenenergy $E_0$ of the fundamental mode of a single detached micropillar ($E_D = E_0 + 3\bar{t}$), and they would both coincide exactly in the absence of next-nerarest-neighbor coupling. The numerical IPR is displayed in dashed blue lines in Fig. 5.6(f) and predicts a value of IPR$= 0.89$ for the polariton lifetime measured in the lattice. The difference with the value of 0.35 in the experiments arises from an horizontal tilt of the incident beams, which induces an estimated phase shift of about $0.09\pi$ between three consecutive spots. The solid blue line in Fig. 5.6(f) takes into account this fact and it reproduces the measured IPR at $E_D$. In contrast, Fig. 5.6(e) shows that for a single spot excitation, the transmitted signal is extended over many lattice sites for any photon energy resulting in very low IPR values.

The presented three-pumps configuration can be used as a building block to engineer localization in as many sites as it is desired and, therefore, to build up any at-will intensity pattern in the lattice. For example, Figure 5.7(a) exhibits the emission when three overlapping building blocks in a triangular shape (blue circles) pump the lattice. A localized intensity pattern is observed that mostly occupies three sites in-between the pump spots and forms a staggered triangle. Numerical solution of Eq. (5.1), considering

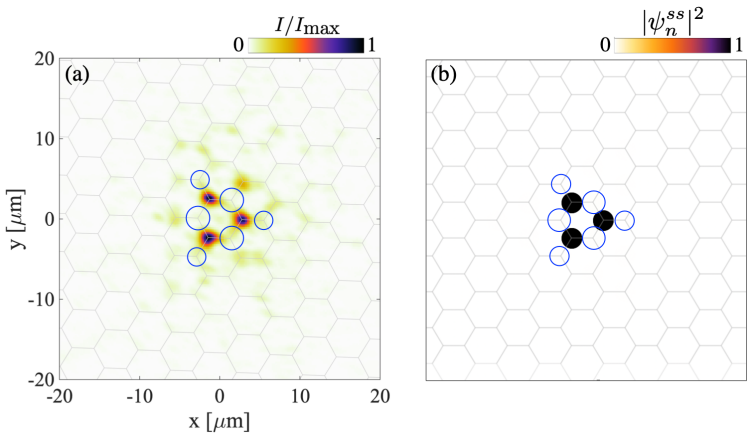


Fig. 5.7 **Multiple localization in a honeycomb lattice**. (a) Optical response of the honeycomb lattice when arranging three times the localization building block shown in Fig. 5.6(b) to implement a triangle. Large circles indicate laser spots having twice the intensity of the ones indicated with small circles. (b) Simulated optical response in the experimental condition of (a).

this pump configuration and the experimental conditions, reproduces the multiple localized response of the honeycomb lattice [see Fig. 5.7(b)].

Additionally, we also explore experimentally the case of multiple resonances as we presented in the 1D-lattice case (see Fig. 5.2). As we mentioned, the resonant localized modes appear at the molecular eigenenergies of the enclosed region. Thus, in the honeycomb lattice, we generate a pumping configuration of four drives with equal amplitude and phase such that it surrounds completely two adjacent micropillars of the lattice, as depicted by blue circles in Fig 5.8(a). In that configuration, we expect the appearance of a localized mode at the energy of the bonding state of a dimer, $\hbar\omega_p = E_D - t$, if the hopping among next-nearest neighbors is not taken into account. Figure 5.8(a) reports the emission at $\hbar\omega_p = E_D - 0.36$ meV, which corresponds to the highest localization of the experimental IPR when the laser energy scans from the bottom of the photonic bands up to $E_D + 0.7$ meV [see top panel of Fig. 5.8(c)]. Residual scattered light forbids a confident measurement of the IPR for higher photon energies. Despite the low value of the measured IPR ($\sim 0.08$), caused by a residual misalignment of the excitation spots, the emission is mostly localized in the two surrounded micropillars having a bonding-like mode shape (some light is also observed in micropillars near the pumping region). Under a perfect alignment and considering next-nearest-neighbor hopping, the expected IPR value goes up to 0.32 at $\hbar\omega_p = E_D - 0.407$ meV [see bottom panel of Fig. 5.8(c)], energy that slightly differs from the measured one by about 15% of $t$. Figure 5.8(b) shows the expected emission

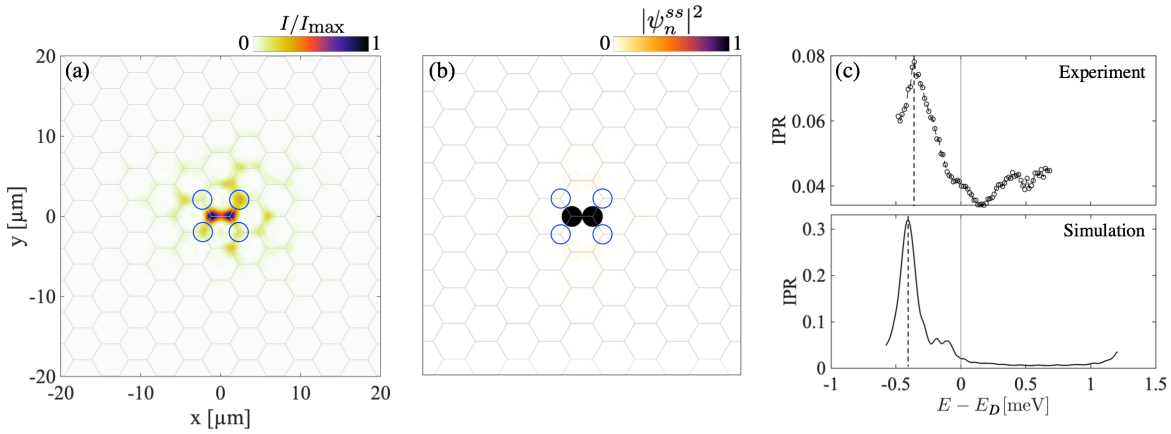


Fig. 5.8 **Localized bonding mode in a honeycomb lattice** (a) Emitted intensity at the IPR peak, $\hbar\omega_p = E_D - 0.36$ meV, in top panel of (c) when four driving beams of nominally the same amplitude and phase demarcate a two-site molecule or dimer. Blue circles denote the driven sites. (b) Stationary-state solution of Eq. (5.1) with the same experimental conditions than (a) at the IPR peak of bottom panel of (c): $\hbar\omega_p = E_D - 0.407$ meV. (c)-top experimental IPR of the emission as a function of the energy within the photonic bands. For photon energies above $E_D + 0.7$ meV residual scattered light prevent a confident measurement of the IPR. (c)-bottom Simulated IPR in the case of perfect alignment. Dashed line in every panel points out the energy of the highest IPR value.

that is highly localized in the surrounded micropillars. Although the mismatch between the energy of the experimental and simulated IPR peak is small, it is worth to mention that the presence of on-site energy disorder in the lattice may cause a slight energy shift of the IPR peak.

As demonstrated in the 1D-lattice case, the resonant energies at which the localized modes appear are determined by the eigenenergies of the optically defined cavities (region surrounded by the drives) as if they were completely detached from the lattice. We analytically and numerically showed that the resonant energy can be modified when adding an extra drive on top of the sites surrounded by the main drives. Here, we experimentally demonstrate this effect in 2D by considering the simplest situation of three identical pumps that induce a localization in a single site [see Fig. 5.6(b)]. On top of this site, we add an additional drive of the same frequency as the surrounding pumps. Remarkably, the frequency (or energy) of the localized mode can be shifted at any energy within the photonic bands when changing the relative intensity and phase between the added spot $|F_{in}|^2$ compared to that of the surrounding spots $|F_{out}|^2$, as shown in simulations in Fig. 5.9(a). The relative phase between the outer and inner

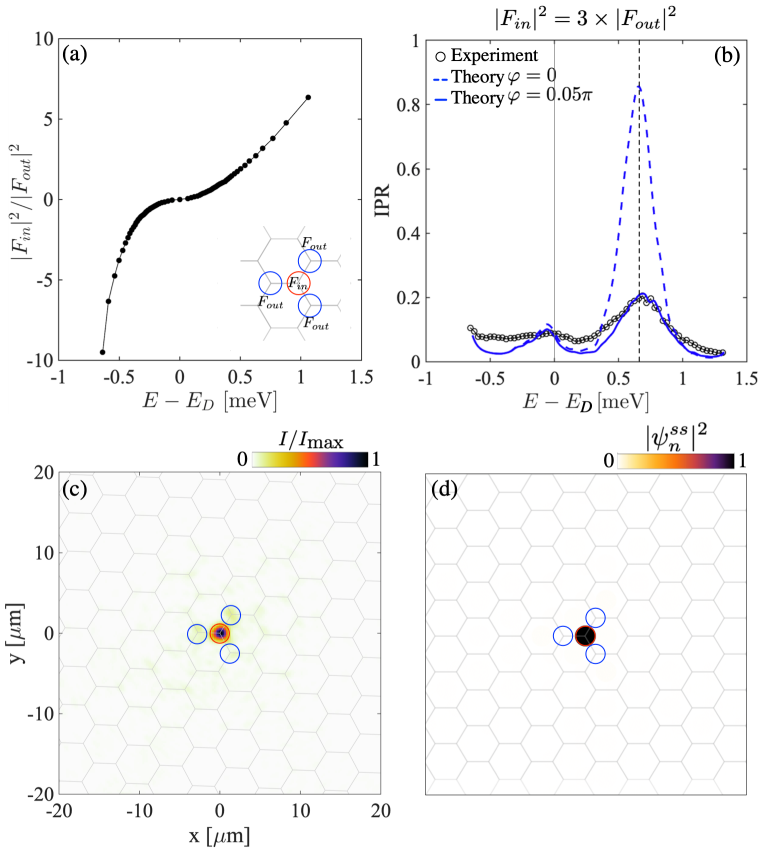


Fig. 5.9 **Shifting the energy of the localized mode in a honeycomb lattice** (a) Calculated photon energy of the IPR peak for a pumping configuration of four drives shown in inset. The vertical axis corresponds to the intensity ratio between the inner spot $|F_{in}|^2$ and the outer spots $|F_{out}|^2$. The sign denotes the relative phase between the inner and the outer spots: positive (negative) means zero ($\pi$) phase. (b) Measured IPR (dots) when scanning the laser frequency in the configuration of the inset in (a) for $|F_{in}|^2 = 3 \times |F_{out}|^2$. The continuous blue line is the calculated IPR using the photon lifetime of the lattice and equal phase for the four spots, while the dashed blue line includes a phase difference of $0.05\pi$ for one of the outer spots. (c) Real-space emission measured at the the energy of the IPR peak in (b), $E - E_D = 0.69$ meV. The pumping intensity on micropillars denoted by blue circles is three times smaller than the intensity on the micropillar denoted by red circle. (b) Simulated emission considering the experimental conditions of (c) and the scenario of perfect alignment.

beams determines if the resonance moves towards negative or positive energies: a relative phase of $\pi$ (0) shift the energy to negative (positive) values.

In order to demonstrate this energy shift in the experiment, we consider the particular case in which the surrounding pumps (blue circles) possess an intensity three times smaller than the surrounded one, $|F_{in}|^2 = 3 \times |F_{out}|^2$. Performing the photon

energy scan throughout the photonic bands and collecting the emitted intensity, the experimental IPR curve is computed. This is displayed in Fig. 5.9(b) by unfilled dots. A peak at $\hbar\omega_p = E_D + 0.69$ meV reveals a localized mode on the surrounded micropillar as shown in Fig. 5.9(c). The measured IPR$\sim 0.2$ is about four times lower than the expected IPR [dashed blue line in Fig. 5.9(b)], when no phase between the drives is taken into account. The expected localized mode is presented in Fig. 5.9(d) and it exhibits an extreme localization on the surrounded micropillar without any noticeable emission on other micropillars. Conversely, the measured IPR is well reproduced by simulations if the pumping configuration has a phase mismatch of $\varphi = 0.05\pi$ between the drives $F_{out}$ [solid blue line in Fig. 5.9(b)]. It is worth to mention that the lifetime does not play a major role in the energy shift of the resonance, however, as we already saw, it has a considerable impact on the degree of localization, the IPR maximum is strongly modified when varying the lifetime.

## 5.4 Conclusions

We have predicted and experimentally demonstrated the formation of highly localized modes in photonic lattices made of coupled dissipative resonators. Thanks to the interplay between dissipation and judicious driving configurations, the induced localization can be implemented down to a single site in 1D or 2D lattices with any geometry. The localized modes appear due to the interference between the polariton distributions created by each drive, which is constructive on the surrounded resonator and destructive elsewhere, and their energies reside within the bands. Advantageously, this drive-induced localization in lattices of dissipative resonators allows to design localized emission pattern in a reconfigurable manner with high flexibility, which may useful for locally enhancing nonlinear effects and the control of light-matter interactions that require single site excitation.

Furthermore, the localized resonance reported in this chapter has intriguing similarities with the radiation of quantum emitters coupled to photonic baths. For instance, quantum emitters interacting with a 2D square photonic bath (or reservoir) can exhibit directional emission into the lattice when they are properly tuned at a given frequency within the band [155], which corresponds to the stationary state reported in Fig. 5.4(d). A two-level atom weakly coupled to photonic lattices shows similar vacancy-like behavior to the one shown in Fig. 5.6(a) [156]. Indeed, it has been recently proved that the stationary states of driven-dissipative lattices are formally linked to that of the

quantum emitters coupled to lattices [157], opening up the possibility of exploring the quantum-emitter phenomena in a purely photonic platform.

# Chapter 6

# Chiral emission induced by optical Zeeman effect in micropillars

Up to here we have shown the qualities of exciton-polariton to implement lattice Hamiltonians with novel ingredients such as drive and dissipation. The studied phenomena has been purely linear and we have not dealt with the excitonic component of polaritons. As we have already mentioned, this matter component of polaritons provides them with sensitivity to magnetic fields as well as nonlinear interactions, which can be used in lattices to trigger more complex effects.

One of the major challenges when engineering photonic lattices is the implementation of Hamiltonians with broken time-reversal symmetry. This ingredient in the photonic toolbox allows the study of photonic Chern insulators and nonreciprocal structures. A natural way of breaking time-reversal symmetry is the application of an external magnetic field. For instance, the first demonstration of a Chern insulator for electromagnetic waves was realized in the microwave domain using a lattice made of a gyrotropic material subject to a magnetic field [45]. Later, emission from chiral edge modes was reported at telecom and near-infrared wavelengths in YIG photonic crystals [158, 159] and in lattices of coupled polariton micropillars [46], respectively. However, the relatively low magnetic susceptibility of these systems resulted in topological gaps of limited size. Moreover, a very interesting perspective would be the spatial control of the magnitude and direction of the magnetic field at the micron scale in such photonic lattices. This would allow the exploration of lattice Hamiltonians subject to, for instance, staggered magnetic fields.

Semiconductor microcavities are an excellent platform to overcome these challenges at near-infrared frequencies by taking advantage of the excitonic component of polaritons, which provides matter-like properties. For example, under an external

magnetic field, polaritons in GaAs-based micro-cavities show a Zeeman splitting inherited from the excitonic Zeeman splitting of GaAs quantum wells [160, 48, 161, 162]. Magnetic field have been also used to engineer gauge potentials [163] and induce spin currents [164]. The excitonic component results also in significant polariton-polariton interactions. They are dominated by excitonic exchange terms [49] giving rise to a strong polarization anisotropy [165]: polaritons of same circular polarization (i.e., spin) interact much stronger than polaritons of opposite polarizations [50, 166–168]. Interestingly, polarization-dependent interactions also take place between polariton modes and the reservoir of excitons excited under nonresonant pumping [169–171]. Therefore, by optically injecting spin-polarized carriers in the quantum wells, it is possible to create an interaction-induced Zeeman splitting, i.e., different blueshifts for polaritons of the same and opposite polarizations than the exciton gas. Recently, this effect has been reported in transition metal dichalcogenides [172]. As the exciton reservoir can be localized over a few microns scale [173], the interaction-induced Zeeman splitting could be engineered with onsite precision in a polariton lattice.

In this chapter we demonstrate the breaking of time-reversal symmetry for polaritons in a GaAs-based micropillar without the need of any external magnetic field. To do so we create an optical Zeeman splitting for polaritons by injecting a gas of spin-polarized excitons. Moreover, in combination with optical spin-orbit coupling inherent to semiconductor microstructures [174–176], the optically-induced Zeeman splitting results in emission of vortex beams with a well-defined chirality.

## 6.1 Polariton modes of a micropillar

For this experiment we use a semiconductor micropillar with a diameter of 2.8 $\mu$m [Fig. 6.1(a)]. It is etched from a $\lambda/2$ $Ga_{0.05}Al_{0.95}As$ microcavity ($\lambda = 780$ nm, $E_c = 1589.54$ meV) embedded between two DBRs of 40 and 28 pairs of $\lambda/4$ layers of $Ga_{0.05}Al_{0.95}As/Ga_{0.80}Al_{0.20}As$. Three set of four 7-nm GaAs QWs are grown inside the microcavity at three central maxima of the electromagnetic field. At the cryogenic temperature of the experiments (5 K), the exciton polaritons exhibit a Rabi splitting of 15 meV.

To probe the energy spectrum of the micropillar, we carry out photoluminescence experiments in reflection geometry using the setup schematized in Fig. 6.2. The sample hosting the micropillar is placed in a closed-cycle cryostat that allows reaching the temperature of 5 K. For the off-resonant pumping of the micropillar, we use a beam coming out from a continuous-wave monomode Ti:Sapph laser tuned at $\lambda = 744.4$ nm

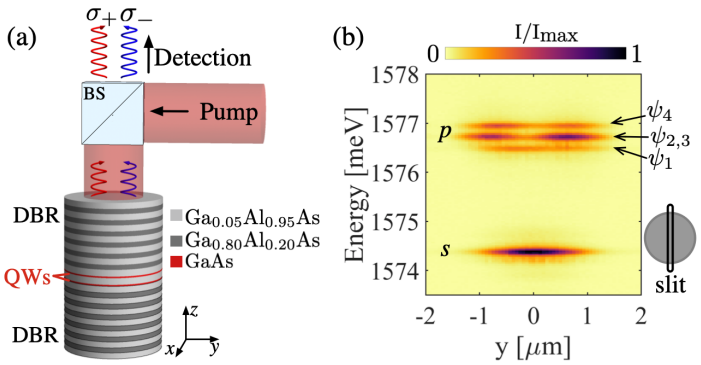


Fig. 6.1 **The micropillar and its spectrum**. (a) Sketch of the micropillar and the pumping-detection setup. (b) Photoluminescence spectrum of a 2.8-$\mu$m-diameter micropillar, showing $s$ and $p$ orbital modes. Gray disk depicts a top view of the micropillar and the unfilled vertical rectangle schematized the selected region by the slit.

($E = 1665.56$ meV). Before reaching the cryostat, the pumping beam is coupled into a polarization-maintaining monomode optical fiber, for spatial-mode cleaning purposes, and it then passes through a quarter-wave plate ($\lambda/4$) that sets its polarization (either linear or circular polarization). An aspherical lens with a 8-mm focal length (NA$= 0.5$) placed inside the cryostat ($f_1$ in Fig. 6.2) focuses tightly the pumping beam on the micropillar, which has full width half maximum (FWHM) on the sample is $2.5\,\mu$m. Once the pump reaches the micropillar, photons are absorbed and relaxation of carriers results in the formation of an exciton gas, which then populates the different polariton modes of the micropillar. After a dozen of picoseconds, polaritons decay and photons escape from the structure. This emission is collected by the same 8-mm focal lens ($f_1$) and then it is magnified and imaged at the entrance slit of a spectrometer (signal path shown in Fig. 6.2). The entrance slit together with a scanning lens placed on a motorized translation stage allow selecting real-space vertical slices of the micropillar emission. Each slice of the image is dispersed by the spectrometer and imaged on a coupled-charge device (CCD) camera, resolving the emission in energy with a resolution of 33.1 $\mu$eV.

Figure 6.1(b) displays the low-power photoluminescence spectrum measured along the vertical diameter of a micropillar with an exciton-photon detuning $\delta_{cx} = -7.8$ meV for the lowest energy mode (exciton fraction of 27%). The excitation beam is circularly polarized and the emission is detected in the same polarization. The two sets of energy levels displayed in the panel correspond to the fundamental and first-excited modes, called $s$ and $p$, respectively, owing to their symmetry. The eigenstates of the micropillar can be accurately described in a basis of Laguerre-Gauss modes in cylindrical

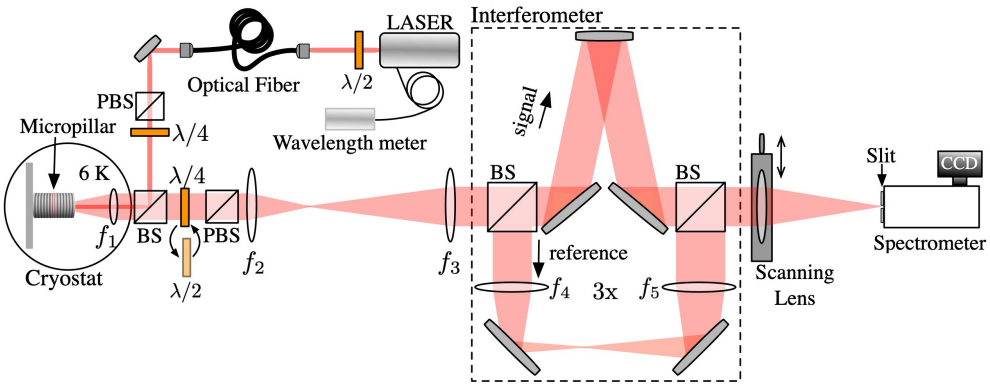


Fig. 6.2 Scheme of the experimental setup to measure both polarization-resolved and self-interfered polariton emission of the micropillar. The former is done by blocking the reference arm of the interferometer along the detection path, which is demarcated by the dashed rectangle. Lenses: $f_1 = 8$ mm, $f_2 = 300$ mm, $f_3 = 75$ mm, $f_4 = 100$ mm, $f_5 = 300$ mm. Abbreviations: $\lambda/2$ half-wave retarder, $\lambda/4$ quarter-wave retarder, PBS polarized beam splitter, BS beam splitter, CCD coupled-charge device.

coordinates $(r, \theta)$ and polarization pseudospin [176, 97, 177]: $\psi^{\sigma}_{nl} = C^{\sigma}_{n,l}(r)e^{il\theta}$, where $C_{n,l}(r)$ is the radial part of the Laguerre-Gauss modes. This basis is characterized by three quantum numbers: the radial quantum number $n$, which selects the $s$ or $p$ modes, the orbital angular momentum (OAM) $l$, and the circular polarization $\sigma_{\pm}$. The two $s$ modes present an OAM of $l = 0$ and are degenerate in polarization $(\sigma_{\pm})$ at $E_s = 1574.12$ meV.

The splitting of the triplet of $p$ modes visible in Figure 6.1(b) at around $E_p = 1576.74$ meV is a consequence of the optical spin-orbit coupling present in dielectric microcavities. Before describing in detail these orbital modes, we will focus on the $s$ modes of the micropillar in order to explore the consequences of inducing a spin imbalance in the exciton reservoir.

## 6.2 Optically induced Zeeman splitting

The micropillar exhibits two degenerate $s$ modes at energy $E_s$ with $\sigma_+$ and $\sigma_-$ polarizations. A splitting between them can be induced by taking advantage of polarization-dependent interactions present in polaritons [165, 50, 178, 179]. It has been shown that the exchange interaction of exciton with parallel spin is the predominant one for polariton-polariton interactions at negative exciton-photon detuning [50]. On the contrary, the exchange interaction between excitons (or polaritons) with antiparallel spin takes place by intermediate states of total spin momentum $s = \pm 2$, which are

optically inactive states (dark excitons) [50]. This event has a much less probability because the energy difference between initial and intermediate states is about the Rabi spliting: polaritons have the energy of the $s$ mode and dark excitons states are at the energy of the exciton. In samples with relatively low Rabi splitting ($\sim 3.5$ meV, for instance), interaction of excitons with opposite spin becomes relevant and they mainly happen via biexciton states, which can produce phenomena such as the Feshbach resonance [180].

To experimentally demonstrate this splitting, we perform power-dependent polarization-resolved photoluminescence measurements. Even though the pump is off resonant, the polarization of the generated carriers is partially preserved and an excitonic spin imbalance is created with a majority spin determined by the polarization of the laser [178]. At low pump power [0.26 kW cm$^{-2}$, Figs. 6.3(d) and 6.3(e)], interactions are negligible and the spin imbalance of the reservoir does not play any role: both $\sigma_+$ and $\sigma_-$ polariton modes emit at the same energy. At high pump powers, excitons with spin + interact mainly with $\sigma_+$ polaritons, while excitons with spin − interact with $\sigma_-$ polaritons [165]. As a consequence, when the pump irradiance is ramped up, polaritons co-polarized with the pump experience a higher energy blueshift than those cross-polarized. This is clearly evidenced in the spectral profiles displayed in Figs. 6.3(d) and 6.3(e). The peak energy of the $\sigma_+$ or $\sigma_-$ polarized polariton emission is shown in Figs. 6.3(a) and 6.3(b) as a function of excitation density for $\sigma_-$ and $\sigma_+$ polarized pumps, respectively. The shadowed areas represent the FWHM (linewidth) of the emission peak for each polarization, which is about 70 $\mu$eV at the lowest pump irradiance. When the power is increased, not only a splitting appears between opposite polarizations, but also the polariton mode co-polarized with the pump exhibits a higher intensity and becomes narrower in linewidth due to the onset of stimulated relaxation from the reservoir. Note that under a linearly polarized pump, the excitonic reservoir does not present any spin imbalance and both $\sigma_+$ and $\sigma_-$ polariton modes blueshift at the same rate when the pump power is increased [see Fig. 6.3(c)].

The measured energy difference between the two opposite polarizations under circularly polarized pumping is summarized in Fig. 6.3(f) and shows a behavior analogous to a Zeeman splitting in which the role of the external magnetic field is played by the power of the pump laser. The maximum observed splitting is $\sim 200\,\mu$eV at $P = 12.7$ kW cm$^{-2}$, which is of the same order than Zeeman splittings reported for exciton-polaritons with similar photon-exciton detuning, but under actual external magnetic fields of $4 - 9$ T in the Faraday configuration [160, 48, 161, 162]. Increasing further the pump power does not enlarge the splitting because co-polarized polaritons enter into the lasing

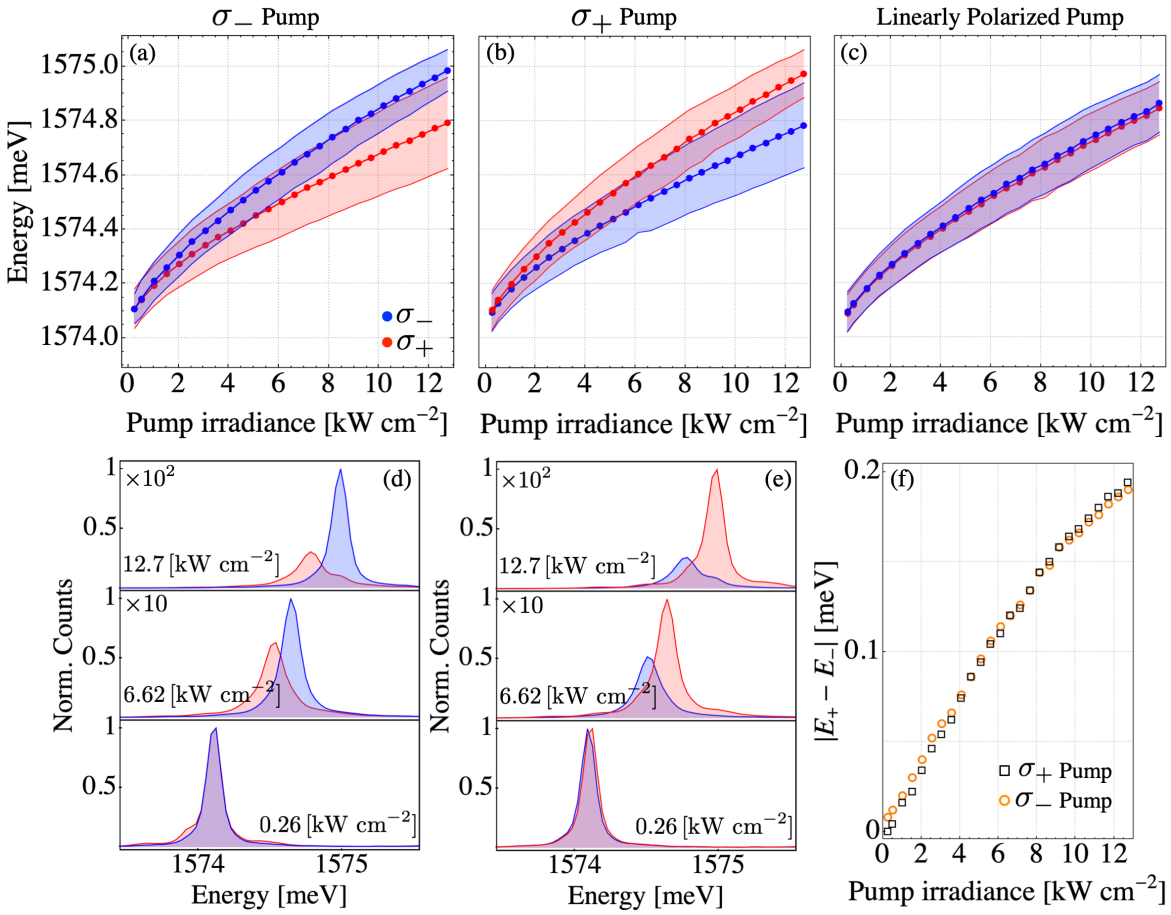


Fig. 6.3 **Optical Zeeman effect in a micropillar**. [(a)-(c)] Measured energy of $s$ orbitals as a function of the pump irradiance when detecting with circular polarization, $\sigma_-$ (blue dots) and $\sigma_+$ (red dots) with three different polarizations of the pump: (a) $\sigma_+$ circularly polarized, (b) $\sigma_-$ circularly polarized, (c) linearly polarized. Shadowed areas correspond to the measured FWHM of the emission peak. [(d),(e)] Measured spectra at three pump irradiance values when pumping with $\sigma_-$ and $\sigma_+$ polarization, respectively. (f) Absolute value of the splitting between $\sigma_+$ and $\sigma_-$ peak energies as a function of the pump irradiance.

regime causing a saturation of their blueshift. Other power-dependent spin-relaxation effects may also be at the origin of the saturation [181]. From the measured blueshift and splittings, and assuming that only excitons and polaritons of the same spin interact, we estimate the ratio of $\sigma_-$ to $\sigma_+$ exciton populations to be $n_+/n_- = 0.78$ at $P = 12.7$ kW cm$^{-2}$ under $\sigma_-$ pump.

## 6.3 Optical spin-orbit coupling in a micropillar

Now we turn our attention to the $p$ modes of the micropillar. As previously mentioned, these modes show three energy levels due to the presence of the optical spin-orbit coupling [see Fig. 6.1(b)]. In planar structures it manifests in the form of a linear polarization splitting between modes polarized along and perpendicular to the propagation direction within the cavity [69, 182, 183]. The splitting is a function of the in-plane momentum of the cavity photons and its magnitude depends on the spectral position of the cavity mode with respect to the center of the high reflectivity stop band of the structure [69]. This spectral position can be modified by using different values of $\lambda$ for the design of the Fabry-Perot mode of the $\lambda/2$ cavity and for the design of the $\lambda/4$ stacks in the mirrors. From the comparison between the measured value of the linear polarization splitting and transfer matrix simulations of the structure, we estimate the two values of $\lambda$ to differ by 3% in the present case.

In microstructured microcavities, the spin-orbit coupling gives rise to a fine structure of modes which mixes the orbital and polarization degrees of freedom. This was first reported in a hexagonal molecule of coupled micropillars in Refs. [175], whose $|l| = 1$ multiplet shows a triplet similar to the one observed in $\sigma_+$ ($\sigma_-$) column of Fig. 6.1(b). The exact same fine structure was found for $p$ modes in a single photonic dot open cavity by Dufferwiel and coworkers, who described the spin-orbit coupling effect in these modes with the following Hamiltonian [176]:

$$H_p = \begin{pmatrix} E_p & 0 & 0 & 0 \\ 0 & E_p & t_{\mathrm{SOC}} & 0 \\ 0 & t_{\mathrm{SOC}} & E_p & 0 \\ 0 & 0 & 0 & E_p \end{pmatrix}, \tag{6.1}$$

which is written in the basis $|l, \sigma\rangle$: $\{|+1, \sigma_+\rangle, |+1, \sigma_-\rangle, |-1, \sigma_+\rangle, |-1, \sigma_-\rangle\}$. $E_p$ is the energy of the $p$ modes in the absence of spin-orbit coupling, and $t_{\mathrm{SOC}}$ is the strength of the spin-orbit coupling. The four modes present the following eigenstate fine structure:

$$\begin{aligned} |\psi_1\rangle &= \frac{1}{\sqrt{2}} \left( |-1, \sigma_+\rangle - |+1, \sigma_-\rangle \right), \\ |\psi_2\rangle &= |+1, \sigma_+\rangle, \\ |\psi_3\rangle &= |-1, \sigma_-\rangle, \\ |\psi_4\rangle &= \frac{1}{\sqrt{2}} \left( |-1, \sigma_+\rangle + |+1, \sigma_-\rangle \right), \end{aligned} \tag{6.2}$$

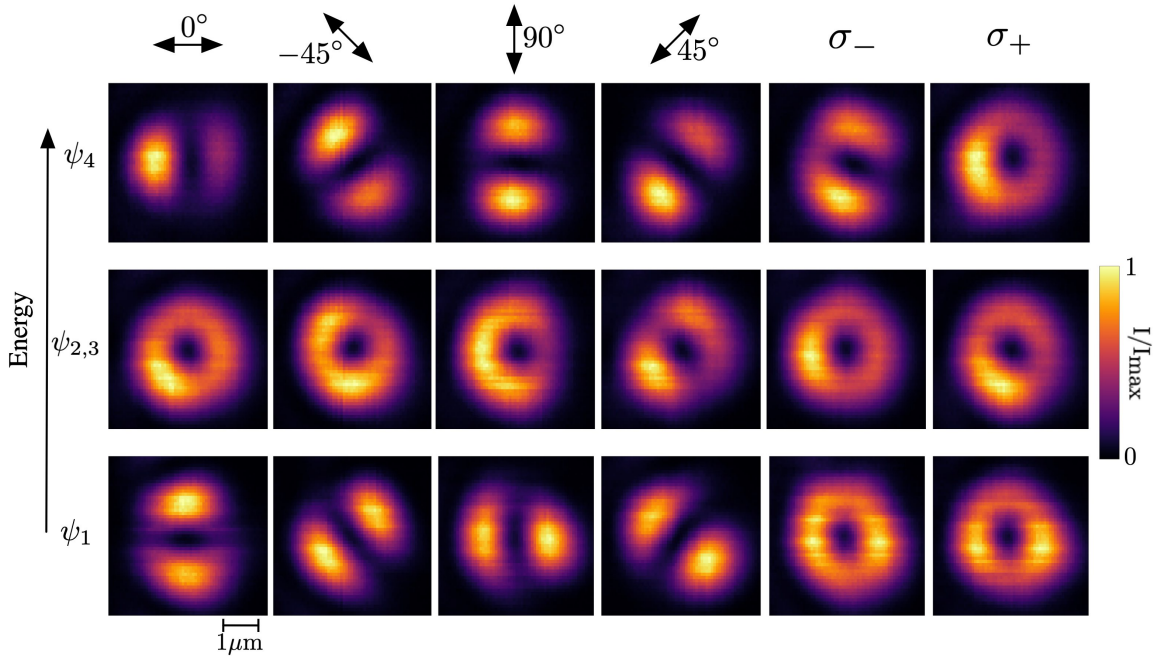


Fig. 6.4 **Real-space tomography of the *p* modes**. Bottom, middle and top rows present the real-space intensity profiles measured at the energies of the $\psi_1$, $\psi_{2,3}$ and $\psi_4$ modes, respectively, at low pump irradiance ($P = 0.26$ kW cm$^{-2}$) and with either linear or circular polarizations of detection (pointed out on the very top). Each image is normalized to its own maximum intensity.

with energy $E_1 = E_p - t_{\mathrm{SOC}}$, $E_2 = E_3 = E_p$ and $E_4 = E_p + t_{\mathrm{SOC}}$. This simple model explains the three $p$ emission lines visible in Fig. 6.1(b) at low excitation power, with $t_{\mathrm{SOC}} = 254 \pm 17\,\mu$eV.

The combination of orbital and polarization modes of the eigenstates results in different polarization textures for each $p$ mode. To extract them, polarization-resolved tomographies are implemented at low pump irradiance ($P = 0.26$ kW cm$^{-2}$). The four-left columns in Fig. 6.4 shows the reconstructed real-space profiles at the energy of the three emission lines of the $p$ modes when selecting linear polarization along horizontal (0°), vertical (90°), diagonal (45°), and antidiagonal (−45°) directions. A half-wave plate ($\lambda/2$) together with a polarized beam splitter (PBS) set the linear polarized detection, and the recording of many micropillar spectra at different horizontal position allows revealing the real-space profile of each mode. $\psi_1$ and $\psi_4$ modes display two intensity lobes that rotate in the opposite and the same sense as the selected polarization, respectively. In contrast, $\psi_{2,3}$ modes exhibit roughly a doughnut-like shape in every polarization with some changes in the intensity distribution. From these

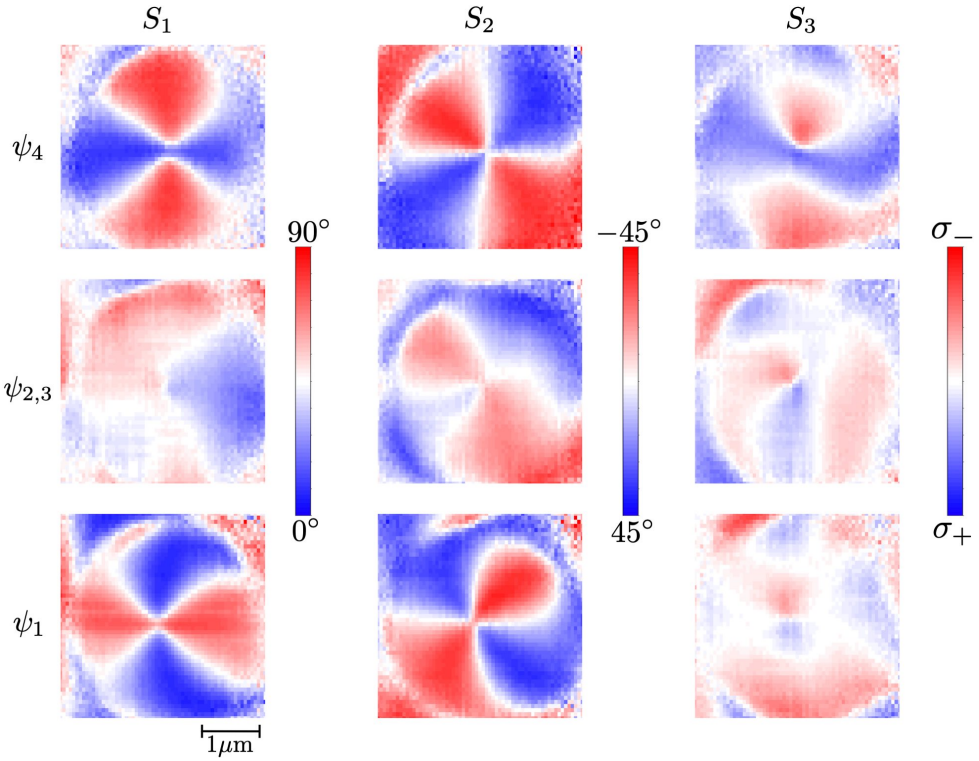


Fig. 6.5 **Stokes parameters**. $S_1$, $S_2$ and $S_3$ Stokes parameters [Eq. (6.3)] at the energy of the $p$ modes, computed from the images of Fig. 6.4.

images, the Stokes parameters for each pixel in real space are computed at the energy of the modes. These parameters are defined as

$$S_1 = \frac{I_{0^\circ} - I_{90^\circ}}{I_{0^\circ} + I_{90^\circ}}\,,\ S_2 = \frac{I_{45^\circ} - I_{-45^\circ}}{I_{45^\circ} + I_{-45^\circ}}\,,\ S_3 = \frac{I_{\sigma_+} - I_{\sigma_-}}{I_{\sigma_+} + I_{\sigma_-}}\,. \tag{6.3}$$

Figure 6.5 shows the Stokes parameters for the three emission energies of the $p$ modes. For $\psi_1$ and $\psi_4$, the $S_3$ Stokes parameter has very weak values (mostly light-blue and light-red colors), while $S_1$ and $S_2$ reach values close to 1 and $-1$ (dark red/blue, respectively). This means that these modes are well characterized by the linear polarization angle $\phi = (1/2)\arctan(S_2/S_1)$ [176], which define the polarization texture of the $p$ triplet.

Figure 6.6(b) shows the total intensity profile of each mode (sum of all polarizations, $I_{0^\circ} + I_{90^\circ}$). Lines on top indicate the orientation of the linear polarization at each point extracted from $S_1$ and $S_2$. The length of each line corresponds to the magnitude of the linear polarization angle. These two polarization textures, azimuthal and radial one for $\psi_1$ and $\psi_4$, respectively, were also reported in an open microcavity [176] and in a structure composed of six coupled micropillar forming a benzene-like molecule [175]. On

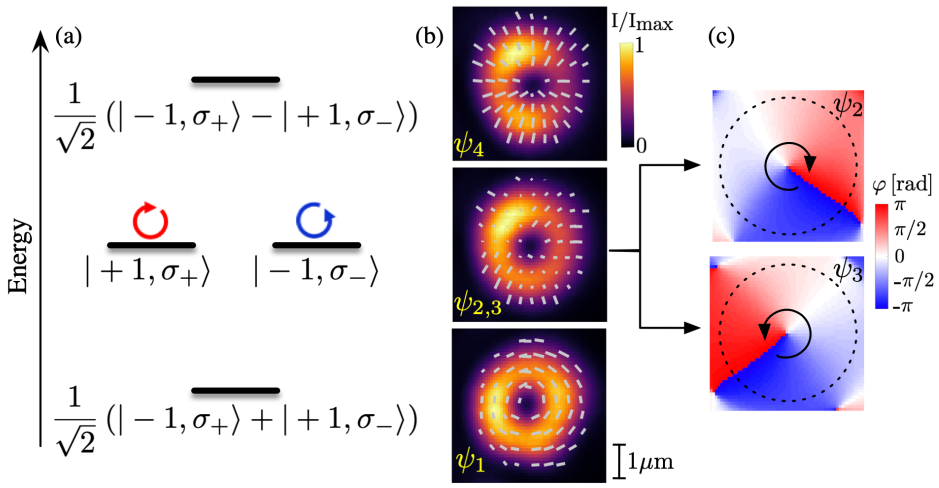


Fig. 6.6 ***p*-orbitals fine structure of the micropillar**.(a) Energy level of $p$ orbital modes of the micropillar in presence of the optical spin-orbit coupling, Eq. 6.2. (b) Real-space emission measured at low-pump irradiance (0.26 kW cm$^{-2}$) at the energy of the $\psi_{1,2,3,4}$ modes indicated in Fig.6.1(b). The bars show the measured orientation and degree of linear polarization at each point in space (polarization texture). (c) Retrieved phase at the energy of $\psi_2$ and $\psi_3$ modes when selecting $\sigma_+$ (top) and $\sigma_-$ (bottom) circular polarization of emission.

the other hand, the two middle states ($\psi_2$ and $\psi_3$), degenerate with energy $E_p$, present a phase vorticity of topological charge $\pm 1$ with circular polarization $\sigma_\pm$, respectively. The observed linear polarization pattern at the energy of these modes is determined by a phase relation between the two modes established by local disorder [176].

The presence of $l = \pm 1$ OAM coupled to $\sigma_\pm$ circular polarizations in states $\psi_2$ and $\psi_3$ can be evidenced by doing a polarization-resolved interferometric measurement. To do so, an interferometer is set up along the detection path (see region enclosed by a dashed rectangle in Fig. 6.2). The detection path is split into two path of the same length (zero delay time between the two arms). Along one of the arms, the image of the micropillar is magnified by a factor of 3 (reference beam) with respect to the image obtained along the other arm (signal beam). Consequently, the signal beam interfieres with a small area of the reference beam, which is used as a phase reference. This interference of the emission is then diffracted by the spectrometer and recorded by the CCD camera, which enables the reconstruction of an interference pattern at the energy of each mode. Figure 6.7(a) shows the reconstructed interference pattern for $|\psi_3\rangle$ mode ($\sigma_-$ polarized detection). To understand how the phase pattern of the signal beam can be extracted from the interference, let us write the two interfering beams in the following way:

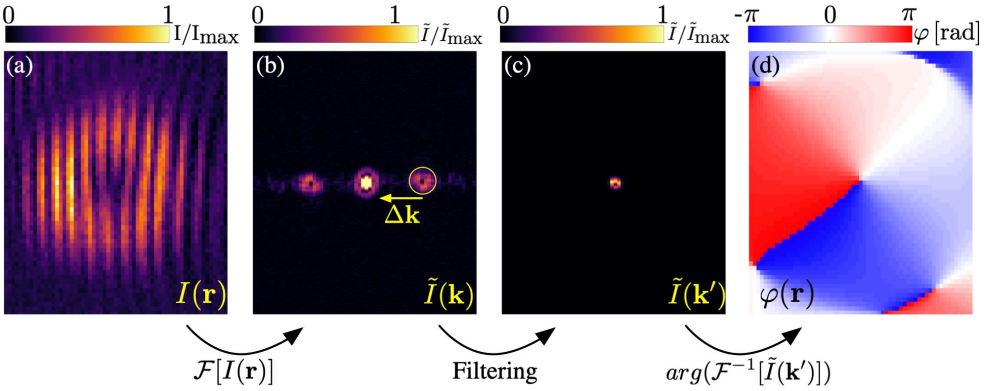


Fig. 6.7 **Retrieving of the wavefront phase**. (a) Interference pattern for the middle $p$ mode when selecting $\sigma_-$ polarization at low pump irradiance ($P = 0.26$ kW cm$^{-2}$). This is produced by interfering the signal and reference arm (see Fig. 6.2) with a given wavevector difference $\Delta\vec{k}$. (b) Fast Fourier transform (FFT) of the interferogram. (c) Filtered and translated image of (b). (d) Real-space phase pattern $\varphi(\vec{r})$ of the emission after Fourier transform of (c).

$$\begin{aligned} A_s(\vec{r},t) &= A_s(\vec{r})e^{-i(\omega t-\vec{k}_s\cdot\vec{r}+\varphi(\vec{r}))}\,, \\ A_r(\vec{r},t) &= A_r(\vec{r})e^{-i(\omega t-\vec{k}_r\cdot\vec{r})}\,, \end{aligned} \tag{6.4}$$

where $A_s(\vec{r})$ $[A_r(\vec{r})]$ is the amplitude of the signal [reference] beam, $\vec{r} = (x, y)$ is the real-space vector across the transverse plane of the micropillar (perpendicular to the growth direction $z$), $\omega$ is the frequency of the emitted mode (selected by the spectrometer), $\vec{k}_s$ and $\vec{k}_r$ are the transverse wavevectors of the signal and reference beam, respectively, and $\varphi(\vec{r})$ is the wavefront phase of the $p$ mode that varies throughout the $\vec{r}$ plane of the micropillar. Since the reference beam is three times bigger than the signal one, we assume the reference beam having a constant wavefront phase in the region of interference with the signal beam. Therefore, the interference can be written as:

$$\begin{aligned} I(\vec{r}) &= |A_s(\vec{r},t) + A_r(\vec{r},t)|^2\,, \\ I(\vec{r}) &= |A_s(\vec{r})|^2 + |A_r(\vec{r})|^2 + \left[A_s(\vec{r})A_r^*(\vec{r})e^{-i(\Delta\vec{k}\cdot\vec{r}+\varphi(\vec{r}))} + cc.\right]\,, \end{aligned} \tag{6.5}$$

where $\Delta\vec{k} = \vec{k}_s - \vec{k}_r$ is set by the angle between the signal and reference beams at the entrance slit of the spectrometer. The angle between the two beams lies within the horizontal plane, resulting in an interference fringes in the vertical direction. The

Fourier transform of this interference pattern, $\tilde{I}(\vec{k}) = \mathcal{F}[I(\vec{r})]$, gives three peaks that are shown in Fig. 6.7(b). One peak is at the center of the reciprocal space and it comes from the first and second terms of eq. (6.5). The other two peaks are translated by $\pm\Delta\vec{k}$ with respect to the origin and they come from the third and fourth terms of eq. (6.5). In consequence, these non-centered peaks carry the information of the wavefront phase $\varphi(\vec{r})$. In order to retrieve it, firstly, a translation equal to $-\Delta\vec{k}$ of the reciprocal space is done, thus, the right peak stays on the center of the reciprocal space. Secondly, a filtering process erases all other frequencies as shown in Fig. 6.7(c). Specifically, this filtering process selects the frequencies only within a small region in the center by using either a circular (sharp) or a gaussian-like shape, both filters giving similar results. The remaining peak corresponds to $\tilde{I}(\vec{k'}) = \mathcal{F}[A_s(\vec{r})A_r^*(\vec{r})e^{-i\varphi(\vec{r})}]$. Finally, an inverse Fourier transform of the filtered momentum space image is implemented. Its argument directly gives the phase $\varphi(\vec{r})$ shown in Fig. 6.7(d). The same procedure is done for the $|\psi_2\rangle$ mode ($\sigma_+$ polarized detection), which is shown in Fig. 6.5(b) along with the $|\psi_3\rangle$ mode. They display respectively a clear $2\pi$ and $-2\pi$ winding of the phase in the micropillar.

One of the most interesting features of this level structure [Fig. 6.6(a)] is that it can give rise to chiral modes with nonzero orbital-phase winding if a polarization splitting is induced between modes $\psi_2$ and $\psi_3$. Without inducing any splitting, Carlon Zambon and coworkers showed lasing in one of these degenerate modes in the weak-coupling regime using a hexagonal molecule of coupled micropillars [184]. In that paper, a spin imbalance in the exciton reservoir favored lasing gain in a mode with a given circular polarization and orbital angular momentum. Here we will show that a splitting between these levels can indeed be induced by taking advantage of polarization-dependent interactions. In this way time-reversal symmetry is broken without the need of any external magnetic field.

## 6.4 Chiral emission in $p$ modes

The optically induced Zeeman splitting we have described for the $s$ modes can be directly used to lift the degeneracy of middle modes in the $p$ multiplet, and to obtain the emission of modes with a net chirality. To experimentally demonstrate so, we now focus on power-dependent photoluminescence experiments in the $p$ modes. Taking advantage of the cavity wedge present in the wafer of the sample, we use a different micropillar of the same diameter as previous experiment with an emission energy for

the $p$ modes very close to that of the $s$ modes discussed in Fig. 6.1 and, therefore, with the same photon-exciton detuning.

Figure 6.8(b) displays the measured peak energy of each state extracted from a multi-gaussian fit as a function of the power irradiance of a $\sigma_-$ polarized pump when detecting either $\sigma_-$ or $\sigma_+$ polarizations. Every curve exhibits a monotonous blueshift of the energy when ramping up the power. More importantly, it is observed that modes $|\psi_3\rangle = |-1,\sigma_-\rangle$ and $|\psi_2\rangle = |+1,\sigma_+\rangle$ lift their degeneracy when the irradiance is increased. A maximum splitting $\Delta E_z = 94\,\mu$eV is observed at $P = 10.7$ kW cm$^{-2}$ [see Fig. 6.8(c)]. This is in contrast with the lower and uppermost modes corresponding, respectively, to $\psi_1$ and $\psi_4$, which present a negligible polarization splitting (within our spectral resolution), see Fig. 6.8(c).

The observed blueshifts and splittings in the $p$ manifold can be simulated using the hamiltonian in Eq. (6.1) with an extra Zeeman term $\Delta E_z$

$$H_p = \begin{pmatrix} E_p - \frac{\Delta E_z}{2} & 0 & 0 & 0 \\ 0 & E_p + \frac{\Delta E_z}{2} & t_{\mathrm{SOC}} & 0 \\ 0 & t_{\mathrm{SOC}} & E_p - \frac{\Delta E_z}{2} & 0 \\ 0 & 0 & 0 & E_p + \frac{\Delta E_z}{2} \end{pmatrix}. \tag{6.6}$$

We consider a saturable exciton reservoir with total density $n_{tot} = n_- + n_+ = \beta P/(1 + P/P_{sat})$, in which $P$ is the pump irradiance, $P_{sat}$ is the saturation value, and $\beta$ is a proportionality factor. Thus, the energy of the $p$ modes evolves as $E_p = E_p^0 + \alpha_1 n_{tot}/2$, where now $E_p^0 = 1574.58$ meV is the energy of the $p$ modes in absence of interactions and spin-orbit coupling, and $\alpha_1$ accounts for the interaction of excitons with same-spin polaritons (we neglect cross-spin interactions for the reasons mentioned in section 6.2). Additionally, we consider the Zeeman term as $\Delta E_z = \alpha_1(n_- - n_+)$, which takes into account the reservoir spin imbalance. Figure 6.8(a) shows the computed eigenenergies as a function of the pump irradiance $P$, considering $n_+/n_- = 0.86$, and $P_{sat}$ and $\alpha_1\beta$ as fitting parameters. The fit was done to match the measured energies for $\psi_2$ and $\psi_3$, resulting in an overall good agreement for the ensemble of the $p$ modes.

The direct consequence of the optically induced Zeeman splitting between states $\psi_2$ and $\psi_3$ is that orbital modes with opposite chirality are emitted at different energies. Therefore, frequency filtering of the emitted light is enough to select a mode with a given chirality. Figures 6.8(d1)-(e1) show the interference pattern measured in the energy-resolved tomographic experiment described above at the energy of the $\psi_2$ and $\psi_3$ modes, respectively, at an excitation density of $P = 10.7$ kW cm$^{-2}$. In this experiment, the total emitted intensity at a given energy is measured without

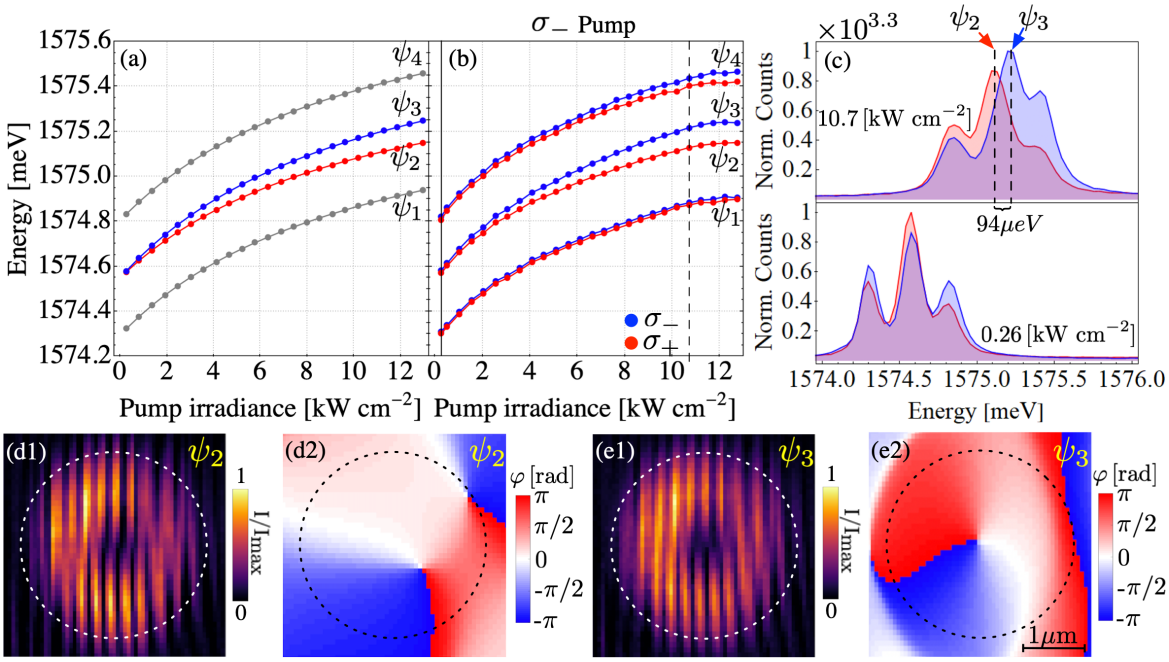


Fig. 6.8 **Chiral emission induced by optical Zeeman effect**. (a) Computed energy of $p$ orbitals from Hamiltonian (6.6) as a function of excitation density (see text for parameters). (b) Measured energy of the $p$ modes as a function of the pump irradiance when detecting with the two circular polarizations. Blue (red) dots correspond to $\sigma_-$ ($\sigma_+$) polarization of emission, and the pump is $\sigma_-$ polarized. (c) Measured photoluminescence spectra at two values of the pump irradiance, which are denoted by continuous and dashed lines in (b). The optical Zeeman splitting between the $\psi_2$ and $\psi_3$ modes is highlighted in the top panel. (d1),(e1) Measured interference patterns of middle $p$ modes at the energies of the $\psi_2$ and $\psi_3$ modes, respectively, without any polarization selection. The orbital angular momentum of the modes is evidenced in (d2) and (e2), which show the retrieved phase gradients [see Fig. 6.6(b) for comparison]

any polarization selection. From the interference patterns, the phase of the emitted field can be extracted by performing a filtered double Fourier transform, and it is shown in Fig. 6.8(d2) and (e2) (same procedure described above and summarized in Fig. 6.7). A phase singularity is observed close to the center of the micropillars, with a clockwise phase winding of $2\pi$ around the center for the emission energy of $\psi_2$ and a counterclockwise winding at energy of $\psi_3$. The phase singularity visible at the upper right edge of the micropillar in Fig. 6.8(d2) is an artifact related to a region of high gradient of intensity. Therefore, emission with energy-split vorticity is observed in our experiment thanks to the breaking of time-reversal symmetry optically induced by a polarized laser pump.

The value of the optical Zeeman splitting can be enlarged by increasing the excitonic component of the polaritons modes of interest. This can be done straightforwardly by changing the photon-exciton detuning. Concurrently, the photon component would decrease and with it the value of the spin-orbit coupling. In our experiments we chose the best available compromise in our structure to observe the splitting between the modes with opposite chirality. Increasing the spin-orbit coupling in further asymmetric microcavity structures would allow access to larger Zeeman splittings.

## 6.5 Conclusions

The method we have demonstrated to break time-reversal symmetry without the need of an external magnetic field has direct applications in the optical control of the topological phases of polariton Chern insulators in lattices [185, 186]. Indeed, the micropillar system we have discussed here is the building block to engineer one- and two-dimensional lattices. Moreover, the local control of the spin of the excitonic reservoir using external beams of different circular polarizations permits the breaking of time-reversal symmetry in more sophisticated manners. For example, one could envision lattices subject to staggered Zeeman fields, generating interfaces between two regions of a lattice illuminated with beams of opposite circular polarizations, which may show several topological edge modes.

# Chapter 7

# Conclusions and outlooks

In this thesis we have explored transport and localization properties of exciton polaritons in two-dimensional lattice potentials. The fabrication techniques developed in the laboratories of C2N have allowed us to study high-quality honeycomb lattices made of coupled semiconductor micropillars. Studies have been done by observing the photoluminescence of polariton systems. The precise control on the cavity wedge, micropillar width and inter-micropillar distances has enabled us to investigate tight-binding lattice Hamiltonians with impressive features.

Studying the polariton honeycomb lattices we have addressed Dirac physics present in graphene. We have taken as a landmark the preceding research of our group [12, 36, 99, 58]. We have simulated uniaxial compression in graphene via anisotropic inter-micropillar distances in the lattices, demonstrating experimentally a long-sought anisotropic transport of particles that happens due to the merging of the Dirac cones and the emergence of a semi-Dirac dispersion. Moreover, we have generated an all-optical analog of a bulk-vacancy state in graphene by harnessing the driving of polaritons, which has been reported in Ref. [101]. A promising perspectives is the study of nonlinear modes at the Dirac and semi-Dirac points in conservative lattices [187] and $\mathcal{PT}$-symmetric lattices [130], hardly studied so far due to the rarity of systems with engineered Dirac cones, loss and gain control, and nonlinearities.

Exploiting drive and dissipation in lattices of micropillar resonators, we have proposed novel types of localized modes. In general, we have shown that implementing multiple external optical drives in lattices of lossy resonators enlarges the possibility of manipulating interference effects in lattices and allows the appearance of localized modes down to a single lattice site. In particular, we have used a highly-photonic polariton honeycomb lattice resonantly driven by several laser beams at energies within its photonic bands to demonstrate this localization effect [188]. These localized modes

are analogous to the localized emission patterns expected from quantum emitters in photonic lattices [155, 156], as it was recently proposed [157]. Thus, ideas from this area could be studied in polariton platforms enlarging the possibilities of manipulating light-matter interaction.

Furthermore, we have inquired into the interaction between reservoir excitons and polaritons in a single micropillar structure. Performing power-dependent non-resonant experiments with circularly polarized laser beams, we have shown that time-reversal symmetry can be broken and an effective Zeeman splitting can be induced for the $s$ modes of a micropillar. Using this effect along with the inherent TE-TM splitting in our sample, we have proven the splitting of two opposite chiral states that are present in the $p$ orbitals of the micropillar, enabling the energy (or frequency) selection of these states [189]. This optical Zeeman effect can be implemented in lattices [190], which could permit the study of topological phases without the need of an external Zeeman field.

One can conceive more sophisticated lattices thanks to the capabilities of the fabrication process in C2N. For instance, lattices composed of micropillars with alternating width can be fabricated, giving way to the hopping between $s$ and $p$ orbitals and, thus, the implementation of negative hoppings. Preliminary studies in a Lieb lattice with $s$-$p$ hopping show that bands with dispersion along one direction only can be engineered. All the eigenstates are extended along one direction and localized in the orthogonal one, allowing unidirectional transport in the lattice. A natural next step is the study of this lattice in the nonlinear regime thanks to the sizable nonlinearity that the exciton component provides. The emergence of topological phases in the excitation spectrum of this lattice has been predicted [191].

On the other hand, the precise control of the optical drives presented in chapter 5 could open the way to the exploration of topological phases induced by nonlinearity. Specifically, an interesting avenue is the appearance of edge states in the excitation spectrum of a lattice by judiciously designing the resonant pumping beam [192].

# Appendix A

# Sample details

| | Desing 1 | $\delta z$ [nm] | n($\lambda_c = 780$ nm) | Rep |
|---|---|---|---|---|
| $\text{Layer}_1$ | $Ga_{0.80}Al_{0.20}As$ | 56.6 | 3.45 | 1 |
| $\text{DBR}_1$ | $Ga_{0.05}Al_{0.95}As$ | 65.0 | 2.99 | 27 |
| $\text{DBR}_2$ | $Ga_{0.80}Al_{0.20}As$ | 56.6 | 3.45 | 27 |
| $\text{Layer}_2$ | $Ga_{0.05}Al_{0.95}As$ | 65.0 | 2.99 | 1 |
| QWs | GaAs | 7.0 | 3.58 | 4 |
| $\text{Layer}_2$ | $Ga_{0.05}Al_{0.95}As$ | 3.0 | 2.99 | 4 |
| Sp | $Ga_{0.05}Al_{95}As$ | 39.6 | 2.99 | 1 |
| QWs | GaAs | 7.0 | 3.58 | 4 |
| $\text{Layer}_2$ | $Ga_{0.05}Al_{0.95}As$ | 3.0 | 2.99 | 4 |
| Sp | $Ga_{0.05}Al_{95}As$ | 36.6 | 2.99 | 1 |
| $\text{Layer}_1$ | $Ga_{0.80}Al_{0.20}As$ | 56.6 | 3.45 | 1 |
| $\text{Layer}_2$ | $Ga_{0.05}Al_{0.95}As$ | 65.0 | 2.99 | 4 |
| QWs | GaAs | 7.0 | 3.58 | 4 |
| $\text{Layer}_2$ | $Ga_{0.05}Al_{0.95}As$ | 65.0 | 2.99 | 1 |
| $\text{DBR}_2$ | $Ga_{0.80}Al_{0.20}As$ | 56.6 | 3.45 | 39 |
| $\text{DBR}_1$ | $Ga_{0.05}Al_{0.95}As$ | 65.0 | 2.99 | 39 |
| Sub | GaAs | $3.5 \cdot 10^5$ | 3.58 | 1 |

Table A.1 **Reflection sample parameters**. Nominal parameters used for the growth of the heterostructure. The target central cavity wavelength is $\lambda_c = 780$ nm. Abbreviations: $\text{DBR}_{1,2}$ distributed Bragg reflector or quarter-wave stacks, Sp spacer layer, QW quantum well, Sub substrate wafer. $\delta z$ indicates the thickness of the layers, $n$ correspond to the refractive index of the alloys calculated at $\lambda_c$ and Rep points out the number of repetitions of each layer.

| | Desing 2 | $\delta z$ [nm] | n($\lambda = 890$ nm) | Rep |
|---|---|---|---|---|
| $DBR_1$ | $Ga_{0.90}Al_{0.10}As$ | 64.76 | 3.44 | 28 |
| $DBR_2$ | $Ga_{0.05}Al_{0.95}As$ | 75.35 | 2.95 | 28 |
| Sp | GaAs | 116.93 | 3.51 | 1 |
| QW | $In_{0.09}Ga_{0.91}As$ | 20 | 3.51 | 1 |
| Sp | GaAs | 116.93 | 3.51 | 1 |
| $DBR_2$ | $Ga_{0.05}Al_{0.95}As$ | 75.35 | 2.95 | 32 |
| $DBR_1$ | $Ga_{0.90}Al_{0.10}As$ | 64.76 | 3.44 | 32 |
| Sub | GaAs | $3.5 \cdot 10^5$ | 3.51 | 1 |
| ARC | $SiO_{0.18}N_{1.22}$ | $\sim 112$ | 1.88 | 1 |

Table A.2 **Transmission sample parameters**. Nominal parameters used for the growth of the semiconductor microcavity. The target central cavity wavelength is $\lambda_c = 890$ nm. The Abbreviation are the same as in Table A.1 and ARC refers to the anti-reflective coating. Also, $\delta z$ indicates the thickness of the layers, $n$ correspond to the refractive index of the alloys calculated at $\lambda_c$ and Rep points out the number of repetitions of each layer.

# Appendix B

# Multiple-beams generation

The generation of multiple-beams excitation is made thanks to a reflective phase-only Spatial Light Modulator (SLM) PLUTO-2.1-NIR-015 (HR). This device is a liquid crystal on silicon (LCOS) microdisplay with a full HD resolution, $1920 \times 1080$ pixels, a $8\,\mu$m pixel pitch and an input frame rate of 60 Hz. This SLM is set up along the excitation path as schematized in Fig. B.1(a). Before the laser arrives to the SLM, it firstly passes through a single-mode polarization-maintaining optical fiber to be mode cleaned and collimated. Then, the beam is directed at normal incidence towards the SLM screen with the use of a beam splitter (BS). At this point, the SLM imprints the phase information of the desire real-space pattern to the beam. Then, the beam reflected by the SLM goes through the BS and it is directed towards the close-cycle cryostat where the sample is held at cryogenic temperature. A 8-nm lens inside the cryostat focus it on the sample generating the multiple-beams excitation, as schematized in Fig. B.1(b) for the case of exciting with three beams.

The basic operation of SLMs consists in changing the phase of a beam by addressing voltage signals to each pixel of the device. This voltage signal is encoded into 256 gray levels, which needs to be calibrated in order to know how much phase is added with each gray level. There are different methodologies to calibrate phase-only SLM and, in this thesis, we have used a method based on diffractive optics following the Ref. [193]. One of the advantage of diffractive methods compare to others, like ones based on interferometry measurements, is that this method is less sensitive to environmental fluctuations [193]. The method that we follow consists in measuring the focal irradiance of binary phase Fresnel lenses imprinted in the SLM screen as a function of the gray levels.

A binary phase Fresnel lens is an optical element composed of a set of radially symmetric rings with alternating phase values, which focus a beam at different focal

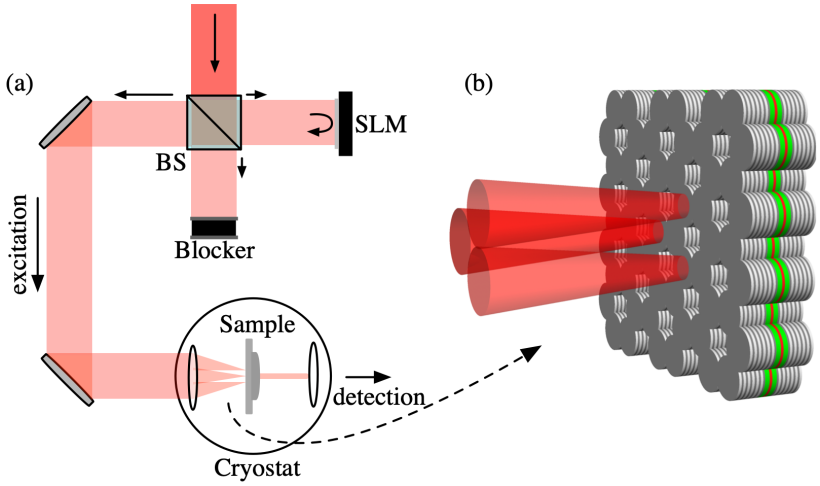


Fig. B.1 (a) Scheme of the experimental setup used to generate multiple laser beams. Abbreviations: SLM spatial light modulator, BS beam splitter. (b) Scheme of the excitation of the honeycomb lattice with three beams in order to obtain the localized mode in the surrounded resonator.

planes. For a given focal plane the beam intensity is determined by the phase difference among the alternating rings [193] as

$$I = \frac{4}{\pi^2} \sin^2 \left( \frac{\phi_2 - \phi_1}{2} \right) , \tag{B.1}$$

where $\phi_1$ and $\phi_2$ are the phases of the alternating rings. Since the phase modulation of the SLM is encoded into gray levels, a full characterization of the intensity can be done by varying one of the two gray levels and keeping the other at a given value. In order to do so, we use binary Fresnel lenses generated with the Pattern Generator software or the SLM Slideshow Player software, which is given by the Holoeye company, and we have controlled the gray levels with the same software. Specifically, once generated a binary Fresnel lens, one gray level is kept at value 0 while the other is varied from 0 to 255. The intensity in the central region of the beam is recorded by a CCD camera, which capture the light reflected by the SLM [the camera is placed right after the BS in the beam path reflected from the SLM, see Fig. B.1(a)]. Fig. B.2(a) shows the intensity as a function of the gray levels. As it is expected, the curve shows a sinusoidal shape. Replacing this values in Eq. (B.1) the phase shift as a function of the gray level is obtained, as shown in Fig. B.2(b).

The shaping of the laser in arbitrary input beams is done using a Matlab toolbox [194], which is composed of algorithms commonly used for generating patterns in beam shaping applications. In particular, we use the well-known iterative algorithm

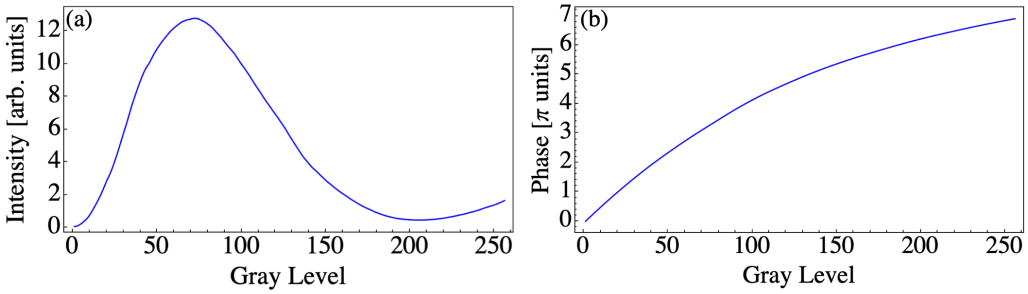


Fig. B.2 **Calibration of the SLM**(a) Intensity at the focal as a function of the Gray level for binary phase Fresnel lenses. (b) Phase shift as a function of the gray level obtained from Eq. (B.1) when replacing the values of the intensity obtained in (a).

called 2-D Gerchberg–Saxton that allow us to generate a far-field phase pattern of the target amplitude pattern. This method consists in 6 steps [194]: (1) Generate an initial guess of the phase pattern at the SLM, (2) Calculate the output amplitude profile by using the Fourier transform., (3) Multiply the output phase by the target amplitude, (4) perform the inverse Fourier transform, (5) Extract the phase of the generated complex amplitude, which is the new guess, and (6) Iterate until converged. In our case we create the multiple-beams target amplitude with the honeycomb geometry using a matlab code, which enters the iteration in step 3 and converges after 20 iterations.

# References


[1] D. N. Christodoulides, F. Lederer, and Y. Silberberg, Nature **424**, 817 (2003).

[2] L. Lu, J. D. Joannopoulos, and M. Soljačić, Nat. Photonics **8**, 821 (2014).

[3] A. B. Khanikaev and G. Shvets, Nat. Photonics **11**, 763 (2017).

[4] T. Ozawa, H. M. Price, A. Amo, N. Goldman, M. Hafezi, L. Lu, M. C. Rechtsman, D. Schuster, J. Simon, O. Zilberberg, and I. Carusotto, Rev. Mod. Phys. **91**, 015006 (2019).

[5] M. Kremer, L. J. Maczewsky, M. Heinrich, and A. Szameit, Opt. Mater. Express **11**, 1014 (2021).

[6] S. Xia, D. Song, N. Wang, X. Liu, J. Ma, L. Tang, H. Buljan, and Z. Chen, Opt. Mater. Express **11**, 1292 (2021).

[7] O. Zilberberg, Opt. Mater. Express **11**, 1143 (2021).

[8] J. Joannopoulos, S. Johnson, J. Winn, and R. Meade, *Photonic Crystals: Molding the Flow of Light - Second Edition* (Princeton University Press, 2011) pp. 1–24.

[9] M. Bellec, U. Kuhl, G. Montambaux, and F. Mortessagne, Phys. Rev. Lett. **110**, 033902 (2013).

[10] M. Hafezi, E. A. Demler, M. D. Lukin, and J. M. Taylor, Nat. Phys. **7**, 907 (2011).

[11] I. L. Garanovich, S. Longhi, A. A. Sukhorukov, and Y. S. Kivshar, Phys. Rep. **518**, 1 (2012).

[12] T. Jacqmin, I. Carusotto, I. Sagnes, M. Abbarchi, D. D. Solnyshkov, G. Malpuech, E. Galopin, A. Lemaître, J. Bloch, and A. Amo, Phys. Rev. Lett. **112**, 116402 (2014).

[13] T. Pertsch, P. Dannberg, W. Elflein, A. Bräuer, and F. Lederer, Phys. Rev. Lett. **83**, 4752 (1999).

[14] F. Dreisow, A. Szameit, M. Heinrich, T. Pertsch, S. Nolte, A. Tünnermann, and S. Longhi, Phys. Rev. Lett. **102**, 076802 (2009).

[15] H. Trompeter, W. Krolikowski, D. N. Neshev, A. S. Desyatnikov, A. A. Sukhorukov, Y. S. Kivshar, T. Pertsch, U. Peschel, and F. Lederer, Phys. Rev. Lett. **96**, 053903 (2006).

[16] Y. Sun, D. Leykam, S. Nenni, D. Song, H. Chen, Y. D. Chong, and Z. Chen, Phys. Rev. Lett. **121**, 033904 (2018).

[17] T. Schwartz, G. Bartal, S. Fishman, and M. Segev, Nature **446**, 52 (2007).

[18] Y. Lahini, A. Avidan, F. Pozzi, M. Sorel, R. Morandotti, D. N. Christodoulides, and Y. Silberberg, Phys. Rev. Lett. **100**, 013906 (2008).

[19] I. Makasyuk, Z. Chen, and J. Yang, Phys. Rev. Lett. **96**, 223903 (2006).

[20] F. Dreisow, M. Heinrich, A. Szameit, S. Döring, S. Nolte, A. Tünnermann, S. Fahr, and F. Lederer, Opt. Express **16**, 3474 (2008).

[21] H. S. Eisenberg, Y. Silberberg, R. Morandotti, A. R. Boyd, and J. S. Aitchison, Phys. Rev. Lett. **81**, 3383 (1998).

[22] J. W. Fleischer, T. Carmon, M. Segev, N. K. Efremidis, and D. N. Christodoulides, Phys. Rev. Lett. **90**, 023902 (2003).

[23] J. W. Fleischer, M. Segev, N. K. Efremidis, and D. N. Christodoulides, Nature **422**, 147 (2003).

[24] N. Masumoto, N. Y. Kim, T. Byrnes, K. Kusudo, A. Löffler, S. Höfling, A. Forchel, and Y. Yamamoto, New Journal of Physics **14**, 065002 (2012).

[25] R. A. Vicencio, C. Cantillano, L. Morales-Inostroza, B. Real, C. Mejía-Cortés, S. Weimann, A. Szameit, and M. I. Molina, Phys. Rev. Lett. **114**, 245503 (2015).

[26] S. Mukherjee, A. Spracklen, D. Choudhury, N. Goldman, P. Öhberg, E. Andersson, and R. R. Thomson, Phys. Rev. Lett. **114**, 245504 (2015).

[27] L. Morales-Inostroza and R. A. Vicencio, Phys. Rev. A **94**, 043831 (2016).

[28] S. A. Schulz, J. Upham, L. O'Faolain, and R. W. Boyd, Opt. Lett. **42**, 3243 (2017).

[29] S. Xia, A. Ramachandran, S. Xia, D. Li, X. Liu, L. Tang, Y. Hu, D. Song, J. Xu, D. Leykam, S. Flach, and Z. Chen, Phys. Rev. Lett. **121**, 263902 (2018).

[30] L. Tang, D. Song, S. Xia, S. Xia, J. Ma, W. Yan, Y. Hu, J. Xu, D. Leykam, and Z. Chen, Nanophotonics **9**, 1161 (2020).

[31] R. A. Vicencio, Advances in Physics: X **6**, 1878057 (2021).

[32] O. Peleg, G. Bartal, B. Freedman, O. Manela, M. Segev, and D. N. Christodoulides, Phys. Rev. Lett. **98**, 103901 (2007).

[33] M. C. Rechtsman, Y. Plotnik, J. M. Zeuner, D. Song, Z. Chen, A. Szameit, and M. Segev, Phys. Rev. Lett. **111**, 103901 (2013).

[34] Y. Plotnik, M. C. Rechtsman, D. Song, M. Heinrich, J. M. Zeuner, S. Nolte, Y. Lumer, N. Malkova, J. Xu, A. Szameit, Z. Chen, and M. Segev, Nat. Mater. **13**, 57 (2014).

[35] M. Bellec, U. Kuhl, G. Montambaux, and F. Mortessagne, New J. Phys. **16**, 113023 (2014).

[36] M. Milićević, T. Ozawa, P. Andreakou, I. Carusotto, T. Jacqmin, E. Galopin, A. Lemaître, L. Le Gratiet, I. Sagnes, J. Bloch, and A. Amo, 2D Mater. **2**, 034012 (2015).

[37] D. Song, V. Paltoglou, S. Liu, Y. Zhu, D. Gallardo, L. Tang, J. Xu, M. Ablowitz, N. K. Efremidis, and Z. Chen, Nat. Commun. **6**, 6272 (2015).

[38] M. C. Rechtsman, J. M. Zeuner, A. Tünnermann, S. Nolte, M. Segev, and A. Szameit, Nat. Photonics **7**, 153 (2013).

[39] O. Jamadi, E. Rozas, G. Salerno, M. Milićević, T. Ozawa, I. Sagnes, A. Lemaître, L. Le Gratiet, A. Harouri, I. Carusotto, J. Bloch, and A. Amo, Light Sci. Appl. **9**, 144 (2020).

[40] M. Bellec, C. Poli, U. Kuhl, F. Mortessagne, and H. Schomerus, Light Sci. Appl. **9**, 146 (2020).

[41] C. E. Whittaker, T. Dowling, A. V. Nalitov, A. V. Yulin, B. Royall, E. Clarke, M. S. Skolnick, I. A. Shelykh, and D. N. Krizhanovskii, Nat. Photonics **15**, 193 (2021).

[42] N. Malkova, I. Hromada, X. Wang, G. Bryant, and Z. Chen, Opt. Lett. **34**, 1633 (2009).

[43] M. C. Rechtsman, J. M. Zeuner, Y. Plotnik, Y. Lumer, D. Podolsky, F. Dreisow, S. Nolte, M. Segev, and A. Szameit, Nature **496**, 196 (2013).

[44] M. Hafezi, S. Mittal, J. Fan, A. Migdall, and J. M. Taylor, Nat. Photonics **7**, 1001 (2013).

[45] Z. Wang, Y. Chong, J. D. Joannopoulos, and M. Soljačić, Nature **461**, 772 (2009).

[46] S. Klembt, T. H. Harder, O. A. Egorov, K. Winkler, R. Ge, M. A. Bandres, M. Emmerling, L. Worschech, T. C. H. Liew, M. Segev, C. Schneider, and S. Höfling, Nature **562**, 552 (2018).

[47] C. Weisbuch, M. Nishioka, A. Ishikawa, and Y. Arakawa, Phys. Rev. Lett. **69**, 3314 (1992).

[48] P. Walker, T. C. H. Liew, D. Sarkar, M. Durska, A. P. D. Love, M. S. Skolnick, J. S. Roberts, I. A. Shelykh, A. V. Kavokin, and D. N. Krizhanovskii, Phys. Rev. Lett. **106**, 257401 (2011).

[49] C. Ciuti, V. Savona, C. Piermarocchi, A. Quattropani, and P. Schwendimann, Phys. Rev. B **58**, 7926 (1998).

[50] M. Vladimirova, S. Cronenberger, D. Scalbert, K. V. Kavokin, A. Miard, A. Lemaître, J. Bloch, D. Solnyshkov, G. Malpuech, and A. V. Kavokin, Phys. Rev. B **82**, 075301 (2010).

## References


[51] A. Amo and J. Bloch, Comptes Rendus Phys. **17**, 934 (2016).

[52] S. Klembt, T. H. Harder, O. A. Egorov, K. Winkler, H. Suchomel, J. Beierlein, M. Emmerling, C. Schneider, and S. Höfling, Applied Physics Letters **111**, 231102 (2017).

[53] C. E. Whittaker, E. Cancellieri, P. M. Walker, D. R. Gulevich, H. Schomerus, D. Vaitiekus, B. Royall, D. M. Whittaker, E. Clarke, I. V. Iorsh, I. A. Shelykh, M. S. Skolnick, and D. N. Krizhanovskii, Phys. Rev. Lett. **120**, 097401 (2018).

[54] D. D. Solnyshkov, G. Malpuech, P. St-Jean, S. Ravets, J. Bloch, and A. Amo, Opt. Mater. Express **11**, 1119 (2021), 2011.03012 .

[55] T. Gao, G. Li, E. Estrecho, T. C. H. Liew, D. Comber-Todd, A. Nalitov, M. Steger, K. West, L. Pfeiffer, D. W. Snoke, A. V. Kavokin, A. G. Truscott, and E. A. Ostrovskaya, Phys. Rev. Lett. **120**, 065301 (2018).

[56] R. Su, E. Estrecho, D. Biegańska, Y. Huang, M. Wurdack, M. Pieczarka, A. G. Truscott, T. C. H. Liew, E. A. Ostrovskaya, and Q. Xiong, Science Advances **7**, eabj8905 (2021).

[57] P. St-Jean, V. Goblot, E. Galopin, A. Lemaître, T. Ozawa, L. Le Gratiet, I. Sagnes, J. Bloch, and A. Amo, Nat. Photonics **11**, 651 (2017).

[58] M. Milićević, O. Bleu, D. Solnyshkov, I. Sagnes, A. Lemaître, L. Le Gratiet, A. Harouri, J. Bloch, G. Malpuech, and A. Amo, SciPost Phys. **5**, 064 (2018).

[59] J. Kasprzak, M. Richard, S. Kundermann, A. Baas, P. Jeambrun, J. M. Keeling, F. M. Marchetti, M. H. Szymánska, R. André, J. L. Staehli, V. Savona, P. B. Littlewood, B. Deveaud, and L. S. Dang, Nature **443**, 409 (2006).

[60] D. Tanese, H. Flayac, D. Solnyshkov, A. Amo, A. Lemaître, E. Galopin, R. Braive, P. Senellart, I. Sagnes, G. Malpuech, and J. Bloch, Nat. Commun. **4**, 1749 (2013).

[61] F. Baboux, D. De Bernardis, V. Goblot, V. N. Gladilin, C. Gomez, E. Galopin, L. Le Gratiet, A. Lemaître, I. Sagnes, I. Carusotto, M. Wouters, A. Amo, and J. Bloch, Optica **5**, 1163 (2018).

[62] S. R. K. Rodriguez, A. Amo, I. Sagnes, L. Le Gratiet, E. Galopin, A. Lemaître, and J. Bloch, Nat. Commun. **7**, 11887 (2016).

[63] S. Rahimzadeh Kalaleh Rodriguez, A. Amo, I. Carusotto, I. Sagnes, L. Le Gratiet, E. Galopin, A. Lemaitre, and J. Bloch, ACS Photonics **5**, 95 (2018).

[64] V. Goblot, B. Rauer, F. Vicentini, A. Le Boité, E. Galopin, A. Lemaître, L. Le Gratiet, A. Harouri, I. Sagnes, S. Ravets, C. Ciuti, A. Amo, and J. Bloch, Phys. Rev. Lett. **123**, 113901 (2019).

[65] P. Yeh, *Optical Waves in Layered Media*, Wiley Series in Pure and Applied Optics (Wiley, 2005).

[66] A. Kavokin, J. Baumberg, G. Malpuech, and F. Laussy, *Microcavities*, Series on Semiconductor Science and Technology (OUP Oxford, 2017) pp. 133–140, 244.

[67] V. Savona, in *Confined Photon Systems*, edited by H. Benisty, C. Weisbuch, É. Polytechnique, J.-M. Gérard, R. Houdré, and J. Rarity (Springer Berlin Heidelberg, Berlin, Heidelberg, 1999) pp. 173–242.

[68] N. Carlon Zambon, *Chirality and nonlinear dynamics in polariton microresonators*, Ph.D. thesis, Université Paris-Saclay (2020).

[69] G. Panzarini, L. C. Andreani, A. Armitage, D. Baxter, M. S. Skolnick, V. N. Astratov, J. S. Roberts, A. V. Kavokin, M. R. Vladimirova, and M. A. Kaliteevski, Phys. Rev. B **59**, 5082 (1999).

[70] S. M. Girvin and K. Yang, *Modern Condensed Matter Physics* (Cambridge University Press, 2019) pp. 198–210.

[71] R. L. Greene, K. K. Bajaj, and D. E. Phelps, Phys. Rev. B **29**, 1807 (1984).

[72] G. H. Wannier, Phys. Rev. **52**, 191 (1937).

[73] N. F. Mott, Trans. Faraday Soc. **34**, 500 (1938).

[74] A. Rahimi-Iman, *Polariton physics*, Springer Series in Optical Sciences (Springer, Cham, 2020) pp. 37–44, 60.

[75] B. Deveaud, F. Clérot, N. Roy, K. Satzke, B. Sermage, and D. S. Katzer, Phys. Rev. Lett. **67**, 2355 (1991).

[76] E. M. Purcell, H. C. Torrey, and R. V. Pound, Phys. Rev. **69**, 37 (1946).

[77] J. J. Hopfield, Phys. Rev. **112**, 1555 (1958).

[78] I. Carusotto and C. Ciuti, Rev. Mod. Phys. **85**, 299 (2013).

[79] D. Porras, C. Ciuti, J. J. Baumberg, and C. Tejedor, Phys. Rev. B **66**, 085304 (2002).

[80] M. Wouters and I. Carusotto, Phys. Rev. Lett. **99**, 140402 (2007).

[81] P. M. Walker, L. Tinkler, B. Royall, D. V. Skryabin, I. Farrer, D. A. Ritchie, M. S. Skolnick, and D. N. Krizhanovskii, Phys. Rev. Lett. **119**, 097403 (2017).

[82] P. Stepanov, I. Amelio, J. G. Rousset, J. Bloch, A. Lemaître, A. Amo, A. Minguzzi, I. Carusotto, and M. Richard, Nat. Commun **10**, 3869 (2019).

[83] B. Deveaud, Comptes Rendus Physique **17**, 874 (2016), polariton physics / Physique des polaritons.

[84] C. Schneider, K. Winkler, M. D. Fraser, M. Kamp, Y. Yamamoto, E. A. Ostrovskaya, and S. Höfling, Reports Prog. Phys. **80**, 016503 (2017), 1510.07540 .

[85] E. A. Cerda-Méndez, D. N. Krizhanovskii, M. Wouters, R. Bradley, K. Biermann, K. Guda, R. Hey, P. V. Santos, D. Sarkar, and M. S. Skolnick, Phys. Rev. Lett. **105**, 116402 (2010).

[86] E. A. Cerda-Méndez, D. Sarkar, D. N. Krizhanovskii, S. S. Gavrilov, K. Biermann, M. S. Skolnick, and P. V. Santos, Phys. Rev. Lett. **111**, 146401 (2013).

[87] E. A. Cerda-Méndez, D. N. Krizhanovskii, M. S. Skolnick, and P. V. Santos, J. Phys. D Appl. Phys. **51**, 033001 (2018).

[88] E. Wertz, L. Ferrier, D. D. Solnyshkov, R. Johne, D. Sanvitto, A. Lemaître, I. Sagnes, R. Grousson, A. V. Kavokin, P. Senellart, G. Malpuech, and J. Bloch, Nat. Phys. **6**, 860 (2010).

[89] A. Askitopoulos, H. Ohadi, A. V. Kavokin, Z. Hatzopoulos, P. G. Savvidis, and P. G. Lagoudakis, Phys. Rev. B **88**, 041308 (2013).

[90] N. G. Berloff, M. Silva, K. Kalinin, A. Askitopoulos, J. D. Töpfer, P. Cilibrizzi, W. Langbein, and P. G. Lagoudakis, Nat. Mater. **16**, 1120 (2017).

[91] S. Alyatkin, H. Sigurdsson, A. Askitopoulos, J. D. Töpfer, and P. G. Lagoudakis, Nat. Commun. **12**, 5571 (2021).

[92] C. W. Lai, N. Y. Kim, S. Utsunomiya, G. Roumpos, H. Deng, M. D. Fraser, T. Byrnes, P. Recher, N. Kumada, T. Fujisawa, and Y. Yamamoto, Nature **450**, 529 (2007).

[93] N. Y. Kim, K. Kusudo, C. Wu, N. Masumoto, A. Löffler, S. Höfling, N. Kumada, L. Worschech, A. Forchel, and Y. Yamamoto, Nat. Phys **7**, 681 (2011).

[94] R. I. Kaitouni, O. El Daïf, A. Baas, M. Richard, T. Paraiso, P. Lugan, T. Guillet, F. Morier-Genoud, J. D. Ganière, J. L. Staehli, V. Savona, and B. Deveaud, Phys. Rev. B **74**, 155311 (2006).

[95] K. Winkler, J. Fischer, A. Schade, M. Amthor, R. Dall, J. Geßler, M. Emmerling, E. A. Ostrovskaya, M. Kamp, C. Schneider, and S. Höfling, New Journal of Physics **17**, 023001 (2015).

[96] J. Bloch, R. Planel, V. Thierry-Mieg, J. Gérard, D. Barrier, J. Marzin, and E. Costard, Superlattices and Microstruct **22**, 371 (1997).

[97] J. M. Gérard, D. Barrier, J. Y. Marzin, R. Kuszelewicz, L. Manin, E. Costard, V. Thierry-Mieg, and T. Rivera, Applied Physics Letters **69**, 449 (1996).

[98] M. Galbiati, L. Ferrier, D. D. Solnyshkov, D. Tanese, E. Wertz, A. Amo, M. Abbarchi, P. Senellart, I. Sagnes, A. Lemaître, E. Galopin, G. Malpuech, and J. Bloch, Phys. Rev. Lett. **108**, 126403 (2012).

[99] M. Milićević, T. Ozawa, G. Montambaux, I. Carusotto, E. Galopin, A. Lemaître, L. Le Gratiet, I. Sagnes, J. Bloch, and A. Amo, Phys. Rev. Lett. **118**, 107403 (2017).

[100] M. Milićević, G. Montambaux, T. Ozawa, O. Jamadi, B. Real, I. Sagnes, A. Lemaître, L. Le Gratiet, A. Harouri, J. Bloch, and A. Amo, Phys. Rev. X **9**, 031010 (2019).

[101] B. Real, O. Jamadi, M. Milićević, N. Pernet, P. St-Jean, T. Ozawa, G. Montambaux, I. Sagnes, A. Lemaître, L. Le Gratiet, A. Harouri, S. Ravets, J. Bloch, and A. Amo, Phys. Rev. Lett. **125**, 186601 (2020), 2004.03478 .

[102] C. Kittel, *Introduction to Solid State Physics, 8th Edition* (John Willey and Sons, Inc., 2004).

[103] E. Kaxiras, *Atomic and Electronic Structure of Solids* (Cambridge University Press, 2003).

[104] F. Mangussi, M. Milićević, I. Sagnes, L. L. Gratiet, A. Harouri, A. Lemaître, J. Bloch, A. Amo, and G. Usaj, J. Phys. Condens **32**, 315402 (2020), 1907.13621 .

[105] P. R. Wallace, Phys. Rev. **71**, 622 (1947).

[106] A. K. Geim and K. S. Novoselov, Nat. Mater. **6**, 183 (2007).

[107] K. S. Novoselov, A. K. Geim, S. V. Morozov, D. Jiang, M. I. Katsnelson, I. V. Grigorieva, S. V. Dubonos, and A. A. Firsov, Nature **438**, 197 (2005).

[108] A. H. Castro Neto, F. Guinea, N. M. R. Peres, K. S. Novoselov, and A. K. Geim, Rev. Mod. Phys. **81**, 109 (2009).

[109] K. Watanabe, T. Taniguchi, and H. Kanda, Nat. Mater. **3**, 404 (2004).

[110] C.-H. Park, L. Yang, Y.-W. Son, M. L. Cohen, and S. G. Louie, Nat. Phys. **4**, 213 (2008).

[111] M. O. Goerbig, J. N. Fuchs, G. Montambaux, and F. Piéchon, Phys. Rev. B **78**, 045415 (2008), arXiv:0803.0912 .

[112] B. Wunsch, F. Guinea, and F. Sols, New J. Phys. **10**, 103027 (2008).

[113] P. Dietl, F. Piéchon, and G. Montambaux, Phys. Rev. Lett. **100**, 236405 (2008).

[114] V. M. Pereira, A. H. Castro Neto, and N. M. R. Peres, Phys. Rev. B **80**, 045401 (2009).

[115] G. Montambaux, F. Piéchon, J.-N. Fuchs, and M. O. Goerbig, Phys. Rev. B **80**, 153412 (2009).

[116] G. Montambaux, F. Piéchon, J.-N. Fuchs, and M. O. Goerbig, Eur. Phys. J. B **72**, 509 (2009).

[117] R. de Gail, J.-N. Fuchs, M. Goerbig, F. Piéchon, and G. Montambaux, Physica B **407**, 1948 (2012).

[118] J. Ibañez-Azpiroz, A. Eiguren, A. Bergara, G. Pettini, and M. Modugno, Phys. Rev. A **88**, 033631 (2013).

[119] J. Feilhauer, W. Apel, and L. Schweitzer, Phys. Rev. B **92**, 245424 (2015).

[120] G. E. Volovik and K. Zhang, JETP Lett. **104**, 645 (2016).

[121] V. H. Nguyen and J.-C. Charlier, Phys. Rev. B **97**, 235113 (2018).

[122] D. Li, B. Rosenstein, B. Y. Shapiro, and I. Shapiro, Phys. Rev. B **95**, 094513 (2017).

[123] Y. Hasegawa, R. Konno, H. Nakano, and M. Kohmoto, Phys. Rev. B **74**, 33413 (2006).

[124] S.-L. Zhu, B. Wang, and L.-M. Duan, Phys. Rev. Lett. **98**, 260402 (2007).

[125] C. Dutreix, L. Bilteanu, A. Jagannathan, and C. Bena, Phys. Rev. B **87**, 245413 (2013).

[126] L.-K. Lim, J.-N. Fuchs, and G. Montambaux, Phys. Rev. Lett. **108**, 175303 (2012).

[127] P. Adroguer, D. Carpentier, G. Montambaux, and E. Orignac, Phys. Rev. B **93**, 125113 (2016).

[128] J. Kim, S. S. Baik, S. H. Ryu, Y. Sohn, S. Park, B.-G. Park, J. Denlinger, Y. Yi, H. J. Choi, and K. S. Kim, Science **349**, 723 (2015).

[129] L. Tarruell, D. Greif, T. Uehlinger, G. Jotzu, and T. Esslinger, Nature **483**, 302 (2012).

[130] M. Kremer, T. Biesenthal, L. J. Maczewsky, M. Heinrich, R. Thomale, and A. Szameit, Nat. Commun. **10**, 435 (2019).

[131] K. Nakada, M. Fujita, G. Dresselhaus, and M. S. Dresselhaus, Phys. Rev. B **54**, 17954 (1996).

[132] M. Fujita, K. Wakabayashi, K. Nakada, and K. Kusakabe, J. Phys. Soc. Jpn **65**, 1920 (1996).

[133] M. Kohmoto and Y. Hasegawa, Phys. Rev. B **76**, 205402 (2007), 0702162 .

[134] S. Ryu and Y. Hatsugai, Phys. Rev. Lett. **89**, 077002 (2002), 0112197 .

[135] Y. Hatsugai, T. Fukui, and H. Aoki, Eur. Phys. J. Spec. Top. **148**, 133 (2007).

[136] P. Delplace, D. Ullmo, and G. Montambaux, Phys. Rev. B **84**, 195452 (2011), 1109.4608 .

[137] Y. Kobayashi, K.-i. Fukui, T. Enoki, K. Kusakabe, and Y. Kaburagi, Phys. Rev. B **71**, 193406 (2005), 0503472 [cond-mat] .

[138] P. St-Jean, A. Dauphin, P. Massignan, B. Real, O. Jamadi, M. Milicevic, A. Lemaître, A. Harouri, L. Le Gratiet, I. Sagnes, S. Ravets, J. Bloch, and A. Amo, Phys. Rev. Lett. **126**, 127403 (2021).

[139] V. M. Pereira, F. Guinea, J. M. B. Lopes dos Santos, N. M. R. Peres, and A. H. Castro Neto, Phys. Rev. Lett. **96**, 036801 (2006).

[140] T. O. Wehling, A. V. Balatsky, M. I. Katsnelson, A. I. Lichtenstein, K. Scharnberg, and R. Wiesendanger, Phys. Rev. B **75**, 125425 (2007).

[141] L. Levi, M. Rechtsman, B. Freedman, T. Schwartz, O. Manela, and M. Segev, Science **332**, 1541 (2011).

[142] D. Leykam, A. Andreanov, and S. Flach, Advances in Physics: X **3**, 1473052 (2018).

[143] Y. Plotnik, O. Peleg, F. Dreisow, M. Heinrich, S. Nolte, A. Szameit, and M. Segev, Phys. Rev. Lett. **107**, 183901 (2011).

[144] C. W. Hsu, B. Zhen, A. D. Stone, J. D. Joannopoulos, and M. Soljačić, Nat. Rev. Mater **1**, 16048 (2016).

[145] A. Regensburger, M.-A. Miri, C. Bersch, J. Näger, G. Onishchukov, D. N. Christodoulides, and U. Peschel, Phys. Rev. Lett. **110**, 223902 (2013).

[146] H. Ohno, E. E. Mendez, J. A. Brum, J. M. Hong, F. Agulló-Rueda, L. L. Chang, and L. Esaki, Phys. Rev. Lett. **64**, 2555 (1990).

[147] N. Malkova, I. Hromada, X. Wang, G. Bryant, and Z. Chen, Phys. Rev. A **80**, 043806 (2009).

[148] C. Symonds, A. Lemaître, E. Homeyer, J. C. Plenet, and J. Bellessa, Appl. Phys. Lett **95**, 151114 (2009).

[149] C. Poli, M. Bellec, U. Kuhl, F. Mortessagne, and H. Schomerus, Nat. Commun. **6**, 6710 (2015).

[150] J. Noh, W. A. Benalcazar, S. Huang, M. J. Collins, K. P. Chen, T. L. Hughes, and M. C. Rechtsman, Nat. Photonics **12**, 408 (2018).

[151] Y. Ota, F. Liu, R. Katsumi, K. Watanabe, K. Wakabayashi, Y. Arakawa, and S. Iwamoto, Optica **6**, 786 (2019).

[152] S. Mittal, V. V. Orre, G. Zhu, M. A. Gorlach, A. Poddubny, and M. Hafezi, Nat. Photonics **13**, 692 (2019).

[153] S. Weimann, Y. Xu, R. Keil, A. E. Miroshnichenko, A. Tünnermann, S. Nolte, A. A. Sukhorukov, A. Szameit, and Y. S. Kivshar, Phys. Rev. Lett. **111**, 240403 (2013).

[154] S. Flach, D. Leykam, J. D. Bodyfelt, P. Matthies, and A. S. Desyatnikov, EPL **105**, 30001 (2014), 1311.5689 .

[155] A. González-Tudela and J. I. Cirac, Phys. Rev. Lett. **119**, 143602 (2017).

[156] L. Leonforte, A. Carollo, and F. Ciccarello, Phys. Rev. Lett. **126**, 063601 (2021).

[157] A. González-Tudela, New Journal of Physics **24**, 043001 (2022).

[158] B. Bahari, A. Ndao, F. Vallini, A. E. Amili, Y. Fainman, and B. Kanté, Science **358**, 636 (2017).

[159] B. Bahari, L. Hsu, S. H. Pan, D. Preece, A. Ndao, A. El Amili, Y. Fainman, and B. Kanté, Nat. Phys. **17**, 700 (2021).

[160] A. V. Larionov, V. D. Kulakovskii, S. Höfling, C. Schneider, L. Worschech, and A. Forchel, Phys. Rev. Lett. **105**, 256401 (2010).

[161] B. Piętka, D. Zygmunt, M. Król, M. R. Molas, A. A. L. Nicolet, F. Morier-Genoud, J. Szczytko, J. Łusakowski, P. Zięba, I. Tralle, P. Stępnicki, M. Matuszewski, M. Potemski, and B. Deveaud, Phys. Rev. B **91**, 075309 (2015).

[162] C. Sturm, D. Solnyshkov, O. Krebs, A. Lemaître, I. Sagnes, E. Galopin, A. Amo, G. Malpuech, and J. Bloch, Phys. Rev. B **91**, 155130 (2015).

[163] H.-T. Lim, E. Togan, M. Kroner, J. Miguel-Sanchez, and A. Imamoğlu, Nat. Commun. **8**, 14540 (2017).

[164] T. Chervy, P. Knüppel, H. Abbaspour, M. Lupatini, S. Fält, W. Wegscheider, M. Kroner, and A. Imamoğlu, Phys. Rev. X **10**, 011040 (2020).

[165] I. Shelykh, G. Malpuech, K. V. Kavokin, A. V. Kavokin, and P. Bigenwald, Phys. Rev. B **70**, 115301 (2004).

[166] D. Sarkar, S. S. Gavrilov, M. Sich, J. H. Quilter, R. A. Bradley, N. A. Gippius, K. Guda, V. D. Kulakovskii, M. S. Skolnick, and D. N. Krizhanovskii, Phys. Rev. Lett. **105**, 216402 (2010).

[167] C. Adrados, A. Amo, T. C. Liew, R. Hivet, R. Houdré, E. Giacobino, A. V. Kavokin, and A. Bramati, Phys. Rev. Lett. **105**, 216403 (2010).

[168] M. Sich, F. Fras, J. K. Chana, M. S. Skolnick, D. N. Krizhanovskii, A. V. Gorbach, R. Hartley, D. V. Skryabin, S. S. Gavrilov, E. A. Cerda-Méndez, K. Biermann, R. Hey, and P. V. Santos, Phys. Rev. Lett. **112**, 046403 (2014).

[169] P. Cilibrizzi, H. Sigurdsson, T. C. H. Liew, H. Ohadi, S. Wilkinson, A. Askitopoulos, I. A. Shelykh, and P. G. Lagoudakis, Phys. Rev. B **92**, 155308 (2015).

[170] L. Pickup, K. Kalinin, A. Askitopoulos, Z. Hatzopoulos, P. G. Savvidis, N. G. Berloff, and P. G. Lagoudakis, Phys. Rev. Lett. **120**, 225301 (2018).

[171] I. Gnusov, H. Sigurdsson, S. Baryshev, T. Ermatov, A. Askitopoulos, and P. G. Lagoudakis, Phys. Rev. B **102**, 125419 (2020).

[172] W. Li, X. Lu, J. Wu, and A. Srivastava, Nat. Nanotechnol **16**, 148 (2021).

[173] L. Ferrier, E. Wertz, R. Johne, D. D. Solnyshkov, P. Senellart, I. Sagnes, A. Lemaître, G. Malpuech, and J. Bloch, Phys. Rev. Lett. **106**, 126401 (2011).

[174] K. V. Kavokin, I. A. Shelykh, A. V. Kavokin, G. Malpuech, and P. Bigenwald, Phys. Rev. Lett. **92**, 4 (2004).

[175] V. G. Sala, D. D. Solnyshkov, I. Carusotto, T. Jacqmin, A. Lemaître, H. Terças, A. Nalitov, M. Abbarchi, E. Galopin, I. Sagnes, J. Bloch, G. Malpuech, and A. Amo, Phys. Rev. X **5**, 011034 (2015).

[176] S. Dufferwiel, F. Li, E. Cancellieri, L. Giriunas, A. A. Trichet, D. M. Whittaker, P. M. Walker, F. Fras, E. Clarke, J. M. Smith, M. S. Skolnick, and D. N. Krizhanovskii, Phys. Rev. Lett. **115**, 246401 (2015).

[177] J. P. Reithmaier, M. Röhner, H. Zull, F. Schäfer, A. Forchel, P. A. Knipp, and T. L. Reinecke, Phys. Rev. Lett. **78**, 378 (1997).

[178] P. G. Lagoudakis, P. G. Savvidis, J. J. Baumberg, D. M. Whittaker, P. R. Eastham, M. S. Skolnick, and J. S. Roberts, Phys. Rev. B **65**, 161310 (2002).

[179] D. N. Krizhanovskii, D. Sanvitto, I. A. Shelykh, M. M. Glazov, G. Malpuech, D. D. Solnyshkov, A. Kavokin, S. Ceccarelli, M. S. Skolnick, and J. S. Roberts, Phys. Rev. B **73**, 073303 (2006).

[180] N. Takemura, S. Trebaol, M. Wouters, M. T. Portella-Oberli, and B. Deveaud, Nat. Phys. **10**, 500 (2014).

[181] R. I. Dzhioev, K. V. Kavokin, V. L. Korenev, M. V. Lazarev, B. Y. Meltser, M. N. Stepanova, B. P. Zakharchenya, D. Gammon, and D. S. Katzer, Phys. Rev. B **66**, 245204 (2002).

[182] A. Kavokin, G. Malpuech, and M. Glazov, Phys. Rev. Lett. **95**, 136601 (2005).

[183] C. Leyder, M. Romanelli, J. P. Karr, E. Giacobino, T. C. H. Liew, M. M. Glazov, A. V. Kavokin, G. Malpuech, and A. Bramati, Nat. Phys. **3**, 628 (2007).

[184] N. Carlon Zambon, P. St-Jean, M. Milićević, A. Lemaître, A. Harouri, L. Le Gratiet, O. Bleu, D. D. Solnyshkov, G. Malpuech, I. Sagnes, S. Ravets, A. Amo, and J. Bloch, Nat. Photonics **13**, 283 (2019).

[185] O. Bleu, D. D. Solnyshkov, and G. Malpuech, Phys. Rev. B **95**, 115415 (2017).

[186] O. Bleu, D. D. Solnyshkov, and G. Malpuech, Phys. Rev. B **93**, 085438 (2016).

[187] Z. Chen and B. Wu, Phys. Rev. Lett. **107**, 065301 (2011).

[188] O. Jamadi, B. Real, K. Sawicki, C. Hainaut, A. Gonzalez-Tudela, N. Pernet, I. Sagnes, M. Morassi, A. Lemaitre, L. L. Gratiet, A. Harouri, S. Ravets, J. Bloch, and A. Amo, Optically defined cavities in driven-dissipative photonic lattices (2021).

[189] B. Real, N. Carlon Zambon, P. St-Jean, I. Sagnes, A. Lemaître, L. Le Gratiet, A. Harouri, S. Ravets, J. Bloch, and A. Amo, Phys. Rev. Res. **3**, 043161 (2021).

[190] C. E. Whittaker, D. R. Gulevich, D. Biegańska, B. Royall, E. Clarke, M. S. Skolnick, I. A. Shelykh, and D. N. Krizhanovskii, Phys. Rev. A **104**, 063505 (2021).

[191] M. Di Liberto, A. Hemmerich, and C. Morais Smith, Phys. Rev. Lett. **117**, 163001 (2016).

[192] C.-E. Bardyn, T. Karzig, G. Refael, and T. C. H. Liew, Phys. Rev. B **93**, 020502 (2016).

[193] O. Mendoza-Yero, G. Mínguez-Vega, L. Martínez-León, M. Carbonell-Leal, M. Fernández-Alonso, C. Doñate-Buendía, J. Pérez-Vizcaíno, and J. Lancis, Journal of Display Technology **12**, 1027 (2016).

[194] I. C. Lenton, A. B. Stilgoe, T. A. Nieminen, and H. Rubinsztein-Dunlop, Computer Physics Communications **253**, 107199 (2020).

# List of Publications

1. O. Jamadi*, B. Real*, K. Sawicki, C. Hainaut, A. González-Tudela, N. Pernet, I. Sagnes, M. Morassi, A. Lemaître, L. Le Gratiet, A. Harouri, S. Ravets, J. Bloch, and A. Amo, *Optically defined cavities in driven-dissipative photonic lattices*, submitted. *Equal contribtution.

2. B. Real, N. Carlon-Zambon, P. St-Jean, I. Sagnes , A. Lemaître, L. Le Gratiet, A. Harouri, S. Ravets , J. Bloch, and A. Amo, *Chiral emission induced by optical Zeeman effect in polariton micropillars*, Phys. Rev. Research **3**, 043161 (2021)

3. P. St-Jean, A. Dauphin , P. Massignan , B. Real, O. Jamadi, M. Milicevic, A. Lemaître, A. Harouri, L. Le Gratiet, I. Sagnes, S. Ravets, J. Bloch, and A. Amo, *Measuring Topological Invariants in a Polaritonic Analog of Graphene*, Phys. Rev. Lett. **126**, 127403 (2021)

4. B. Real, O. Jamadi , M. Milićević, N. Pernet, P. St-Jean, T. Ozawa , G. Montambaux, I. Sagnes , A. Lemaître, L. Le Gratiet, A. Harouri, S. Ravets , J. Bloch, and A. Amo, *Semi-Dirac Transport and Anisotropic Localization in Polariton Honeycomb Lattices*, Phys. Rev. Lett. **125**, 186601 (2020)

5. M. Milićević, G. Montambaux, T. Ozawa, O. Jamadi, B. Real, I. Sagnes, A. Lemaître, L. Le Gratiet, A. Harouri, J. Bloch, and A. Amo, *Type-III and Tilted Dirac Cones Emerging from Flat Bands in Photonic Orbital Graphene*, Phys. Rev. X **9**, 031010 (2019)